

Kernel-Based PET Image Reconstruction using Dynamic
PET and MR Anatomical Information

by

Zahra Ashouri Talouki

A thesis submitted to the Faculty of Graduate and Postdoctoral
Affairs in partial fulfillment of the requirements for the degree of

Doctor of Philosophy

in

Systems and Computer Engineering

Carleton University

Ottawa, Ontario

© 2021

Abstract

Positron emission tomography (PET) imaging is used to track biochemical processes in the human body. PET image quality is limited by noise and several methods have been implemented to improve the quality. Kernel-based image reconstruction is among the methods implemented to increase PET image quality and commonly uses a Gaussian kernel. Unfortunately, the Gaussian kernel tends to smooth details in the reconstructed image. To reduce noise without losing contrast details, a different kernel is needed. This work gives an overview of Gaussian kernel PET image reconstruction and focuses on finding substitutes for the Gaussian kernel that tackles its shortcomings. A wavelet kernel can be more efficient than the Gaussian kernel in reducing noise while keeping contrast details by better separating signal from noise and thus it does not over smooth peak values in the final reconstructed images. In this thesis, a wavelet kernel was first applied on prior information derived from dynamic PET series, and its usefulness has been evaluated using simulated brain data, physical phantom data and patient data. Reconstruction results are presented and discussed in detail comparing the wavelet kernel method with the Gaussian kernel method. In the next step, using magnetic resonance (MR) information as prior information for kernel-based PET image reconstruction, the wavelet method is improved and extended by proposing a multi-scale wavelet kernel. This method identifies the directionality in the MR image and includes that information for kernel construction as well. Methods developed in this thesis allow for higher SNR in the reconstructed PET image while preserving contrast. They also produce reconstructed PET images with higher visual quality compared to Gaussian kernel methods.

Preface: Statement of Originality

This dissertation is a review of the author's core research during her Ph.D. studies at Carleton University. Portions of this work have been previously published in journal or as presented conference proceedings listed below in reverse chronological order.

All work was supervised by Dr. Richard Dansereau at Carleton University and Dr. Robert deKemp at the University of Ottawa Heart Institute. The author used available MATLAB code provided by Dr. Guobao Wang and Benjamin A. Spencer at the University of California, Davis to run the kernel-based image reconstruction in Chapter 3 and have adapted the code to new methods provided in the rest of the chapters. The author has used simulated data given in their package as part of the evaluation for Chapters 3, 4 and 6.

Also, the author received some help from Chad R. Hunter, a post-doctoral fellow at the Ottawa Heart Institute who provided an introduction on how to retrieve data from the PET/CT scanner at the Ottawa Heart Institute. He helped in some parts of the General Electric (GE) MATLAB toolbox and to convert the images outputted from the MATLAB GE toolbox to Digital Imaging and Communications in Medicine (DICOM) format which can be used in other medical image viewers such as AMIDE. He also helped the author to work with the AMIDE DICOM viewer to use this viewer for visualizations of results.

To reorient cardiac images and convert to polar map representation, the author used FlowQuant [1] software developed and maintained by Dr. Ran Klein, Dr. Robert deKemp, and Jennifer Renaud.

To register PET data to MR images, the author has used Elastix software [2]. All patient images were obtained from research subjects who provided written informed consent to participate in clinical research studies at the University of Ottawa Heart Institute.

All other work was performed by Zahra Ashouri under the supervision of Dr. Richard Dansereau and Dr. Robert deKemp. Specifically, my contributions to the research presented in this thesis are:

- Dr. deKemp helped me to carry out the NEMA phantom study when, due to covid, I could not do in person testing. He sent over the study, and I prepared them for reconstruction with MATLAB.
- I invented and developed the wavelet-based dynamic PET kernel method and implemented the method by writing MATLAB code, and designed experiments to validate the output.
- For the dynamic PET, I extensively evaluated the wavelet kernel method using simulated data, phantom study and also real patient data.
- I applied wavelet-based MR kernel with MR images as prior information. For this case, a physical phantom study was not feasible, therefore the results are evaluated based on simulated data and real patient data.
- I conceived the idea to use multi-scale wavelet and experiment with it for the MR prior information.
- Dr. Dansereau and I proposed including multi-directionality property of the wavelets for MR-based kernel reconstruction as well.
- I anonymized and exported clinical image datasets from the hospital servers
- I reconstructed all given images.
- I performed all calculations, evaluation, and statistical analysis using MATLAB.

- I wrote articles and abstracts and after receiving editing and comments from Dr. deKemp and Dr. Dansereau and Dr. Wang I submitted them, and I presented oral and poster presentations at meetings or conferences (oral or poster).

Peer-reviewed papers

- Z. Ashouri, R. M. Dansereau, G. Wang, and R. A. DeKemp, “Multi-scale Wavelet Kernel-based PET Reconstruction Using MR Prior Information and Feature-Driven Spatial Weighting,” submitted to *IEEE Trans. Radiat. Plasma Med. Sci.*
- Z. Ashouri, G. Wang, R. M. Dansereau, and R. A. DeKemp, “Evaluation of Wavelet Kernel-based PET Image Reconstruction,” *IEEE Trans. Radiat. Plasma Med. Sci.*, Aug 2021, doi: 10.1109/TRPMS.2021.3103104.

Conference Proceedings

- Z. Ashouri, G. Wang, R. M. Dansereau and R. A. deKemp, “Multi-scale Wavelet Kernel-based PET Reconstruction Using MR Side Information”, MIC-NSS 2021, Japan.
- Z. Ashouri, C. R. Hunter, B. A. Spencer, G. Wang, R. M. Dansereau and R. A. deKemp, “Kernel-based Reconstruction of Cardiac PET Images Using MR Information”, University of Ottawa Heart Institute’s Annual Research Day, Ottawa, ON, May 2021.
- Z. Ashouri, C. R. Hunter, B. A. Spencer, G. Wang, R. M. Dansereau and R. A. deKemp, “Kernel-based Reconstruction of Cardiac PET Images Using MR Information”, in *2020 IEEE Nuclear Science Symposium and Medical Imaging Conference (NSS/MIC)*, 2020, pp. 1-2, doi: 10.1109/NSS/MIC42677.2020.9507993.
- Z. Ashouri, A. Groll and C. S. Levin, "PET Reconstruction with a Spatially Varying Point Spread Function for a Brain Dedicated PET Insert for PET/MR," *2020 IEEE Nuclear Science Symposium and Medical Imaging Conference (NSS/MIC)*, 2020, pp. 1-3.

- Z. Ashouri, C. R. Hunter, B. A. Spencer, G. Wang, R. M. Dansereau, and R. A. deKemp, “Dynamic PET Image Reconstruction Using the Wavelet Kernel Method,” in *2019 IEEE Nuclear Science Symposium and Medical Imaging Conference (NSS/MIC)*, Oct. 2019, pp. 1–3. doi: 10.1109/NSS/MIC42101.2019.9059890.
- Z. Ashouri, C. R. Hunter, B. A. Spencer, G. Wang, R. M. Dansereau, and R. A. deKemp, “Kernel-Based Reconstruction of C-11-Hydroxyephedrine Cardiac PET Images of the Sympathetic Nervous System,” in *2019 41st Annual International Conference of the IEEE Engineering in Medicine and Biology Society (EMBC)*, Jul. 2019, pp. 832–835. doi: 10.1109/EMBC.2019.8856752.
- Z. Ashouri, C. R. Hunter, B. A. Spencer, G. Wang, R. M. Dansereau, and R. A. deKemp “Kernel-Based Dynamic Cardiac PET Image Reconstruction of C-11-Hydroxyephedrine,” University of Ottawa Heart Institute’s Annual Research Day, Ottawa, ON, April 2019.

Acknowledgements

I would like to acknowledge the following sources of funding, without which this work might not have been possible: Natural Sciences and Engineering Research Council of Canada (NSERC), Alexander Graham Bell Canada Graduate Scholarships, NSERC Discovery Grant and Ontario Graduate Scholarship (OGS). Along with several donor funded awards such as: Dr. Roger Kay Memorial Scholarship awarded three times, Bader Student Travel Award and NSERC funding for Canada Graduate Scholarships – Michael Smith Foreign Study Supplements to aid in conducting research outside country.

Additionally, I would like to thank the IEEE, the Society of Nuclear Medicine and Molecular Imaging, the Canadian Institutes for Health Research, and the OHIRC for providing travel support to the numerous conferences that I was privileged to be a part of.

I am grateful to the Carleton University Systems and Computer Engineering department. I appreciate the support that I have received in the form of funding application review, nominations for internal funding, and accommodating my TA leaves due to child-care responsibilities. I would like to thank the University of Ottawa Heart Institute for their amazing and friendly environment in which I've learnt a lot. It also gives me the opportunity to present my work to people of different backgrounds.

I am grateful to my supervisors Dr. Richard Dansereau and Dr. Robert deKemp for their continued support throughout this journey. Our discussions with Dr. Dansereau kept me in the right track for my goal and Dr. deKemp provided insights on the clinical side as well as connecting me to amazing physicists working in the field. I am greatly thankful to Dr. Guobao Wang, our collaborator from University of California, Davis. I would like to thank him for very useful discussions and all his valuable comments on the publications.

I would also like to thank my supervisors for being supportive of my decision to spend a few months at Stanford University as a visitor researcher which was a great opportunity for me. I would also like to extend mt thanks to Dr. Craig Levin at Stanford University whom I had the pleasure of working with during my research experience abroad. I would like to thank him for giving me the incredible opportunity of working in development of a PET scanner. It has been an amazing experience working with him and his talented team.

Finally, I thank my friends and family. To my parents, thank you for your support and help in any way you could from far away. I love you as much. To my husband, Mohsen, thank you for encouraging me whenever I needed and thanks for accommodating me following my dreams in any way you could. To my daughter, Sara, thank you for your understanding and patience, especially during covid and work from home and school closures. I cannot believe we passed through that stage together. I am proud of you.

Table of Contents

Abstract	ii
Preface: Statement of Originality.....	iii
Acknowledgements	vii
List of Illustrations.....	xii
List of Tables	xvi
List of Abbreviations.....	xvii
Chapter 1 : Introduction	1
1.1 Introduction and Motivation	1
1.2 Aims and Objectives	2
1.3 Organization of Chapters.....	4
1.4 List of Contributions	4
Chapter 2 : Overview of PET Imaging	8
2.1 Positron Annihilation	8
2.2 PET Scanner	10
2.3 Data Acquisition, Projections and Sinograms.....	11
2.4 Scatter, Randoms and Attenuation	13
2.5 Image Reconstruction.....	16
2.6 Dynamic PET Imaging	22
2.7 Time Activity Curve.....	23
2.8 The Compartment Model	23
2.9 Previous Work	26
2.10 Summary.....	28

Chapter 3 : Kernel Based Image Reconstruction using Gaussian Kernel	30
3.1 PET Image Reconstruction using Kernel in EM.	30
3.2 Feature vectors.....	31
3.3 Parameter Selection for Gaussian Kernel	34
3.4 Evaluation Method for Patient Data.....	36
3.5 Experimental Setup	38
3.6 Result of the Gaussian Kernel.....	39
3.7 Summary.....	46
Chapter 4 : Substitutes for Gaussian Kernel	48
4.1 Admissible Kernels.....	48
4.2 Kernels	49
4.3 Reconstruction Results of Given Wavelet Kernels	54
4.4 Summary.....	60
Chapter 5 : Kernel Based Image Reconstruction using Morlet Wavelet Filter	61
5.1 Details of the Proposed Morlet Wavelet Kernel.....	61
5.2 Simulation Study.....	63
5.3 Real Data	68
5.4 Summary.....	75
Chapter 6 : Gaussian Kernel Based Image Reconstruction using MR Information.....	76
6.1 Method	77
6.2 Patient Study	78
6.3 Summary.....	81
Chapter 7 : Multi-scale Morlet Wavelet Kernel-based PET Reconstruction Using MR Prior Information	82
7.1 Anatomical Prior Kernel Extraction	82

7.2	Single-scale and Multi-scale Wavelet Kernels	83
7.3	Gabor Spatial Weighting.....	84
7.4	Simulation Study.....	89
7.5	Patient Data	97
7.6	Summary.....	100
Chapter 8 : Conclusions and Future Work		101
8.1	Conclusions.....	101
8.2	Future work	103
<i>Appendix.....</i>		<i>106</i>
<i>References</i>		<i>122</i>

List of Illustrations

<i>Figure 1. Positron decay leading to an annihilation event results in the production of two gamma rays with equal energy and opposite momentum.</i>	<i>10</i>
<i>Figure 2. Sinogram of a point source (after [15]).</i>	<i>11</i>
<i>Figure 3. (a) Stacking of all grouped sinograms by angle which forms a single sinogram, (b) stacked projection view for all slices, and (c) reconstructed frame.</i>	<i>12</i>
<i>Figure 4. Representation of a scatter coincidence. Red line shows the path of the photon, and the blue line is the recorded LOR.....</i>	<i>13</i>
<i>Figure 5. Representation of a random coincidence. Red lines show the path of the incident photons, and the blue line is the recorded LOR.</i>	<i>14</i>
<i>Figure 6. An example of object forward projection and back projection for image reconstruction.</i>	<i>18</i>
<i>Figure 7. Four different time frames (30 s, 50 s, 2 minutes, 40 minutes) in a dynamic PET series of heart images using C-11-HED tracer. The sequence of frames starts from the left towards the right.</i>	<i>22</i>
<i>Figure 8. Time Activity Curve for blood cavity and left ventricle wall. The mid-frame sampling time-points are shown on the blood curve</i>	<i>23</i>
<i>Figure 9. This one-tissue compartment model describes the bidirectional flux of tracer between blood C_b and tissue C_t.</i>	<i>25</i>
<i>Figure 10. Composite frames made by summing dynamic frames.....</i>	<i>31</i>
<i>Figure 11. An example showing the left ventricle (LV) wall segment (the area inside the two orange lines) and blood cavity (Blc) ellipsoid area (shown in green) inside the left ventricle and an ellipsoid area inside liver (shown with blue). This image is from KEM reconstruction.....</i>	<i>38</i>
<i>Figure 12. Standard deviation in blood cavity in a few frames and for different k values.</i>	<i>39</i>
<i>Figure 13. Standard deviation in blood cavity in a few frames and for different σ values.....</i>	<i>40</i>
<i>Figure 14. SNR versus contrast for OSEM without and with different smoothing filters (from FWHM2 corresponding to FWHM of the filter equal to 2 mm to FWHM16 referring to FWHM of the filter equal to 16 mm) and KEM for average of last four frames (uptake frames).</i>	<i>41</i>

Figure 15. Transaxial slice of the last frame from a normal patient comparing KEM reconstruction with OSEM reconstruction using different levels of post filtering (from FWHM2 corresponding to FWHM of the filter equal to 2 mm to FWHM16 referring to FWHM of the filter equal to 16 mm).	42
Figure 16. Average SNR and contrast for all the patients for KEM and OSEM with different post filtering. .	43
Figure 17. Mean and standard deviation (Std) of late uptake values in different tissue regions for the ischemic patients (top) and normal subjects (down). Liver and blood Std was significantly reduced using KEM compared to OSEM.....	44
Figure 18. 3D Contour map of the left ventricle wall for an ischemic and a normal case using KEM reconstruction.	45
Figure 19. Polar map of the left ventricle distribution in the uptake frames. KEM is quantitatively accurate.	46
Figure 20. Ricker wavelet function.	50
Figure 21. An even version of Meyer wavelet function (shifted in time).	51
Figure 22. Even versions of biorthogonal 2.4 and 2.6 wavelet functions (decomposition functions).	52
Figure 23. Morlet wavelet function for different ω values.	53
Figure 24. a) Digital phantom with A, B, C, and D being regions in the blood pool, gray matter, white matter and tumor region, respectively. b) Time activity curve for different regions.....	54
Figure 25. Reconstructed images of frame 2 from different reconstruction methods along with the original phantom.....	57
Figure 26. Reconstructed images of frame 24 from different reconstruction methods along with the original phantom.....	59
Figure 27. 1-D Gaussian function vs proposed Morlet wavelet.	63
Figure 28. Basis image of the two kernel matrices that corresponds to a pixel in the tumor region of the simulated brain.....	64
Figure 29. MSE for different " σ " (" a " for wavelet) value shown for frame 2 and frame 24.	65
Figure 30. Ground truth and reconstructed images of three different reconstruction methods for two different time frames of the brain phantom.	67

Figure 31. Contrast recovery versus background standard deviation for Zubal head phantom. Blood pool is calculated in frame 2 and the tumor is calculated in frame 24.....	67
Figure 32. Mean square error (MSE) for different reconstruction methods shown for each frame with the standard deviation error bars for ten realizations.	68
Figure 33. Contrast recovery versus background variability for all sphere sizes, with sphere 1 being the smallest sphere and sphere 6 being the largest sphere.	70
Figure 34. Reconstructed image of a frame from NEMA phantom.	72
Figure 35. Average SNR and contrast over all frames for OSEM (with 4 mm post filtering), KEM, and WKEM.	72
Figure 36. A transaxial slice of the heart for OSEM, KEM, and WKEM. Each row corresponds to one of the patients and shows the last frame	73
Figure 37. SNR vs contrast of uptake frames (last four frames) averaged over all patients for OSEM (with 4 mm post filtering), KEM, and WKEM.....	74
Figure 38. A transaxial slice of the heart from patient #1 for a late frame showing reconstructed image for MKEM and KEM and the corresponding SSFP MR image.....	79
Figure 39. K_1 values for three reconstruction methods and all three patients. Each patient is shown in one row. The mean and standard deviation of K_1 is shown.....	81
Figure 40. MR image showing feature extraction with patch-wise similarity between voxels. f_j is the feature vector for pixel j and it contains all the pixels in the blue window and f_l is the feature vector for pixel l and consists of all the pixels in the green window.	83
Figure 41. Real and imaginary part of the Gabor filter for given parameters.....	86
Figure 42. Gabor filters of three wavelengths and six directions.	88
Figure 43. Simulated brain image with different PET reconstruction methods. (a) Middle row is from MRI without tumor and (b) the bottom row is with tumor present in MR image.....	91
Figure 44. Contrast recovery versus background standard deviation for simulated brain phantom calculated for tumor region.	92
Figure 45. SNR value for different number of coincidence events with 40 iterations and 10 realizations	93

Figure 46. SNR for different "a" values with 40 iterations and 200K coincidence events.94

Figure 47. SNR for different neighbourhood sizes with 40 iterations and 200K coincidence events. For a 3 ×3 neighbourhood, 5 pixels are chosen in kNN, for 5×5 neighbourhood 10 pixels are chosen, and for 7 ×7 and 9×9 neighbourhoods 16 and 20 pixels are chosen respectively.....94

Figure 48. SSIM map for reconstructed images of different methods. The high value of SSIM map shows higher structural similarity between the reconstructed image and the reference image. The second column is the part shown in rectangular of the first column.96

Figure 49. Reconstructed images of the simulated brain comparing multi-scale wavelet with Gaussian weighting and multi-scale wavelet with Gabor weighting.....97

Figure 50. SNR versus contrast averaged over three patients showing OSEM, KEM, WKEM-SS and WKEM-MS98

Figure 51. Patient data showing reconstruction result of left and right ventricle.....99

List of Tables

<i>Table 1. Common isotopes used in PET imaging and their properties.</i>	<i>9</i>
<i>Table 2. SNR values for frame 2 and frame 24 comparing different kernels for kernel reconstruction.</i>	<i>59</i>
<i>Table 3. SNR and contrast values for the late uptake frames for all three patients.</i>	<i>79</i>
<i>Table 4. SSIM values for different reconstruction methods. The values are averaged over 10 realizations.</i>	<i>95</i>
<i>Table 5. Average SNR and contrast values for three patients</i>	<i>99</i>

List of Abbreviations

1D, 2D, 3D	1, 2 or 3-Dimensional
ACF	attenuation correction factor
BGO	bismuth germanium oxide
CPU	central processing unit
CRC	contrast recovery coefficient
CT	computed tomography
D600	GE Discovery-600
DICOM	Digital Imaging and Communications in Medicine
ECG	electrocardiogram
EM	Expectation maximization
FBP	filtered back projection
FDG	Fludeoxyglucose
FOV	field of view
FWHM	full width half maximum
GE	General Electric
HED	C-11-hydroxyephedrine
HU	Hounsfield unit
HYPR	highly constrained back-projection
KEM	kernel-based expectation maximization
k NN	k -nearest neighbour
KPCA	kernel principal component analysis
LOR	Line of response
LV	Left Ventricle
MAP	maximum a posteriori
MKEM	MR kernel-based expectation maximization
ML	maximum likelihood
MLEM	maximum likelihood expectation maximization
MR	Magnetic resonance

MRI	Magnetic resonance imaging
MS	multi-scale
MSE	mean square error
MTI	multi-scale translation invariant
NEMA	National Electrical Manufacturers Association
NLM	non-local means
OSEM	ordered subsets expectation maximization
PCA	Principal component analysis
PET	positron emission tomography
PICCS	Prior image constrained compressed sensing
PSF	point spread function
RMS	root mean square
ROI	region of interest
SD	standard deviation
SNR	signal to noise ratio
SS	single-scale
SSFP	steady-state free precession
SSIM	structural similarity index
STI	single-scale translation invariant
SVM	support vector machine
TAC	Time Activity Curve
WKEM	wavelet kernel-based expectation maximization

Chapter 1 : Introduction

1.1 Introduction and Motivation

Positron emission tomography (PET) is used in the detection and characterization of several diseases, such as cancer, neurological disorders, and cardiovascular disease. PET imaging is used to observe biochemical and physiological processes within the human body using radioactive tracers. However, PET spatial resolution is limited due to factors such as intrinsic detector resolution, annihilation photon collinearity, positron range, and statistical noise. Several methods have been proposed to increase image quality. One method to improve PET image quality is to incorporate prior information [3].

Prior information can be from dynamic PET series itself or from anatomical image modalities. In contrast to PET imaging, anatomic imaging modalities, such as computed tomography (CT) and magnetic resonance imaging (MRI), can offer higher spatial resolution and accurate tissue boundary information. Information in anatomical imaging modalities can be incorporated in PET image reconstruction to have a higher quality reconstructed image [4]–[7]. Most PET imaging machines are currently hybrid PET/CT scanners and more recently in fewer numbers PET/MR. The primary benefit of PET/CT systems is for fast and accurate attenuation correction for PET and image co-registration. But the benefit of anatomical imaging methods is not limited to attenuation correction, especially with the introduction of new PET/MR systems offering simultaneous data acquisition. These PET/MR systems offer new ways to further use anatomical information within PET reconstruction [8].

1.2 Aims and Objectives

In this work, the idea is to use prior information to reduce noise and increase resolution in reconstructed PET images. This prior information is derived from two different sources, first the dynamic PET series itself can provide prior information and second MR image for extracting anatomy information. Therefore, I have first tried using dynamic PET images to reduce noise similar to the kernel method introduced by Wang et al. [9]. But since the Gaussian kernel used in their kernel method had some drawbacks, other kernel functions were tested, and a wavelet-based kernel was selected which preserved edge information while reducing noise. This wavelet-based kernel was extensively tested using different datasets, simulated data, a physical phantom data and real patient data. Then the kernel method was applied with prior anatomical information from an MR imaging, this method can be applied both to static and dynamic PET image reconstruction. First the kernel method with Gaussian kernel was applied to prior information from MR image and it was compared to kernel reconstruction results with the dynamic PET series as prior information. The wavelet kernel is then used for kernel-based reconstruction with MR prior information. The wavelet kernel has been modified and enhanced by incorporating the multi-scale property and is then used to extract a kernel from MRI. Directionality information of the MR image are also included in the kernel construction.

My contributions in this work are investigating wavelet-based dynamic PET kernel method for different datasets and wavelet-based MR kernel method for PET image reconstruction. Exploring the multi-scale property of the wavelet for the MR prior information is also another contribution in this thesis. I have also proposed including the

directionality information in the MR image for the kernel construction. For the MR wavelet kernel method, the phantom study was not feasible as the phantom did not show any contrast in an MRI machine, therefore the results are evaluated based on simulated data and real patient data. The multi-scale wavelet eliminates the need to empirically set the parameter in single-scale wavelet and is expected to increase the quality of reconstructed image by including different scales in wavelet.

For prior information from dynamic PET series, in the case of simulated data, a simulated brain is used for which tumor detection and the overall visual quality of the reconstructed image using different methods is investigated. For the phantom study NEMA phantom is used, and the effect of wavelet-based kernel method in the quality of the reconstructed spheres is evaluated. For the patient data heart images are used. Most heart diseases start in the left ventricle, and this is the tissue which is more visible in PET imaging. Also, for blood flow imaging, tracer uptake in the myocardium (left ventricle wall) is the region of interest (ROI); therefore, for patient cases I am focusing on the quality of the left ventricle as my ROI.

As mentioned for MR-based kernel reconstruction, I included directionality information from MR images in the kernel as well. To do that, the spatial information in the chosen neighborhood for each pixel is used to find the direction of the edges in the neighborhood and that direction is also included in the weighting defined between pixels. The expectation is that this way higher quality would be achieved since MR shows much higher quality edges compared to PET. For real patient data, left ventricle walls have a clearer representation in anatomical images. Therefore, MR images which contain anatomical information are expected to increase the quality of reconstructed PET images,

both in terms of noise reduction and contrast enhancement. For the simulated data, similar results may be expected since the boundary details are not very precise in PET imaging and the expectation is to get a clearer image with the inclusion of anatomical information from MRI. In the following chapters, these hypotheses are elaborated.

1.3 Organization of Chapters

In Chapter 2, an overview on PET imaging is provided including its basic physics, acquisition method and some literature review. Chapter 3 explains the kernel method for dynamic PET and gives some experimental results for real data. Then the substitutes for Gaussian kernel are introduced and tested in Chapter 4. Chapter 5 corresponds to wavelet-based kernel reconstruction using dynamic PET with three different data sets. Chapter 6 focuses on kernel reconstruction using MR prior information and compares it to the dynamic prior information with radial Gaussian kernel. In Chapter 7 single-scale wavelet kernel and the multi-scale wavelet kernel with directionality information are used for reconstruction using MR information and the results are presented for simulated data and real patient data. Conclusion and future directions for this work are given in Chapter 8.

1.4 List of Contributions

Here is the list of contributions presented in this thesis.

- Kernel-based image reconstruction was applied to cardiac PET images with C-11-hydroxyephedrine (HED) tracer and compared with the current clinical reconstruction method. The goal was to establish the usefulness of the kernel method for cardiac images where patient motion and cardiac and respiratory motion are present to see if there is an improvement in the quality of reconstructed images. This contribution has been published in

IEEE EMBC 2019 proceedings as “Kernel-Based Reconstruction of C-11-Hydroxyephedrine Cardiac PET Images of the Sympathetic Nervous System”.

- A drawback of the Gaussian kernel in PET image reconstruction is the over-smoothing effect, therefore a different kernel is desirable to reduce noise while keeping the details in the reconstructed images. The hypothesis was to use wavelet kernel for the kernel reconstruction to overcome the shortcoming of Gaussian kernel. This contribution has been presented at the IEEE NSS-MIC 2019 conference as “Dynamic PET Image Reconstruction Using the Wavelet Kernel Method”.
- To further investigate the proposed wavelet kernel, I extended the study by including simulated brain data and NEMA phantom data. Using different data sets and a number of quality measurements enables me to have a more comprehensive comparison between Gaussian kernel and wavelet kernel and check the downsides of wavelet kernel and the results were published in the journal of IEEE Transactions on Radiation and Plasma Medical Sciences with the title “Evaluation of Wavelet Kernel-based PET Image Reconstruction”.
- Then to test the method using other prior information, MR images were used as a source of information in the kernel-based reconstruction of cardiac images. The kernel was defined based on anatomical MR images and used in PET image reconstruction. Then to see the effect of different prior information in the final reconstructed image, the results were compared to

the original kernel-based image reconstruction and has been presented at IEEE NSS-MIC 2020 conference as “Kernel-based Reconstruction of Cardiac PET Images Using MR Information”.

- With establishing the effectiveness of prior information from MR images, I applied wavelet kernel method with the information from MR images to a simulated brain data. The wavelet kernel was also extended to a multi-scale kernel wavelet and both the single-scale and multi-scale wavelet were compared with original Gaussian kernel. The results were presented at IEEE NSS-MIC 2021 conference as “Multi-scale Wavelet Kernel-based PET Reconstruction Using MR Side Information”.
- Then the multi-scale wavelet was combined with directionality information of the MR image using Gabor filter bank. This extended work was expected to produce better quality around the edges due to directionality information included in the kernel. The results were tested on simulated data and patient data and submitted to the journal of IEEE Transactions on Radiation and Plasma Medical Sciences as “Multi-scale Wavelet Kernel-based PET Reconstruction Using MR Prior Information and Feature-Driven Spatial Weighting”.

There were also a couple of internal research days at the Ottawa Heart Institute (2019 and 2021) at which I presented my work. Also, I submitted another contribution from my two months research experience abroad at Stanford University:

- I calculate PSF for their brain-dedicated MR compatible PET system by placing a point source inside it and measuring the response at different

locations. Then the measured PSF is used in the system model of MR compatible PET insert for image reconstruction. The result of this work was presented at IEEE NSS-MIC 2020 conference as “PET Reconstruction with a Spatially Varying Point Spread Function for a Brain Dedicated PET Insert for PET/MR”. This work is currently under extensive phantom evaluation for a journal submission.

Chapter 2 : Overview of PET Imaging

Positron emission tomography (PET) is used in the detection and characterization of several diseases, such as cancer, neurological disorders, and cardiovascular disease. PET imaging is used to observe biochemical and physiological processes, such as blood flow or neurotransmitters in the human body. For this purpose, a small amount of radioactive material (called a tracer) is injected into the body and a PET scanner images the tracer distribution over time in various tissues or in the organ of interest [10]. PET scanners acquire this information by measuring the coincident annihilation photons emitted from the radiotracer within the patient's body. These measurements are then reconstructed into cross-sectional images by iterative reconstruction methods. These steps are further explained in this chapter.

2.1 Positron Annihilation

In one method of producing isotopes that decay by positron emission, hydrogen ions are accelerated to high speeds using electromagnetic fields in a machine called a cyclotron. The accelerated hydrogen ions are then diverted away to interact with stable elements, such as carbon, nitrogen, oxygen or fluorine, which results in the elements being converted into radioactive isotopes. These radioactive isotopes are unstable because they possess too many protons and soon start to decay to reach a more stable configuration [11]. The isotopes decay at different rates depending on their nuclear arrangements and therefore have different half-lives. The half-life, isotope source and positron range for some known isotopes are given in Table 1. Most of the PET tracers, like the ones mentioned in this table, are cyclotron produced which means any clinic wanting to perform PET scans with these tracers must have access to a cyclotron nearby.

As the isotopes decay, they emit a positron from the nucleus turning one of the protons into a neutron for different isotopes. The newly ejected positron will then travel through the surrounding medium and lose energy, therefore even high energy positrons will eventually lose too much energy to resist the Coulomb force of attraction to an electron in the medium, and the two particles will combine and undergo annihilation. Positron annihilation is the term used to refer to the collision of an electron and a positron resulting in the creation of two gamma ray photons. The total energy and momentum of the initial pair are conserved in the annihilation process, causing the two photons to travel in the opposite direction at 180° to each other. It is these gamma rays that are detected during the PET scan. This process is shown Figure 1.

The distance that a positron travels from the source of emission to the point it undergoes annihilation, expressed in mm is positron range and is shown in Table 1 for each isotope.

Table 1. Common isotopes used in PET imaging and their properties.

Isotope	C-11	N-13	O-15	F-18
Isotope Production	Cyclotron	Cyclotron	Cyclotron	Cyclotron
Half-life (min)	20	10	2	110
Positron Range (mm) root mean square (RMS)	0.28	0.45	1.04	0.22

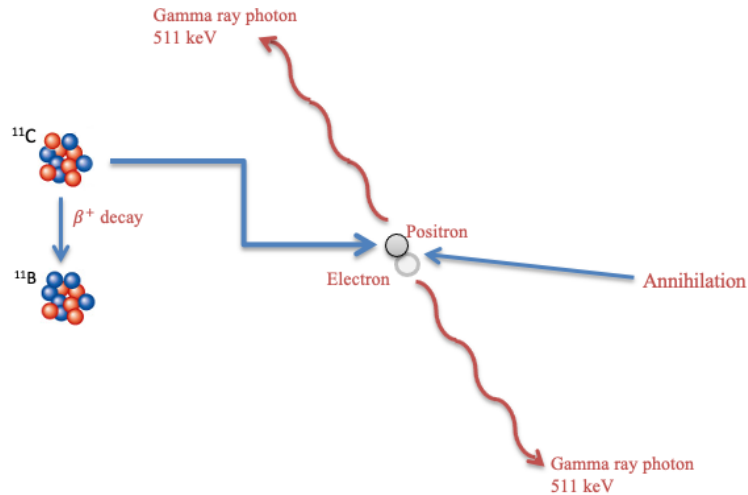


Figure 1. Positron decay leading to an annihilation event results in the production of two gamma rays with equal energy and opposite momentum.

2.2 PET Scanner

PET imaging systems benefit from the physics of positron annihilation. Detectors in a PET scanner, which are placed around the radiation source (patient), are designed to record coincident photons (events). These coincident events are recorded along the line of response (LOR) between the two detectors that have detected the coincident photons as shown in Figure 2.

Early PET scanners had a pair of detectors that rotated around the patient, but all modern PET systems use a ring (or cylinder) of detector crystals. Different scanners have different scintillation crystals to detect gamma photons. For example, the GE Discovery-600, which is the source of the patient data sets, uses bismuth germanate or bismuth germanium oxide (BGO) scintillation crystals. Scintillation is the process of emitting electromagnetic waves, especially in the visible spectrum, following the absorption of ionizing radiation.

The measured coincidence only gives information about the possible line of response between the two crystals where the annihilation event happened, but it cannot indicate where along that line this event took place. However currently, new scanners can use the time difference between coincident photon pairs to estimate the approximate location of the annihilation event along the line of response, which is known as time-of-flight imaging [12].

The GE Discovery-600 (D600), which is widely used clinically and is the source of the real data in this dissertation, combines a BGO block detector designed PET with a 16-slice CT scanner [13]. The system includes image reconstruction computers implementing fully 3D-PET iterative reconstruction algorithms. The D600 consists of 24 rings of detectors for an axial field of view (FOV) of 153 mm. The transaxial FOV diameter is 70 cm.

2.3 Data Acquisition, Projections and Sinograms

To have a photon pair recorded as an annihilation event, several conditions must be met. Photons must fall within the expected energy window (e.g. 425-650 keV for GE-D600), they must deposit their energy within the coincidence time window (e.g. 9.5 ns for GE-D600), and there should be a valid acceptance angle for the line of response between

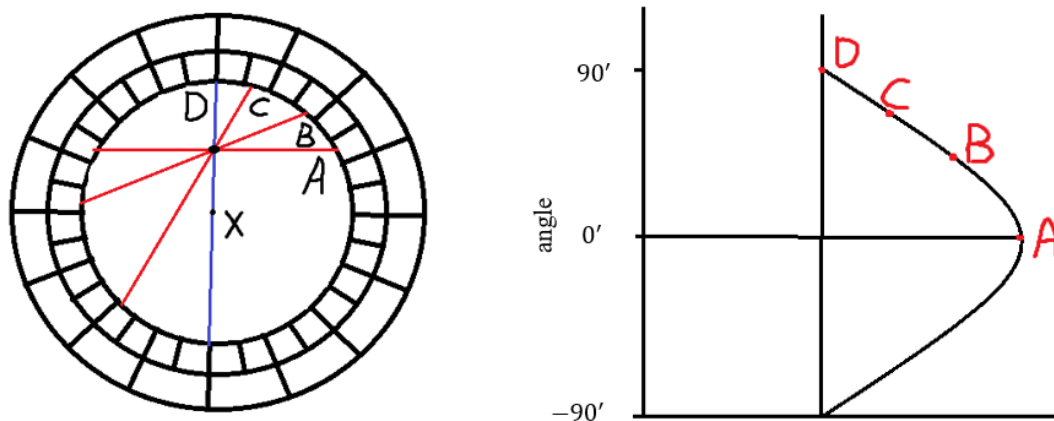


Figure 2. Sinogram of a point source (after [15]).

the two detector crystals in coincidence. The valid events, who meet the conditions, are collected and typically stored in a data structure called a sinogram (this is not the only format that PET scanners store data) as illustrated in Figure 2 [14].

In Figure 2, the center of the PET scanner is marked as “X”. Four different lines of response (LORs) passing through a certain point of coincident events are shown. LORs are connecting two different crystals on the PET scanner. They are characterized by their angle of orientation and the shortest distance of the LOR from the center of the scanner. Each LOR can be plotted for a given source point by putting the angle of LOR from the horizontal on the y-axis and the displacement on the x-axis. If large numbers of LORs are plotted on this diagram, it will trace out a sinusoidal function as shown in Figure 3. By doing so for several point sources, there will be large number of overlapping sinusoids in the sinogram. Sinogram dimensions for GE-D600 shown in Figure 3 is 339 by 256.

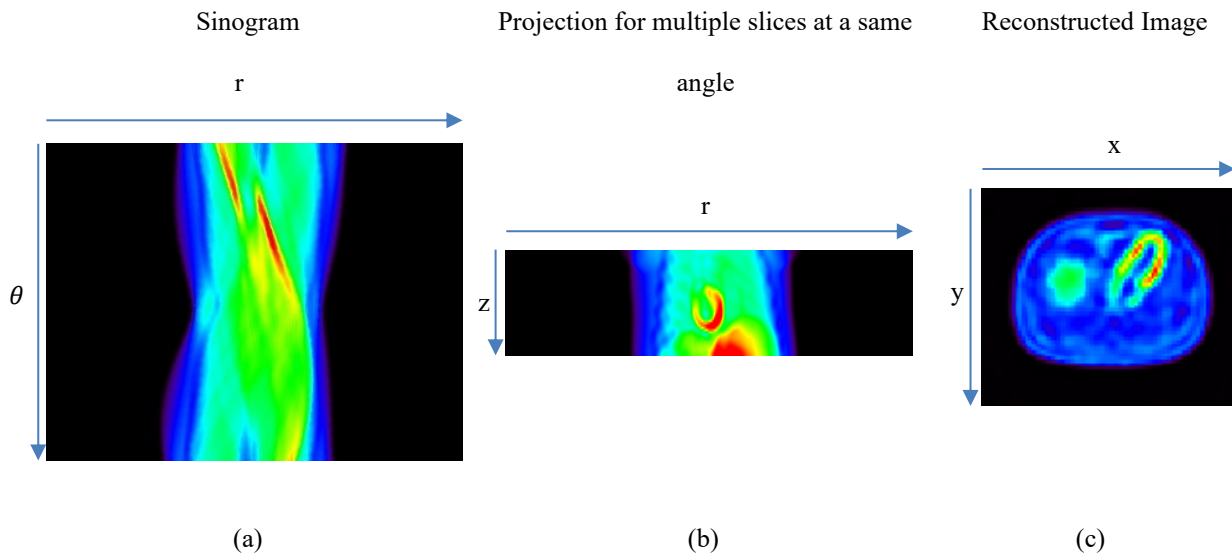


Figure 3. (a) Stacking of all grouped sinograms by angle which forms a single sinogram, (b) stacked projection view for all slices, and (c) reconstructed frame.

By grouping parallel LORs with different displacement values, a “projection” is formed [15]. Projections can be stacked in increasing angular displacement along the radial axis (r) to form a sinogram. Therefore, a sinogram contains all projection information for a single slice.

2.4 Scatter, Randoms and Attenuation

There are a number of factors affecting the quality and accuracy of PET images, which should be accounted for during image reconstruction. One of the major factors that limit the accuracy of PET images is Compton scattering [14]. Compton scattering refers to the situation where a photon scatters and changes direction (and loses energy) in human tissue but is still detected. As shown in Figure 4, this results in an LOR that does not cross the annihilation point where emission occurs at a point within the heart and one of the photons scatters off the bone of a rib.

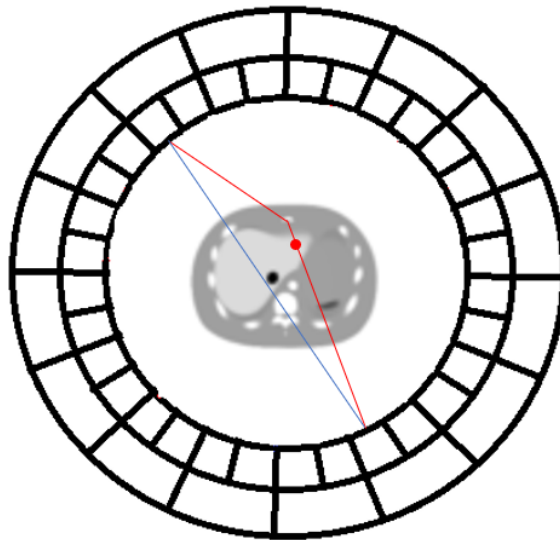


Figure 4. Representation of a scatter coincidence. Red line shows the path of the photon, and the blue line is the recorded LOR.

Compton scattering results in an image with significantly reduced image contrast and signal-to-noise ratio. For 2D PET, scatter is negligible and in many cases it was ignored, but in 3D imaging, 35–50% of detected events may be scattered and therefore accurate scatter correction is essential [14]. There are a number of methods for scatter correction, but the most common is the single scatter simulation model [16]–[20]. Scatter correction is included in the clinical PET/CT scanners such as GE Discovery-600, and is available in the research software toolbox provided by the manufacturer and is therefore included in the clinical image reconstructions.

In addition to scatter events, there are random events which degrade the quality of the final reconstructed PET images by adding a relatively uniform and noisy background to the measured data if not corrected. A random event refers to a situation where two different annihilation events are detected as one coincident event. An example of these events is shown in Figure 5.

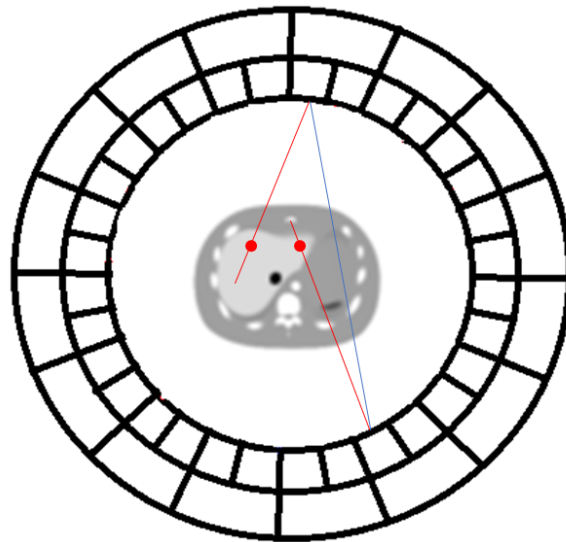


Figure 5. Representation of a random coincidence. Red lines show the path of the incident photons, and the blue line is the recorded LOR.

As mentioned before, PET imaging detects coincidence events based on a coincidence timing window. This finite timing window, however, is not capable of ignoring random events that occur when two unrelated photons, which do not originate from the same site of positron annihilation, are detected within the timing window. Random correction using a delayed coincidence window or calculation from the detector singles rates is also included in the standard software toolbox of the PET/CT scanners.

Another important factor affecting the quality of PET images is attenuation. Attenuation refers to the situation on which annihilation photons emitted from the tracer inside the patient are scattered or absorbed in the tissue and are unable to reach the detector. This loss results in underestimation of true activity inside the body and therefore should be corrected. The attenuation factor is typically known for different tissues, like bone, soft tissue, and lungs. Knowing the attenuation coefficient, the fraction of photons that will pass the medium can be calculated using [14]

$$\Psi = \exp\left(-\int_0^d \mu(r)dr\right). \quad (1)$$

This fraction of photons leaving the attenuating medium (Ψ), is a function of the integral of attenuation coefficient ($\mu(r)$ cm^{-1}) and along the LOR (line of response) from the point of annihilation ($r = 0$) to the location where the first photon exit the patient body ($r = d$). Attenuation coefficient ($\mu(r)$) itself is also a function of location r along the LOR in general. If the patient is considered to have total thickness of D , for a photon traveling in the opposite direction the above formula would change to

$$\Psi = \exp\left(-\int_{-(D-d)}^0 \mu(r)dr\right). \quad (2)$$

If the attenuation coefficient is constant along the line of response, the above equations will be simplified to $e^{-\mu d}$ and $e^{-\mu(D-d)}$. Therefore, the probability of having a coincidence event detected in a line of response is the product of the above probabilities and is given by

$$\Psi = \exp(-\mu D). \quad (3)$$

This equation indicates that the probability of detection is independent of the source position. If the tissue and therefore the attenuation coefficients are not uniform, the probability of detection is given by

$$\Psi = \exp\left(-\int_{-(D-d)}^d \mu(r) dr\right). \quad (4)$$

This probability indicates the difference between attenuated and unattenuated projection data. If projection data is multiplied by $\exp(D\mu(r))$, the attenuation along that line of response is corrected and is called the attenuation correction factor (ACF) [14].

Most modern PET scanners have an on-board CT scanner. The CT scan measurements are in Hounsfield unit (HU) but can be converted to attenuation coefficients at the required energy of 511keV for coincidence imaging (μ map). Thus, information from a CT can be used in calculation of ACF [21]. The PET/CT scanner (GE Discovery-600) used in this thesis also uses CT image to estimate attenuation map which is then included in the reconstruction.

2.5 Image Reconstruction

Image reconstruction for PET is a mathematical method of retrieving tracer distribution from sinograms or projections. The basic principles of image reconstruction are the same for 2D and 3D PET data; for simplicity here, 2D case is explained. The

mathematics of projection was first discovered by Radon in 1917 but it took some years for it to be applied to image reconstruction [22], [23].

Filtered back projection and iterative image reconstruction are two widely used image reconstruction methods, which are explained in the following sections.

2.5.1 Filtered Back Projection

Back projection methods were originally developed and used for x-ray CT images and were later applied to PET imaging as well. The back projection method is based on the Radon transform [24]. A Radon transform of an image can be defined as a series of line integrals at different offsets from the origin. A tomographic image can be described as an intensity function with x and y coordinates that can also be expressed by the distance l and angle θ , therefore a line L in (x, y) plane can be defined as

$$L(l, \theta) = \{(x, y) | x \cos \theta + y \sin \theta = l\}. \quad (5)$$

In this case, the line integral of the image function would be

$$g(l, \theta) = \int_{-\infty}^{\infty} \int_{-\infty}^{\infty} f(x, y) \delta(x \cos \theta + y \sin \theta - l) dx dy \quad (6)$$

where $g(l, \theta)$ is the projection image, $f(x, y)$ is the object to be reconstructed and δ is the impulse function. Because of the impulse function, the integral will be equal to zero except along the line L on which $x \cos \theta + y \sin \theta = l$, therefore this function is a representation of the projection at different angles and is known as the continuous Radon transform.

Back projection image reconstruction is illustrated in Figure 6. In this figure, the projection for 5 different angles (forward projection) for the given object are calculated, then from these projections, back projection images are estimated for each angle. The reconstructed image of the object will be the summation of back projection images at all

angles. Since higher frequencies are under-sampled in the projection space, leading to loss of resolution, the reconstructed image is blurred and is not the same as the original object [24]. To overcome the blurriness, another method called filtered back projection (FBP) can be used instead [24].

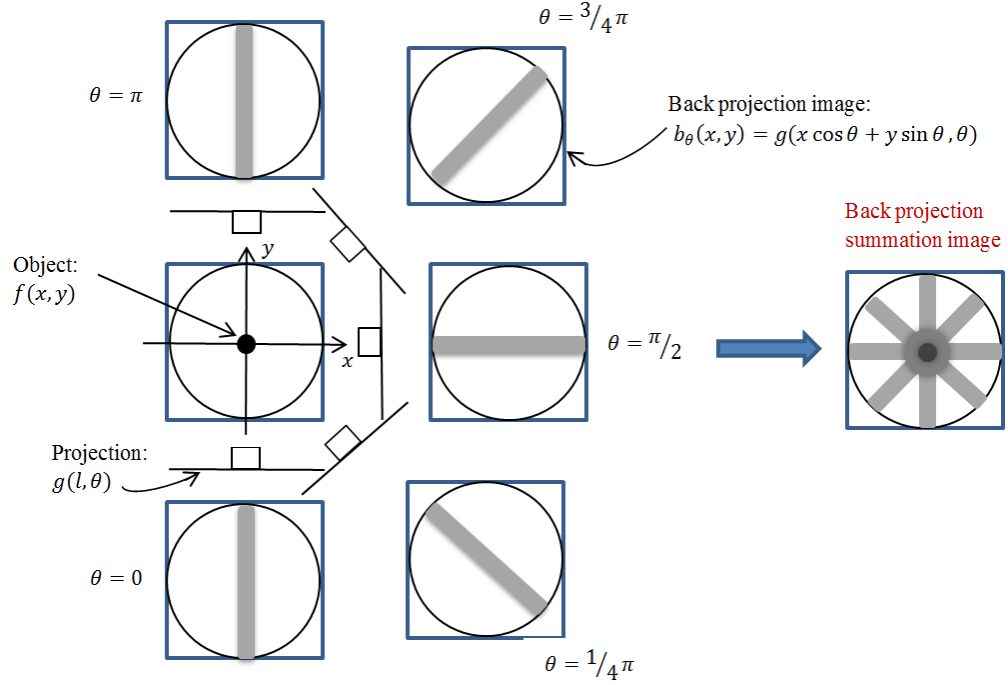


Figure 6. An example of object forward projection and back projection for image reconstruction.

FBP is based on projection-slice theorem (discussed in Appendix A). Based on this theory, a 1D Fourier transform of a projection is a slice of the 2D Fourier transform of the object. The FBP formula is

$$F_{2D}^{-1}\{F(u, v)\} = \int_0^\pi \left[\int_{-\infty}^\infty |\rho| G(\rho, \theta) \exp(j2\pi\rho l) d\rho \right] d\theta \quad (7)$$

where $G(\rho, \theta)$ is the 1D Fourier transform of a projection, $|\rho|$ is a ramp filter and $F(u, v)$ is 2D Fourier transform of the object $f(x, y)$ and $u = \rho \cos \theta$, $v = \rho \sin \theta$. There are four steps in FBP method; first the 1D Fourier transform for each projection is calculated. Then the 1D Fourier transform of projections are filtered by multiplying the Fourier transform

of each projection by the ramp filter. Next the inverse Fourier transform of the filtered projections are computed and finally the data is back projected for each projection and summed together [14], [24].

There are some drawbacks to this method; the ramp filter amplifies statistical noise present at higher frequencies. One method to tackle this problem is to modify the shape of the ramp filter by some window function; however, this process will decrease spatial resolution in the reconstructed image [14].

2.5.2 Iterative Reconstruction

Instead of using analytical solutions for reconstructing images from projection data, there are model-based methods that use the information about the probability distribution of a photon being detected to iteratively estimate the reconstructed image. Iterative reconstruction methods typically use a statistical model including knowledge that the number of measured events using radiation detectors follows a Poisson distribution. For these methods, prior information such as image smoothness or knowledge of anatomical structures in the image can further improve the reconstructed image [3].

In model-based iterative PET image reconstruction methods [3], measured PET projection data \mathbf{y} can be linearly modeled by an unknown source distribution \mathbf{f} and a projection matrix \mathbf{P} as follows

$$\bar{\mathbf{y}} = E[\mathbf{y}] = \mathbf{P}\mathbf{f} + \mathbf{r} + \mathbf{s} \quad (8)$$

where \mathbf{r} refers to random events, \mathbf{s} is the scatter events and $E[\mathbf{y}]$ is the expected value of \mathbf{y} . The element p_{ij} of matrix \mathbf{P} is the average probability of detecting an emission from voxel site j at LOR i . This equation remains the same if \mathbf{f} is substituted by emission image \mathbf{x} as

$$\bar{\mathbf{y}} = \mathbf{E}[\mathbf{y}] = \mathbf{P}\mathbf{x} + \mathbf{r} + \mathbf{s}. \quad (9)$$

The reconstruction problem therefore effectively reduces to approximately solving equation (9) for image \mathbf{x} . To solve this equation, the conditional probability or likelihood function for \mathbf{y} given emission image \mathbf{x} is estimated by independent Poisson distributions given as [3]

$$\mathbf{Prob}(\mathbf{y}|\mathbf{x}) = \prod_{i=1}^M e^{-\bar{y}_i} \frac{\bar{y}_i^{y_i}}{y_i!}, \quad (10)$$

where M is the total number of lines of response. The maximum likelihood (ML) estimate of the image \mathbf{x} can be found by maximizing equation (10) or its log likelihood equivalent given as

$$\mathbf{L}(\mathbf{y}|\mathbf{x}) = \sum_{i=1}^M y_i \log(\bar{y}_i) - \bar{y}_i - \log(y_i!). \quad (11)$$

Maximizing $\mathbf{P}(\mathbf{y}|\mathbf{x})$ and $\mathbf{L}(\mathbf{y}|\mathbf{x})$ produce identical results since a log function is a monotonic function. The ML estimate of the emission image \mathbf{x} is found by

$$\hat{\mathbf{x}} = \underset{\mathbf{x} \geq 0}{\operatorname{argmax}} \mathbf{L}(\mathbf{y}|\mathbf{x}). \quad (12)$$

Expectation maximization (EM) algorithm, proposed by Shepp and Vardi [25], is derived to find the solution to equation (12) by the iterative update

$$\mathbf{x}^{n+1} = \frac{\mathbf{x}^n}{\mathbf{P}^T \cdot \mathbf{1}_M} \left(\mathbf{P}^T \frac{\mathbf{y}}{\mathbf{P}\mathbf{x}^n + \mathbf{r}} \right) \quad (13)$$

where $\mathbf{1}_M$ is a vector of length M with all elements being 1, n denotes iteration number and the superscript “ T ” denotes matrix transpose. The vector multiplication and division are element-wise operations [9]. Equation (13) can be also presented using Hadamard product and division operators [26] and would be

$$\mathbf{x}^{n+1} = (\mathbf{x}^n \oslash (\mathbf{P}^T \mathbf{1}_M)) \odot (\mathbf{P}^T (\mathbf{y} \oslash (\mathbf{P} \mathbf{x}^n + \mathbf{r}))). \quad (14)$$

A problem common to ML methods is ill-conditioning, meaning that the solutions are sensitive to small changes in the data causing the estimates to have high variance. This ill-conditioning can be seen in practice through the ‘checkerboard’ effect in the ML images for high iteration numbers. A solution to the ill-conditioning problem is to add a smoothing penalty to the likelihood function and compute a penalized ML solution [3]. Therefore equation (12) could be changed to

$$\hat{\mathbf{x}} = \underset{\mathbf{x} \geq 0}{\operatorname{argmax}} \mathbf{L}(\mathbf{y}|\mathbf{x}) - \beta U(\mathbf{x}) \quad (15)$$

where β is the parameter for controlling the strength of the regularizer on the result and $U(\mathbf{x})$ is the penalty function. The penalty term would impose the estimate of likelihood function to be the most probable one in terms of prior expectations of image structure or smoothness. Different penalty functions are introduced and proposed in the literature and range from a simple Gaussian model to highly nonconvex functions that result in more sharply defined boundaries in the image [27]–[29]. The choice of penalty function has a strong impact on the appearance of the reconstructed images.

The maximum likelihood expectation maximization (MLEM) algorithm has attractive properties; however, it also converges very slowly. There are alternative methods to the EM algorithm that converge faster. In the ordered subsets EM (OSEM) method proposed by Hudson and Larkin [30], projection data is divided into a number of separate subsets and then the EM algorithm is consecutively applied to each subset in each iteration. This will reduce the convergence time over initial MLEM and causes OSEM to be clinically used as the reconstruction algorithm in PET machines [3].

2.6 Dynamic PET Imaging

As mentioned earlier, PET imaging is molecular as opposed to anatomical imaging, which means its purpose is to measure the concentration of radioactive tracer within the body to be able to quantify the interaction of the tracer with a physiological or biological process. PET images provide useful information for clinicians in both static (single time point) and dynamic (over time) forms. The use of static and dynamic images depends on the molecular process of interest. Static imaging determines where the tracer is located at a particular point in time where the physiological processes defined by the tracer chemistry are most prevalent. On the other hand, dynamic imaging can provide considerably more information about *in vivo* biology by determining both the temporal and spatial pattern of tracer uptake. Dynamic imaging can also mitigate several potential sources of error that occur in static imaging.

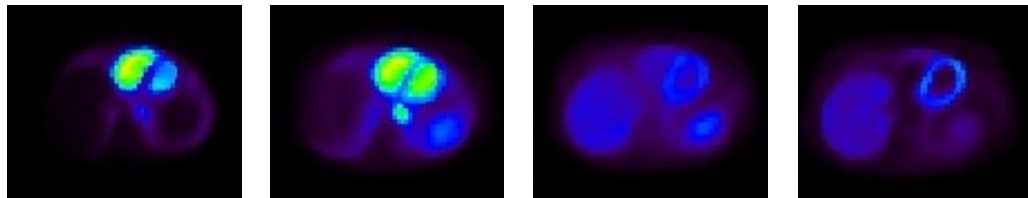


Figure 7. Four different time frames (30 s, 50 s, 2 minutes, 40 minutes) in a dynamic PET series of heart images using C-11-HED tracer. The sequence of frames starts from the left towards the right.

The acquisition time for dynamic PET scans depends on tracer half-life, the temporal kinetics of the tracer, the biological distribution, and the analysis model proposed. In general, the blood and tissue concentration of the radiotracer will change most rapidly early after intra-venous injection; therefore, most dynamic PET imaging sequences have finer time sampling early after injection and wider time frames (longer time for each frame) at

later time points [31]. Figure 7 shows an example of different time frames for a dynamic PET image of the heart region.

2.7 Time Activity Curve

Time activity curve (TAC) is the plot of radioactivity concentration in a region of interest over time. TAC is generated by using dynamic PET data to measure the tracer concentration in a tissue or organ in sequential time frames. For cardiac images, TACs are typically measured for arterial blood and left ventricle wall. An example of a TAC is shown in Figure 8.

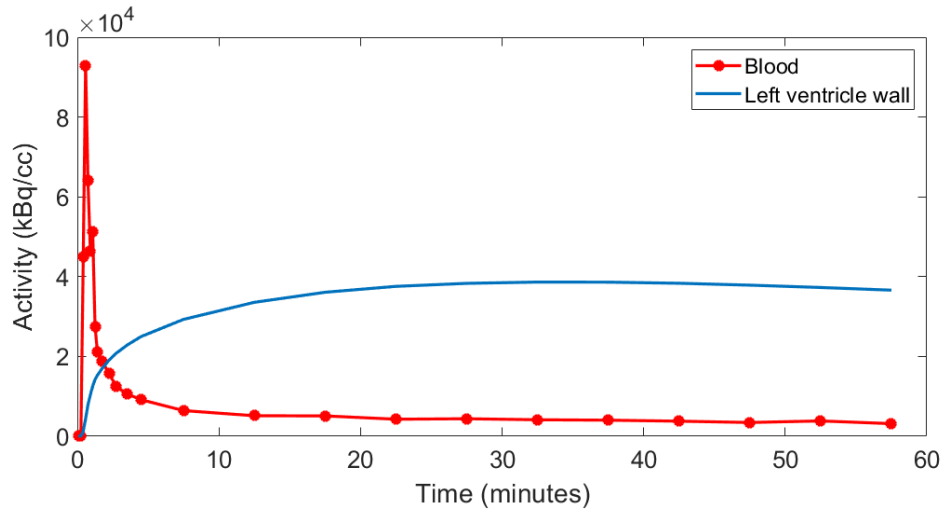


Figure 8. Time Activity Curve for blood cavity and left ventricle wall. The mid-frame sampling time-points are shown on the blood curve

2.8 The Compartment Model

Compartment models are a mathematical method of describing the transport of material in dynamic systems. In this work, compartment models are biological processes that relate the image data to the tracer dynamics for possible states that the tracer can take. Each state described using these models can be considered as a compartment, which is the distribution of a tracer at a specific organ or tissue and time and can be defined by a differential equation. Coefficients in differential equations are based on the exchange rates

and reflect the average state of kinetic properties of the tracer in the system [32]. For the systems of interest, the input to the system is the measured arterial blood curve which is radioactivity concentration in the blood as a function of time. But determining the blood curve is a difficult task since it needs a direct measurement of the input function using arterial blood samples, which is not always feasible. Fortunately, in cardiac imaging applications the arterial input function can be sampled easily using image regions positioned in the cavities of the left ventricle or atrium. By comparing the input function to the measured data, the coefficients for the differential equations describing the exchange between compartments can be estimated.

In tracer studies, certain assumptions are made about the behavior of the tracer [33]:

- 1) The amount of injected tracer is very small, meaning no physiological changes are made on the system by the tracer injection.
- 2) There are no isotope effects, which means labeling tracer molecules with the radionuclides does not change their biological properties.
- 3) Physiological process under investigation can be characterized by the tracer's chemical properties.
- 4) The parameters of the model are time invariant during the study period.
- 5) It is mostly assumed that all organs see the same input function, particularly in PET imaging.

Kinetic models for PET imaging are typically one, two, or three-compartment models in which the blood curve is the input function to the model [33]. Then comparing the output of the model to the experimentally obtained PET data, values for kinetic parameters of the model can be estimated and thus information about binding, delivery and

other information contributing to the measured PET signal can be extracted. A one-tissue compartment model (sometimes referred to as two-compartment model), describes the bidirectional flux of tracer between blood and tissue as shown in Figure 9. It should be noted that in kinetic modeling, blood flow is usually calculated in terms of perfusion of tissue, which means it is described as volume per unit time (flow-rate) per unit volume of tissue. Thus, the words *flow* and *perfusion* are often used interchangeably in PET [33].

The model is characterized by the time-varying tracer concentration in tissue $C_t(t)$ and in blood $C_b(t)$ and the first-order kinetic rate constants (K_1, k_2). $C_b(t)$ and $C_t(t)$ will be written as C_b and C_t for simplicity. It is also assumed that within each compartment (blood and tissue) the tracer has homogeneous distribution. The net tracer flux into tissue for one-tissue compartment model equals the flux entering the tissue minus the flux leaving the tissue as shown in

$$\frac{dC_t}{dt} = K_1 C_b - k_2 C_t. \quad (16)$$

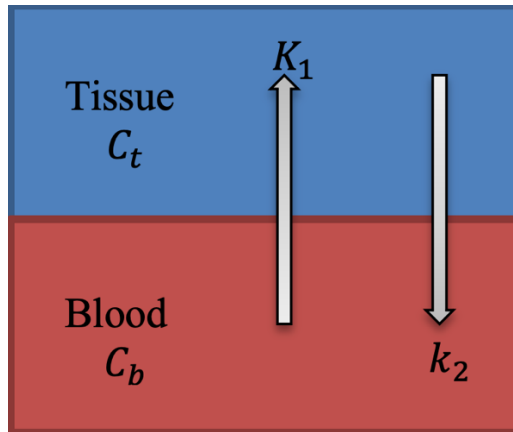


Figure 9. This one-tissue compartment model describes the bidirectional flux of tracer between blood C_b and tissue C_t .

For blood flow quantification, the first task is to define the path the tracer takes from the input function (blood) to the important components (tissues/systems), considering

extraction from those components. Knowing all of these, a compartment model for the system can then be formulated. As stated earlier, tracer uptake in the myocardium is the region of interest for heart blood flow imaging and the input function is the arterial blood supply to the heart. By comparing the measured blood input function to the myocardium TAC function, the parameters of the compartment model are determined.

2.9 Previous Work

As explained earlier, maximum likelihood expectation maximization uses EM algorithm to reconstruct the image and it includes Poisson statistical noise model in tomographic reconstruction [25]. This method includes a Poisson model in the reconstruction and results in a closed form iterative update for reconstruction [25]. Different variations of ML algorithms were developed afterwards that tried to overcome the shortcomings of MLEM. As explained in Section 2.5.2, MLEM is slow to converge and therefore a faster variation was proposed by Hudson and Larkin called ordered subset expectation maximization (OSEM) [30]. Also, it was mentioned that ML-based algorithms are ill-posed because of low count statistics, resulting in reconstructed images that can suffer from high noise.

To improve PET image quality, several methods have been proposed from filtering the reconstructed image to modeling the noise in the reconstruction algorithm and adding it as a smoothing penalty to the likelihood function [34]–[36]. These methods mostly include prior information to improve PET image quality [3]. Anatomical information from other image modalities, such as CT or MRI, can be used as prior information. Incorporating anatomical images is a well-known method to increase PET resolution [5], [37]–[45].

Several methods have used anatomical information as a regularizer in the likelihood function. Bowsher [46] proposed a model that imposes greater smoothing among nearby voxels in the PET image when they have higher similarity in MRI signals. Several papers use the concept of non-local means (NLM) for defining their regularizer term. Nguyen and Lee [39] developed a non-local regularizer where the weight is defined based on similarity between two patches in the PET image and also the similarity between two patches centered in an anatomical image. Compressed sensing reconstruction was used to explore the sparsity in CT image sequences to reconstruct dynamic CT images from highly under sampled projection data sets [47]. The same technique can be applied to PET image reconstruction as well [48].

An alternative approach to defining a regularizer is to add a denoising step at the end of image reconstruction. A NLM filter has been applied in [49] for denoising the reconstructed image. Newer methods have applied deep learning to PET image denoising [50] where a deep neural network is trained for PET image denoising. The proposed pre-training along with fine-tuning can assist with limited training data available.

Moreover, the noise in PET images can be tackled by incorporating image prior information directly into the forward projection model. The kernel methods model the prior information and uses them during image reconstruction, avoiding further post-processing and reducing bias [8], [9], [51]. The kernel-based expectation maximization (KEM) method proposed by Wang and Qi incorporates prior information in a form of an image feature space [9]. Image intensity for each pixel of a PET image is a function of a set of features which are derived from prior information. This function is defined using a kernel method and is assumed to be linear in kernel space. The features can be produced in many

ways: it can be from dynamic PET series [9], [52]–[54] as well as from anatomical images, such as MRI [8], [51], [55]–[57].

Hutchcroft et al. [8] derived the Gaussian kernel directly from the co-registered MR image and embedded it in the iterative update of the image. There are also methods which try to benefit from a combination of both dynamic and MR-based kernels. Gong et al. [58] have combined a dynamic kernel and MR-based kernel through a structural similarity matrix. Wang [54] has extended the spatial kernel method [9] into a more generalized spatiotemporal kernel method. In [51], the authors defined the kernel to be a Kronecker product of the spatial kernel function derived from MRI with a temporal basis function from the time activity curve of the dynamic PET.

Huang [53] has combined denoising with kernel-based reconstruction by applying non-local means denoising after each iteration of KEM update. In that paper, the author defined the kernel as a multiplication of the spatial kernel with a temporal kernel that is obtained by comparing feature vectors of the different frames. Bland et al. [56] have shown that with the help of the MR derived kernel there can be a significant dose reduction in the amount of tracer needed to be injected for PET imaging and the quality of the reconstructed image would be the same as full dose PET imaging with MLEM reconstruction. In another publication by them, Bland et al. [57] select the feature vectors not only from MR intensity values but also based on their spatial location, which will result in preserving PET unique features better than the methods which are only based on the intensity of the MR image.

2.10 Summary

In this chapter, the basics physics of PET systems and methods of reconstructing an image from sinograms were presented. There are some specific physical corrections

needed before being able to reconstruct a quantitatively accurate image from sinogram. Iterative reconstruction methods were explained and MLEM algorithm was introduced as a widely used iterative reconstruction method along with its faster version (i.e., OSEM) which is used in most of the clinical PET/CT scanners. Noise in the reconstructed PET images was described and some literature review on the methods trying to eliminate it was given. We also talked about compartment models derived from dynamic PET image from which we can estimate values for kinetic parameters. Now we can move on to the kernel method reconstruction and its effect on noise reduction.

Chapter 3 : Kernel Based Image Reconstruction using Gaussian Kernel

Part of this chapter has been previously published in a conference proceeding. © 2019 IEEE. Reprinted, with permission, from Zahra Ashouri, Chad R. Hunter, Benjamin A. Spencer, Guobao Wang, Richard M. Dansereau, Robert A. deKemp “Kernel-Based Reconstruction of C-11-Hydroxyephedrine Cardiac PET Images of the Sympathetic Nervous System,” 2019 41st Annual International Conference of the IEEE Engineering in Medicine and Biology Society (EMBC), July 2019. Some modifications have been made.

3.1 PET Image Reconstruction using Kernel in EM.

As explained in Section 2.5.2, the probability of measuring annihilation events follows a Poisson distribution. The expectation maximization algorithm maximizes the log-likelihood function and therefore helps to find the ML estimate of image \mathbf{x} and the result is an iterative update of the image given in equation (13) in Chapter 2 [25].

For kernel-based expectation maximization, the prior information in the image representation is encoded by using the kernel. The basic idea is to represent the PET image \mathbf{x} by a linear function of transformed prior information in a high-dimensional space. A feature vector \mathbf{f}_j is identified for pixel intensity x_j and can be defined by a linear combination of feature vectors of the neighboring pixels. In this chapter, the kernel method introduced by Wang et al. [9] was used for the purpose of improving the left ventricle wall representation. Images of the heart are affected by both cardiac and respiratory motion, which is always present, and because of it, high quality PET images are hard to achieve. In

this chapter, dynamic kernel-based method is applied on cardiac images with C-11-hydroxyephedrine (HED) tracer to see if superior quality in comparison to clinically used OSEM method can be achieved in this tissue. Since the rest of my research is based on the kernel method, establishing its usefulness in its original form for this cardiac dataset is the first step for further improvements. Then, I focus on the drawbacks of Gaussian kernel and try to find better kernels.

3.2 Feature vectors

To define feature vectors, composite frames are made by summing multiple non overlapping time frames from the dynamic image series as shown in Figure 10. The summation of raw projection data from multiple time frames of the dynamic series forms composite frames. This helps to preserve spatial information apparent in most frames at the expense of losing temporal information.

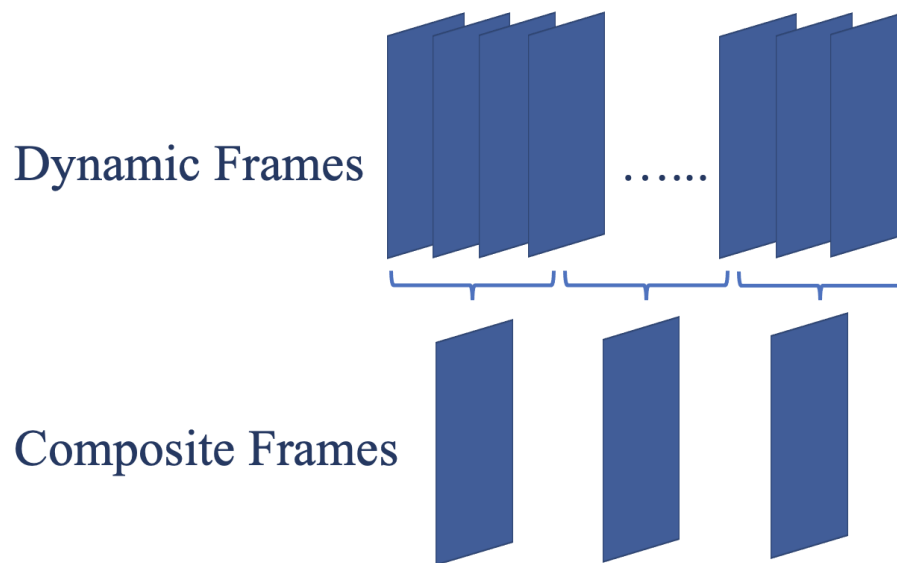


Figure 10. Composite frames made by summing dynamic frames.

The tracer will go through three different phases when injected into the body. First the tracer is in the blood, then it is in transition and finally it is in the tissue, therefore

choosing three composite frames seems reasonable. Wang et al. [9] have also concluded that three composite frames is a plausible option.

A compromise is needed in selecting the number of composite frames. A large number of composite frames means that fewer time frames are averaged to form each composite frame. This will not reduce noise sufficiently in composite frames. On the other hand, to have a very small number of composite frames (one or two), more time frames are averaged to form the composite frames, and this will reduce noise significantly. But it will make the kernel ineffective because temporal information related to redistribution of the tracer to different tissues may be lost. Composite frames should preserve the image contrast and reduce the noise (noise reduction is due to temporal averaging) at the same time. These composite frames are then reconstructed using the standard OSEM algorithm, which is widely used clinically for PET image reconstruction. Reconstruction of composite frames is fast as there are fewer number of frames in comparison to the whole dynamic series. The pixel values in the reconstructed composite frames form the feature vectors as

$$\mathbf{f}_j = [\tilde{x}_{j,1}^{comp}, \tilde{x}_{j,2}^{comp}, \tilde{x}_{j,3}^{comp}, \dots] \quad (17)$$

where $\tilde{x}_{j,Q}^{comp}$ is the image intensity value at pixel j in the composite frame Q , $Q = 1, 2, 3, \dots$

From the feature vectors, the kernel is constructed [9]. The neighbourhood can be defined by different methods. One method is to use the k -nearest neighbour (k NN) method [59] which finds the k closest neighbors for each pixel based on the Euclidean distance between \mathbf{f}_j and \mathbf{f}_i . Alternatively, a cubic window centered on a pixel of interest can be used to define where its neighboring pixels are located. Then, the chosen kernel is used to calculate the weights based on the neighboring pixels. For the Gaussian kernel, the (j, l) th element of the kernel matrix for a given composite frame is calculated as

$$\kappa(\mathbf{f}_j, \mathbf{f}_l) = \exp\left(-\frac{\|\mathbf{f}_j - \mathbf{f}_l\|^2}{2\sigma^2}\right) \quad (18)$$

where $\kappa(\mathbf{f}_j, \mathbf{f}_l)$ is a kernel and measures the similarity of normalized features \mathbf{f}_j and \mathbf{f}_l between pixel x_j and pixel x_l in its neighborhood and σ is the chosen standard deviation. The choice of the neighborhood window is based on the voxel size and the tissue being imaged.

Using the kernel coefficients, the reconstructed image is formed using

$$x_j = \sum_{l=1}^N \alpha_l \kappa(\mathbf{f}_j, \mathbf{f}_l) \quad (19)$$

where N is the number of voxels. Equation (19) can be written in matrix form as

$$\mathbf{x} = \mathbf{K}\boldsymbol{\alpha} \quad (20)$$

where $\boldsymbol{\alpha}$ is the kernel coefficient image (the translate of the image in the kernel space) and elements of matrix \mathbf{K} are given by $\kappa(\mathbf{f}_j, \mathbf{f}_l)$ for the (j, l) th element. Different kernels can be used such as the Gaussian or polynomial kernel [9]. The KEM method of reconstruction is derived by substituting (20) in (13). The iterative solution would be updated to

$$\boldsymbol{\alpha}^{n+1} = \frac{\boldsymbol{\alpha}^n}{\mathbf{K}^T \mathbf{P}^T \mathbf{1}_M} \cdot \left(\mathbf{K}^T \mathbf{P}^T \frac{\mathbf{y}}{\mathbf{P} \mathbf{K} \boldsymbol{\alpha}^n + \mathbf{r}} \right) \quad (21)$$

with element-wise multiplication and division. Equation (21) can be presented by Hadamard product and division as

$$\alpha^{n+1} = (\alpha^n \oslash (\mathbf{K}^T \mathbf{P}^T \mathbf{1}_M)) \odot (\mathbf{K}^T \mathbf{P}^T (\mathbf{y} \oslash (\mathbf{P} \mathbf{K} \alpha^n + \mathbf{r}))). \quad (22)$$

This iterative algorithm is similar to MLEM reconstruction with the kernel embedded in the iterative update and can be solved using MLEM or OSEM which uses the same update formula as equation (13) but is applied on subsets.

3.3 Parameter Selection for Gaussian Kernel

As discussed in Section 3.2, from the reconstructed composite frames the features for building the kernel matrix are extracted. Different kernels can be used to calculate the kernel matrix. In this section, similar to Wang et al. [9], a radial Gaussian function is used to calculate the weights on the neighboring pixels as given in equation (18). As explained earlier, the neighborhood can be defined by different methods such as k NN or cubic window. Since the dataset for patients is 3D regional k NN inside a cubic window is used instead of global k NN since it decreases the computational complexity such that the method is more practical for 3D reconstruction [9]. To include the spatial distance between the pixel of interest and neighboring pixels in the cubic neighborhood, a Gaussian spatial weight is given to the pixels in the neighborhood such that the pixel of interest has the largest weight and pixels that are further away in the neighborhood would have smaller weight in the kernel [57]. The weights are calculated based on an isotropic rotationally symmetric Gaussian filter and depending on the input data it can be 2D or 3D. If the data is 2D, such as in simulated studies, a 2D Gaussian weight is calculated and if it is 3D, such as in clinical data, then the Gaussian weights is set to 3D. The equation for 2D case is

$$G(x, y) = \frac{1}{2\pi\sigma_g^2} e^{-\frac{x^2+y^2}{2\sigma_g^2}} \quad (23)$$

where σ_g is the standard deviation of the Gaussian smoothing filter. Since the image is discrete data, a discrete approximation to the Gaussian function needs to be produced. Therefore, a square matrix is formed based on Gaussian smoothing filter with a predefined size. For example, for a 5×5 Gaussian smoothing filter and with $\sigma_g = 1$ the matrix of weights would be

$$\mathbf{h} = \begin{bmatrix} 0.0030 & 0.0133 & 0.0219 & 0.0133 & 0.0030 \\ 0.0133 & 0.0596 & 0.0983 & 0.0596 & 0.0133 \\ 0.0219 & 0.0983 & 0.1621 & 0.0983 & 0.0219 \\ 0.0133 & 0.0596 & 0.0983 & 0.0596 & 0.0133 \\ 0.0030 & 0.0133 & 0.0219 & 0.0133 & 0.0030 \end{bmatrix} \quad (24)$$

For 3D data, this matrix will be 3D and will be derived from a 3D Gaussian smoothing filter. σ_g is chosen based on the dimension of square matrix $\mathbf{h}_{n \times n}$ (or $\mathbf{h}_{n \times n \times n}$) and is set to

$$\sigma_g = \frac{n}{4\sqrt{2\ln(2)}}. \quad (25)$$

Knowing that for a given Gaussian filter, full width half maximum (FWHM) of the filter is $2\sqrt{2\ln(2)}\sigma_g$, equation (25) basically finds σ_g by dividing the size of \mathbf{h} by 2 and then divides this value by $2\sqrt{2\ln(2)}$.

These weights are then multiplied in the calculation of kernel coefficients in (18). Spatial weighting can be excluded when the neighbouring pixels are found based on global k NN. This is because the pixels in the neighbourhood are found based on the pixel intensity value of all the pixels in the image. However, when the data is dynamic volumetric data and is 3D in each time frame, global k NN is not desirable since it is computationally inefficient, and the neighbouring pixels are selected based on a cubic window. Therefore,

in this case, to include the spatial information related to the distance of each pixel in the neighbourhood (x_1) from the pixel of interest (x_j), spatial weighting is used. After this step, to apply a regional k NN between the kernel coefficients derived from cubic neighbourhood, for each voxel k nearest neighbours are selected inside the neighborhood window, and the rest of the coefficients are set to zero.

To define the neighbourhood in regional k NN, different window sizes such as $5 \times 5 \times 5$, $7 \times 7 \times 7$ and $9 \times 9 \times 9$ can be used. The condition here on the window size is that it should contain enough coefficients to apply regional k NN for the selected k value. Larger window size will result in more voxels used for regional k NN and therefore will increase the quality of reconstructed image from the kernel. On the other hand, increasing the size of the neighbourhood window to very large values has the same problem as the global k NN; it increases the processing time and is computationally inefficient. Based on these discussions, $5 \times 5 \times 5$ window might not be large enough and is not a good option. We tested $7 \times 7 \times 7$ and $9 \times 9 \times 9$ and saw no visual difference in the reconstructed images; therefore, since $9 \times 9 \times 9$ increases the processing time, $7 \times 7 \times 7$ window size was chosen for this experiment which contains 343 voxels.

To choose the number of k for regional k NN and Gaussian parameter (σ), different values were tested and the noise was calculated and based on that k and σ were chosen. The result of this comparison is presented later in the chapter.

3.4 Evaluation Method for Patient Data

To evaluate KEM on patient data, i.e., with no ground truth, SNR and contrast are defined as

$$\text{SNR} = \frac{\text{mean(LV)}}{\text{std(Blc)}} \quad (26)$$

$$\text{Contrast} = \frac{|\text{mean(LV)} - \text{mean(Blc)}|}{\text{mean(LV)}} \quad (27)$$

where “LV” makes reference to the left ventricle wall and the blood cavity inside the left ventricle is represented as “Blc” [60]. These regions are shown in Figure 11. The left ventricle wall is segmented using FlowQuant™ software developed at the Ottawa Heart Institute [1] and the mean value of the pixels in the segmented left ventricle wall is calculated. To calculate background noise, the standard deviation of an area inside the blood cavity of the left ventricle is calculated. This area is an ellipsoid with total volume of around 4.7cm^3 . The mean value of this region is used for contrast calculation.

For a better comparison, an ellipsoid area with total volume of around 42cm^3 inside the liver is used for noise calculation as well. This region is not used for SNR and contrast calculation as those measurements are for the left ventricle. The liver is used as another quality measurement for reconstruction method. The liver is expected to be homogeneous; therefore, the standard deviation in this region is an indication of noise level in this region.

Since OSEM is noisy it is usually followed by post filtering in clinics, therefore I have also compared the results with OSEM that includes post filtering. The post filtering is achieved by a Gaussian filter with different FWHM values. This Gaussian filter is part of the GE MATLAB toolbox, and it is an isotropic filter achieved in 2D for each image slice by calculating standard deviation (σ) of the filter from the given FWHM and then the size of the matrix is set to the closest integer value to $(8\sigma + 1)$. The filter matrix coefficients are calculated for the measured size and σ value. Then the image is convolved with this Gaussian filter matrix and the reconstructed image with post filtering is formed.

Kinetic modelling was achieved using a one-tissue compartment model using FlowQuant™ software [1].

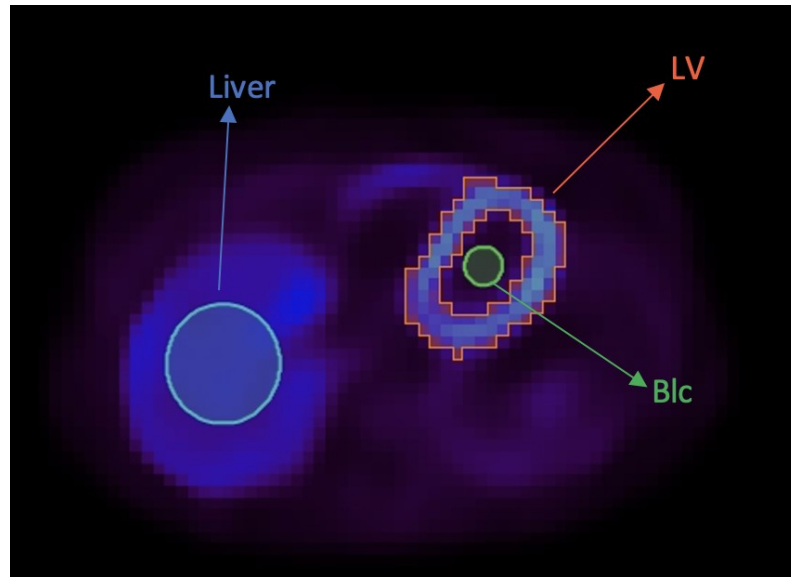


Figure 11. An example showing the left ventricle (LV) wall segment (the area inside the two orange lines) and blood cavity (Blc) ellipsoid area (shown in green) inside the left ventricle and an ellipsoid area inside liver (shown with blue). This image is from KEM reconstruction.

3.5 Experimental Setup

The study population includes dynamic PET imaging acquired from 6 patients (2 normal and 4 ischemic cases) who provided written informed consent to participate in clinical research studies at the University of Ottawa Heart Institute with the research ethics board approval in Appendix D. The data were also anonymized before analysis. The study was done using C-11-HED tracer. This tracer is widely used for myocardium neuronal imaging and has an isotope half-life of 20 min. The scans are acquired by a GE D600 PET/CT scanner. The scan time was 60 min split into 25 time frames defined as follows in order: 9×10 s, 3×30 s, 2×60 s, and 11×300 s showing the number of time frames and their corresponding duration respectively. Final reconstructed images had 47 axial slices of the heart region and the field of view of each slice is 70 cm. These frames are split into three

20 min duration composite frames by summing the frames in 20-minute consecutive intervals: the first composite frame describes the tracer in blood, the second encompasses the transitional phase of the tracer and the final frame describes the uptake in important organs and tissues. As explained earlier, from these composite frames the kernel is produced. This kernel is then used to reconstruct all dynamic frames.

3.6 Result of the Gaussian Kernel

To present the experimental results, first parameters k and σ needs to be chosen. To choose the number of k for regional k NN, different values of k were tested and the standard deviation in blood cavity was calculated (which is an indication of noise) to see the effect of k in noise reduction of the reconstructed image. Standard deviation in blood cavity versus k value has been shown for a few frames in Figure 12. Figure 12 shows that for values larger than 50 the reduction in standard deviation of blood cavity is not considerable especially for later frames, meaning that the percentage of decrease in noise level in this region by increasing k value beyond 50 is negligible considering that larger k value will also increase the processing time. Therefore, for this study k was set to 50.

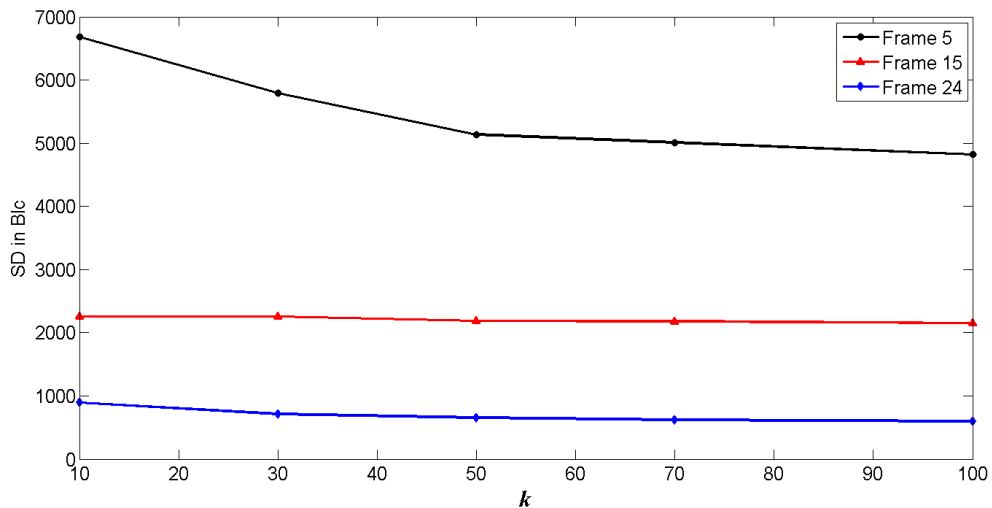


Figure 12. Standard deviation in blood cavity in a few frames and for different k values.

For choosing the Gaussian parameter (σ), different values between 0.1 to 2 were tested and the standard deviation in the blood cavity has been shown for the same frames from the dynamic series for different σ values in Figure 13. Figure 13 shows that for values higher than 1 there is a slight decrease in noise level (standard deviation in blood cavity) for early frames but also a slight increase for values greater than 1 for later frames. Therefore, $\sigma = 1$ was chosen.

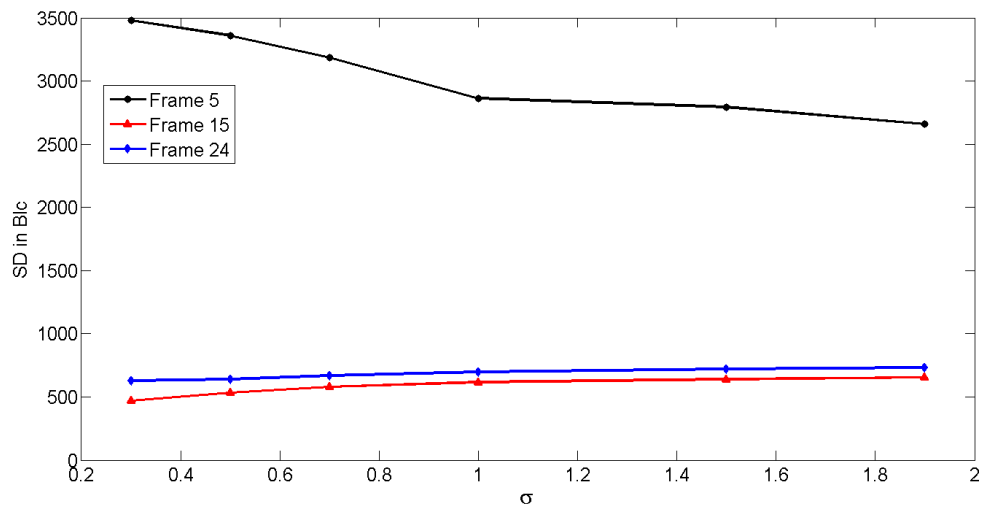


Figure 13. Standard deviation in blood cavity in a few frames and for different σ values.

In Figure 14, SNR versus contrast is shown averaged over all six patients. The values presented in this figure were averaged over the last four uptake frames. In this analysis, I have focused on the latter frames or uptake frames where the tracer uptake is largely in heart tissue as those frames are mostly used for diagnosis. We can see that by increasing the level of post-reconstruction filtering for OSEM, the SNR initially increases as the contrast decreases. After reaching a certain level of post-reconstruction filtering, the SNR decreases with further increased filtering.

Figure 15 shows a transaxial slice of the heart in the last frame for one of the patients showing the results of KEM and OSEM with different levels of post filtering. The

tissue regions from Figure 11 can be seen in this figure as well. As greater post-reconstruction smoothing is used, the image quality and contrast both suffer, and the image becomes blurrier. SNR and contrast values averaged over all patients in each frame are shown in Figure 16 for KEM and OSEM with different post filtering levels. The first two frames are excluded since the activity in the selected areas in those frames was very low and it caused the standard deviation and mean value at these frames to be negligible, thus leading to an unreliable SNR and contrast value. The level of post-reconstruction smoothing is accomplished with a Gaussian spatial filter set to a specific FWHM. In this figure, the index “n” in FWHMn refers to FWHM = n millimeters for the filter.

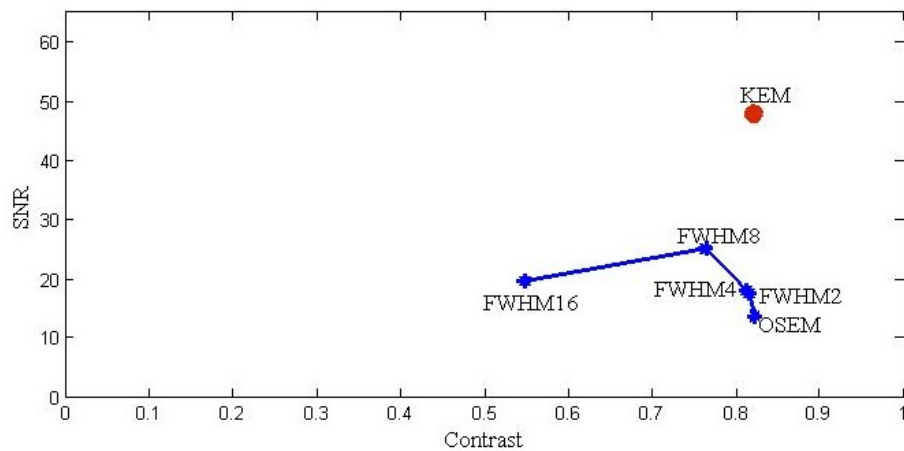


Figure 14. SNR versus contrast for OSEM without and with different smoothing filters (from FWHM2 corresponding to FWHM of the filter equal to 2 mm to FWHM16 referring to FWHM of the filter equal to 16 mm) and KEM for average of last four frames (uptake frames).

Figure 16 shows that the SNR is much higher in KEM than OSEM for most of the post filtering levels, except for 16 mm post filtering, in which for some frames it has higher SNR than KEM. This is because with this amount of post filtering the image is smoothed to a level that the standard deviation inside the blood cavity is very low and thus the SNR is high, but this is not desirable. Figure 15 also shows that with 16 mm post filtering, the

reconstructed image is losing image details and contrast and that is the reason for its low standard deviation in some frames. However, KEM produces a high SNR without a significant impact on contrast and image details.

From Figure 15 and Figure 16, the post filtering which gives the highest SNR among others with no significant reduction in contrast can be chosen and compared with KEM. FWHM = 4 mm (herein called FWHM4) seems to satisfy these conditions. Since the level of post filtering with acceptable result depends on the hardware specifics such as crystal size and intrinsic detector resolution, this 4 mm seems to be the best choice for the whole dataset which is acquired by the same PET scanner.

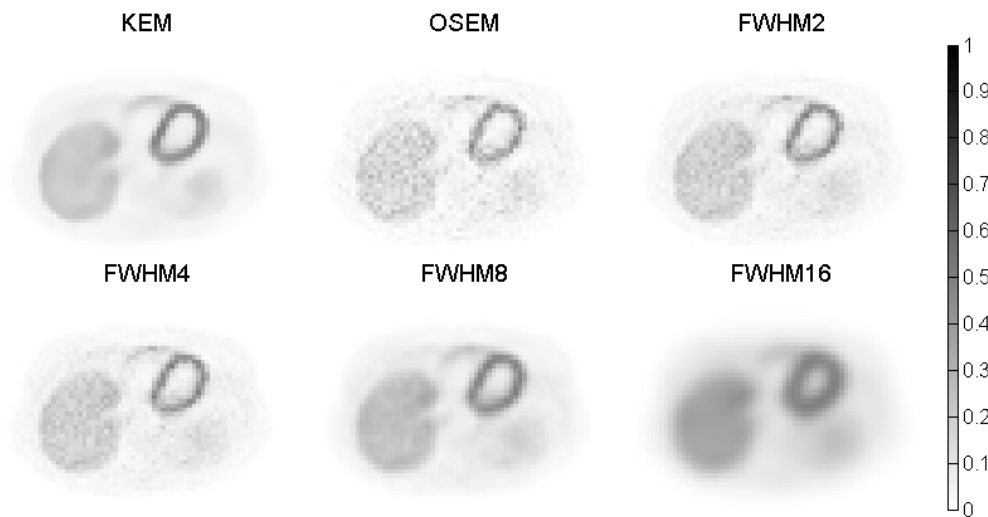


Figure 15. Transaxial slice of the last frame from a normal patient comparing KEM reconstruction with OSEM reconstruction using different levels of post filtering (from FWHM2 corresponding to FWHM of the filter equal to 2 mm to FWHM16 referring to FWHM of the filter equal to 16 mm).

The mean and standard deviation values in different tissue types (blood cavity, heart, and liver) for OSEM with 4 mm post filtering and KEM are presented in Figure 17. This figure shows the result based on normal and ischemic cases, to see if there is any difference between the two categories. From this figure it can be seen that KEM has lower

standard deviation in the blood cavity while it also has higher mean value in the left ventricle wall; this means that KEM suppresses noise better than OSEM with post filtering while it also preserves the signal value (mean value) in the left ventricle wall. The standard deviation in the left ventricle does not change significantly since it is a small structure with high counts and therefore the reconstruction methods do not change its standard deviation noticeably.

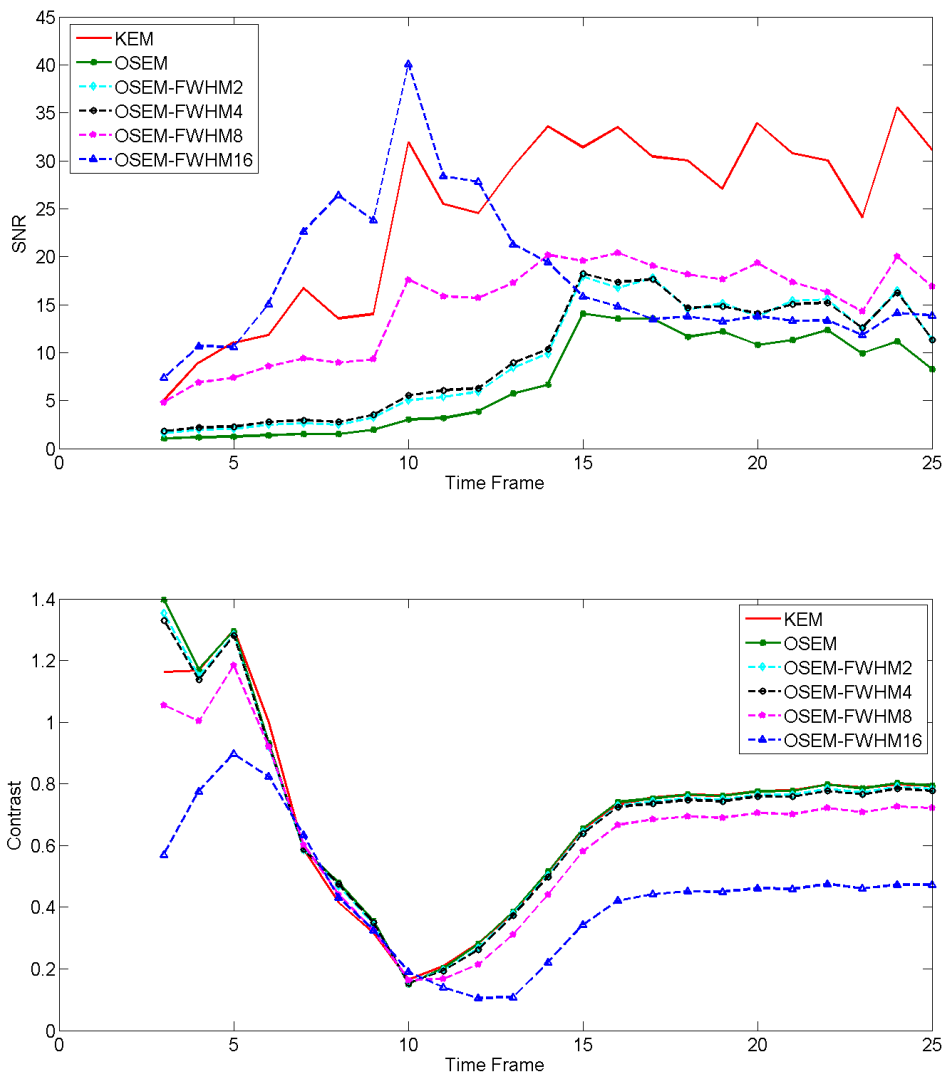


Figure 16. Average SNR and contrast for all the patients for KEM and OSEM with different post filtering.

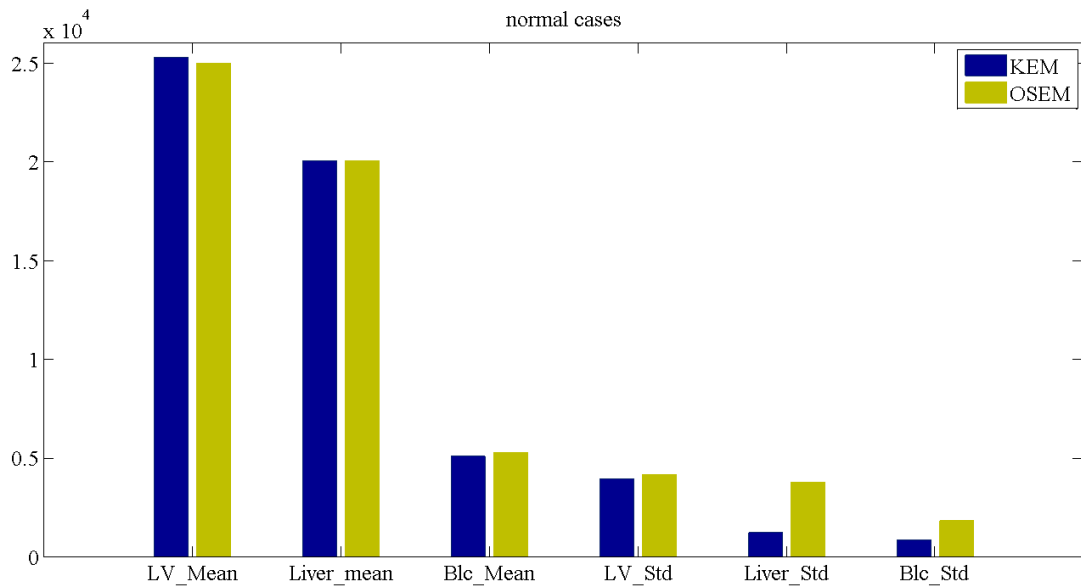
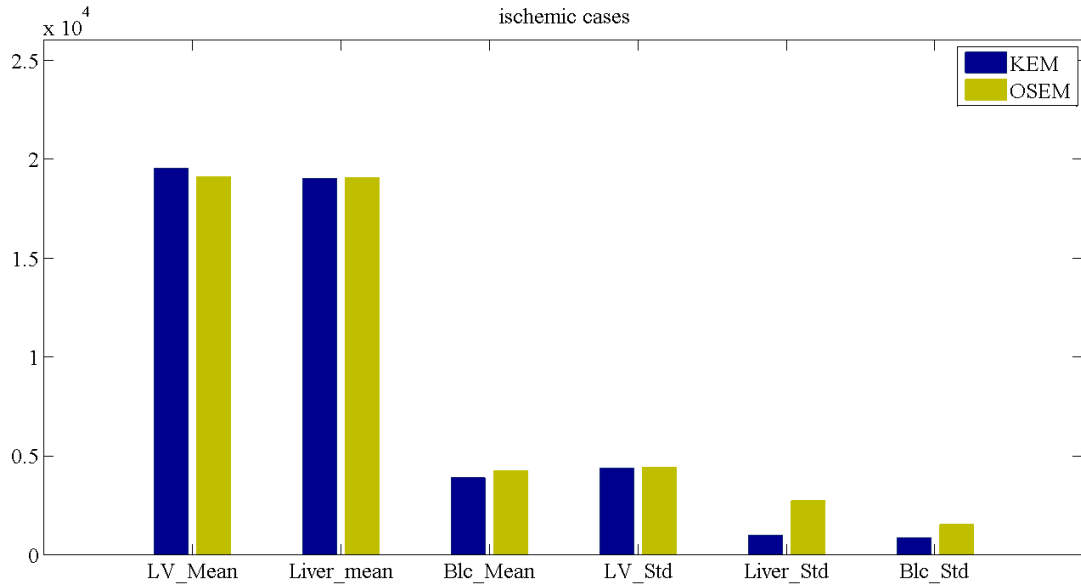


Figure 17. Mean and standard deviation (Std) of late uptake values in different tissue regions for the ischemic patients (top) and normal subjects (down). Liver and blood Std was significantly reduced using KEM compared to OSEM.

Using FlowQuant, the left ventricle heart wall is presented in 3D contour map as shown in Figure 18 derived from the PET image. In this figure the apex is shown. The

“Lat” in the figure refers to lateral wall, “Ant” stands for anterior wall, “Sep” is for septal wall. Different views of the 3D heart wall (posterior view, anterior view and left lateral view) are shown. The color in this figure represents the tracer in the left ventricle wall, the hot color means there is higher tracer uptake in that region and cold colors means the uptake is lower in the region and therefore there may be defects in the left ventricle wall.

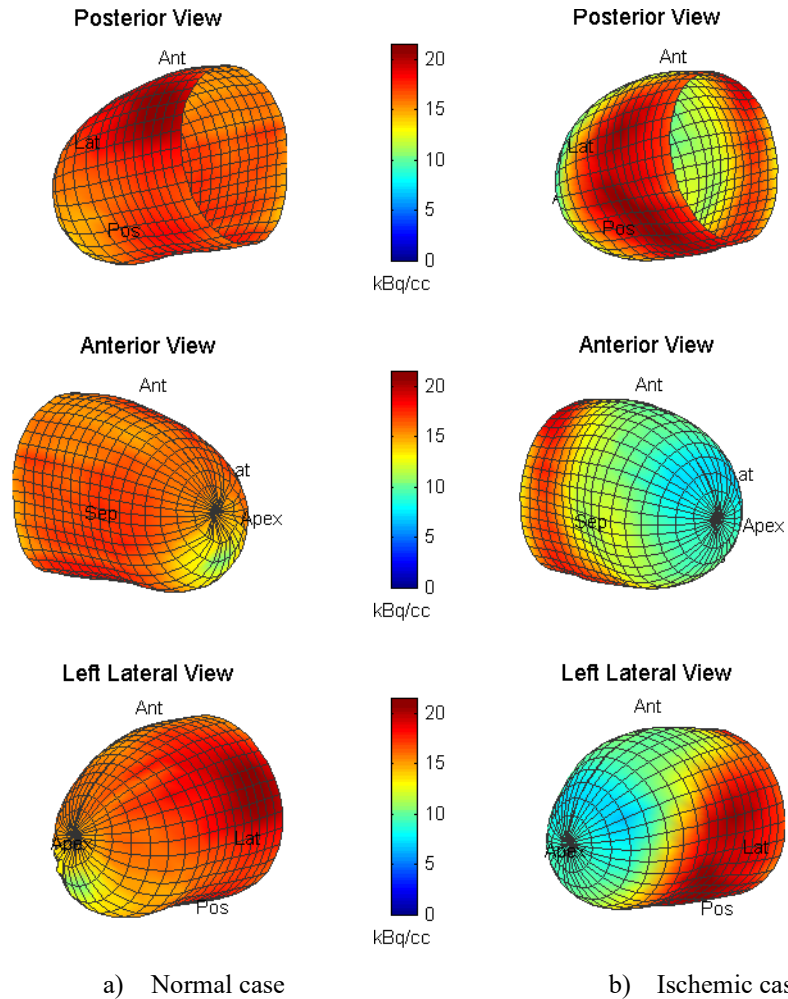


Figure 18. 3D Contour map of the left ventricle wall for an ischemic and a normal case using KEM reconstruction.

To make the analysis of this 3D data easier, the contours are projected onto a 2-dimensional plane called a polar map. The uptake polar maps for one normal and one ischemic patient are shown in Figure 19, in the units of kBq/cc. The middle of the uptake

polar maps is the apex and “S” corresponds to the septal wall, “L” is the lateral wall and “P” represents the posterior wall of the left ventricle. From this image and by comparing the uptake polar maps for OSEM and KEM, we can see that KEM does not change the uptake mean values in the left ventricle.

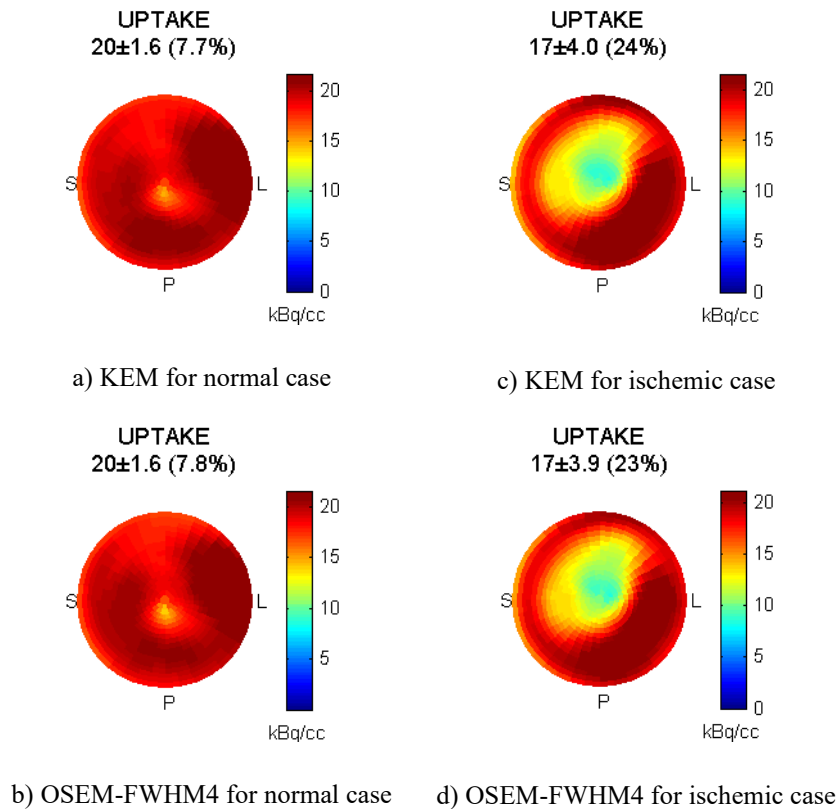


Figure 19. Polar map of the left ventricle distribution in the uptake frames. KEM is quantitatively accurate.

3.7 Summary

In this chapter KEM PET image reconstruction was compared to OSEM for cardiac images of HED tracer. Results show that the kernel-based method can improve SNR for different frames while keeping the contrast high. It should be noted Gaussian kernel might miss small objects or smooth edges and thus result in low resolution on small objects and edges.

Therefore, another kernel which preserves the information in small objects or edges is desirable.

Chapter 4 : Substitutes for Gaussian Kernel

4.1 Admissible Kernels

Mercer's theorem [61] provides the condition for a support vector kernel. The Gaussian kernel satisfies Mercer's condition [62]. As stated in [9] and shown in results in Chapter 3, KEM with the Gaussian kernel results in a reconstructed image with much lower noise compared to clinically used OSEM, but it also removes high frequency details such as edge sharpness and may result in over smoothing of small objects in the image [9]. Therefore, alternatives to the Gaussian kernel may be investigated to better preserve high frequency details. To substitute Gaussian kernel other admissible kernels (\mathbf{K}) should be selected which satisfy Mercer's theorem [61]. A real kernel \mathbf{K} is said to fulfill Mercer's condition if $T_K(s)$ given in

$$T_K(s) = \int \mathbf{K}(x, s) f(x) dx \geq 0 \quad (28)$$

is non-negative for any function $f(x)$ in L^2 space.

This theorem can be represented in the Fourier domain for a translation invariant kernel. A translation invariant kernel $\mathbf{K}(x, x') = \mathbf{K}(x - x')$ is an admissible kernel if and only if [63]

$$F[\mathbf{K}](\omega) = (2\pi)^{-N/2} \int \exp(-j(\omega x)) \mathbf{K}(x) dx \geq 0. \quad (29)$$

This condition implies that the kernel matrix is positive semi-definite [62].

Translation invariant admissible kernels should result in non-negative Fourier transform in (29). Therefore, the kernel needs to be in a form that its Fourier transform would be real and non-negative. This forces the translation invariant kernel $\mathbf{K}(x - x')$ to be real and even, to result in real values for the Fourier transform and then the Fourier

transform needs to be positive. For a function to be even, it should be centered at zero and it should look the same for $+x$ axis and $-x$ axis.

4.2 Kernels

Wavelet analysis will help approximate a signal by a family of functions generated by dilations and translations of a function called the mother wavelet. Wavelets have good energy compaction and have been used to improve support vector machines for machine learning [63]. Thus, the wavelet kernel is expected to enhance kernel-based PET image reconstruction, given the kernel method for image reconstruction shares a similar spirit as kernel machines. The hypothesis is that a wavelet kernel will not over smooth small objects in the reconstructed image. Here a few wavelets which satisfy Mercer's condition are investigated. The Ricker wavelet [64], Morlet wavelet [65] and Meyer wavelet [66] are among them. Some biorthogonal wavelets also have even functions. These wavelets are tested and are compared in terms of SNR value of the reconstructed image and the visual quality.

The closed form formula for the Ricker wavelet is

$$\psi_{Ricker}(t) = \frac{2}{\sqrt{3\sigma\pi}^{1/4}} \left(1 - \left(\frac{t}{\sigma}\right)^2\right) e^{-\frac{t^2}{2\sigma^2}}. \quad (30)$$

Figure 20 shows the Ricker wavelet function. The Fourier transform of this wavelet is

$$\psi_{Ricker}(w) = \frac{2}{\sqrt{3\sigma\pi}^{1/4}} \sigma^3 w^2 e^{-\frac{1}{2\sigma^2 w^2}} \quad (31)$$

which is always positive and therefore the Ricker wavelet satisfies Mercer's condition.

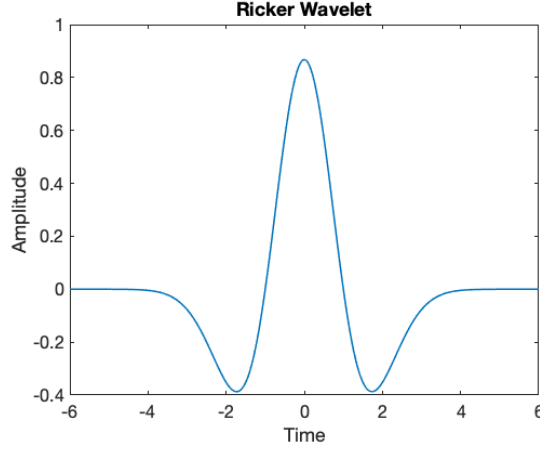


Figure 20. Ricker wavelet function.

Similar to the method used to define the radial Gaussian kernel [9] in equation (18), the radial Ricker wavelet kernel would be

$$\mathbf{K}(\mathbf{f}_j, \mathbf{f}_1) = \frac{2}{\sqrt{3\pi}\pi^{1/4}} \left(1 - \frac{\|\mathbf{f}_j - \mathbf{f}_1\|^2}{\sigma^2} \right) \exp\left(-\frac{\|\mathbf{f}_j - \mathbf{f}_1\|^2}{2\sigma^2}\right). \quad (32)$$

Another even wavelet tested here is the Meyer wavelet. An explicit expression of the Meyer wavelet is [67]

$$\psi_{Meyer}(t) = \psi_1(t) + \psi_2(t) \quad (33)$$

where

$$\psi_1(t) = \frac{\frac{4}{3\pi} \left(t - \frac{1}{2}\right) \cos\left[\frac{2\pi}{3} \left(t - \frac{1}{2}\right)\right] - \frac{1}{\pi} \sin\left[\frac{4\pi}{3} \left(t - \frac{1}{2}\right)\right]}{\left(t - \frac{1}{2}\right) - \frac{16}{9} \left(t - \frac{1}{2}\right)^3} \quad (34)$$

and

$$\psi_2(t) = \frac{\frac{8}{3\pi} \left(t - \frac{1}{2}\right) \cos\left[\frac{8\pi}{3} \left(t - \frac{1}{2}\right)\right] + \frac{1}{\pi} \sin\left[\frac{4\pi}{3} \left(t - \frac{1}{2}\right)\right]}{\left(t - \frac{1}{2}\right) - \frac{64}{9} \left(t - \frac{1}{2}\right)^3}. \quad (35)$$

An even version of the wavelet function ($\psi_{Meyer}(t)$) would be ($\psi_{Meyer}(t - \varepsilon)$) where ε is a number and this even version is shown in Figure 21. A mother wavelet is used

in its shifted versions, therefore even if a shifted version of the wavelet is an even function, then that wavelet can be used to construct a kernel which is an admissible kernel.

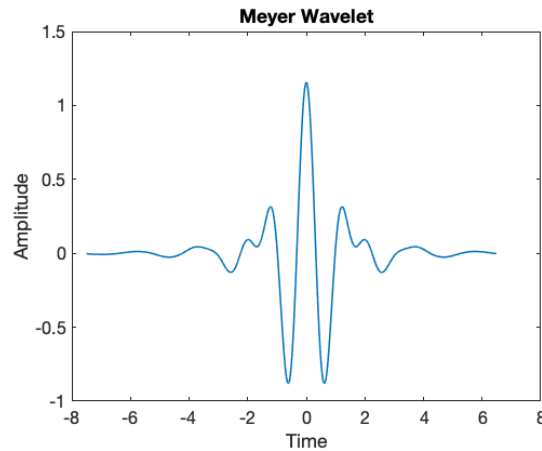


Figure 21. An even version of Meyer wavelet function (shifted in time).

The positivity of the Meyer wavelet needs to be checked. Since the Fourier transform of the given ψ is not easily computable, the eigenvalues of the kernel built from the Meyer wavelet were investigated. Because the eigenvalues are all positive for the calculated kernels, it can be concluded that the kernel constructed from the Meyer wavelet with the given data is positive semi-definite and is therefore an admissible kernel. Wavelet decomposition is achieved in MATLAB using the Meyer wavelet. The feature vector is formed by calculating the difference between each pixel and all its neighbouring pixels, this vector is then decomposed using the Meyer wavelet. The decomposition coefficients for the pixel of interest, form a row of the kernel corresponding to the pixel of interest. For all the pixels in the image the decomposition coefficients are formed to complete the kernel.

Biorthogonal wavelets are another option for a mother wavelet. In biorthogonal wavelets, one wavelet is used in analysis $\tilde{\psi}$ and another one is used for synthesis ψ . The coefficients of a signal s is represented as

$$\tilde{c}_{j,k} = \int s(x) \tilde{\psi}_{j,k}(x) dx \quad (36)$$

and the signal s would be calculated by

$$s(x) = \sum_{j,k} \tilde{c}_{j,k} \psi_{j,k} \quad (37)$$

The analysis and synthesis wavelet are related by duality in the following form

$$\int \tilde{\psi}_{j,k}(x) \psi_{j',k'} dx = 0 \text{ when } j \neq j' \text{ or } k \neq k' \quad (38)$$

$$\int \tilde{\phi}_{0,k}(x) \phi_{0,k'} dx = 0 \text{ when } k \neq k' \quad (39)$$

where ϕ is the scaling function. Even versions of wavelet functions for Bior 2.4 and Bior 2.6 are shown in Figure 22 [68].

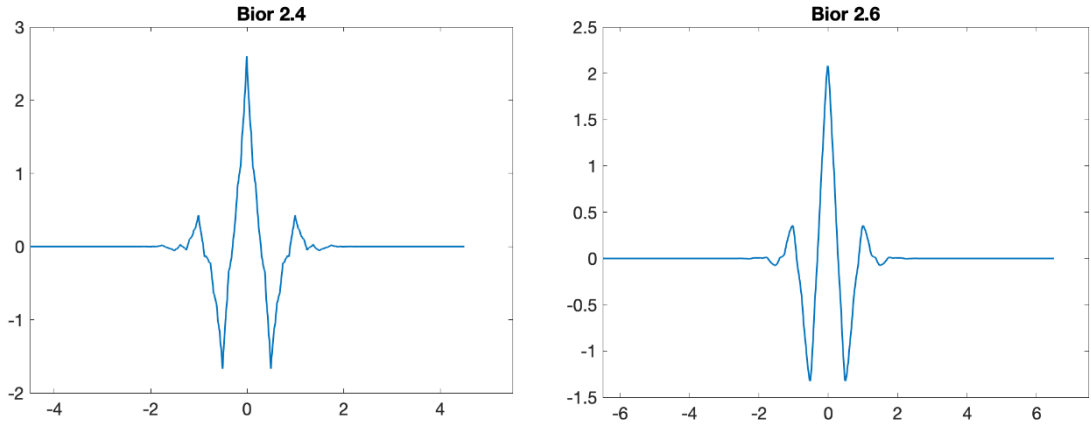


Figure 22. Even versions of biorthogonal 2.4 and 2.6 wavelet functions (decomposition functions).

Mercer's condition for the biorthogonal wavelets were checked like the Meyer wavelet and the eigenvalues for both cases of the biorthogonal wavelet were positive and therefore they are admissible kernels for this goal. The kernel is constructed similar to the Meyer wavelet except that the decomposition is achieved with biorthogonal wavelets.

Another wavelet is the Morlet wavelet [68]. A real Morlet mother wavelet is used to have an even kernel. In general, a real Morlet mother wavelet consists of a sinusoid

$[\cos(\omega z)]$ windowed by a Gaussian function $[\exp(-\frac{z^2}{\omega_b})]$, with ω_b being the bandwidth parameter and ω the central frequency. Typically, in literature, $\omega_b = 2$, therefore the real Morlet mother wavelet would be as follows

$$\psi_{Morlet}(t) = \cos(\omega t) \exp\left(-\frac{t^2}{2}\right). \quad (40)$$

The central frequency, ω , is related to number of significant oscillations within the Gaussian window [69]. The authors in [69] have shown that standard values of ω cannot detect the features due to smearing of the information over the larger number of oscillations. The Morlet wavelet with a few different ω values are shown in Figure 23. The translation invariant kernel constructed with the wavelet in equation (40) would be

$$\mathbf{K}(\mathbf{f}_j, \mathbf{f}_1) = \prod_{i=1}^Q \left[\cos\left(\omega \left(\frac{\mathbf{f}_j^i - \mathbf{f}_1^i}{a}\right)\right) \exp\left(-\frac{(\mathbf{f}_j^i - \mathbf{f}_1^i)^2}{2a^2}\right) \right] \quad (41)$$

where $(\mathbf{f}_j^i - \mathbf{f}_1^i) \in \mathbb{R}^Q$. In this work, Q is the number of composite frames.

This translation invariant kernel satisfies Mercer's condition [62] and the proof is provided in Appendix B.

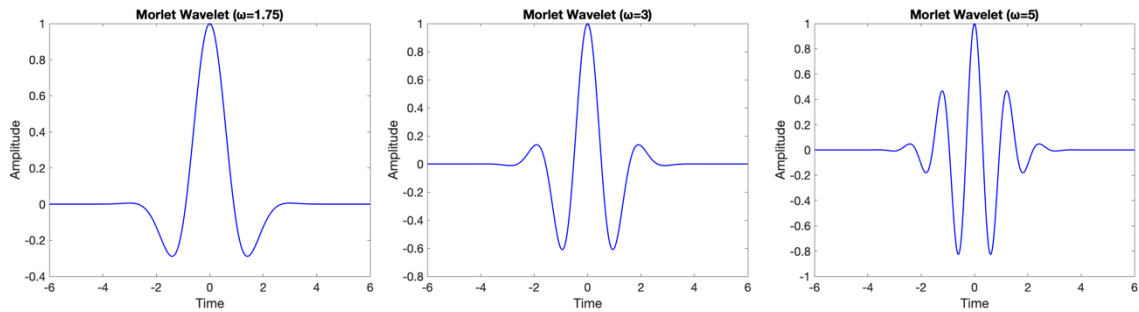


Figure 23. Morlet wavelet function for different ω values.

4.3 Reconstruction Results of Given Wavelet Kernels

To compare the results of the different kernels, a simulated brain phantom is used, and SNR is used as a comparison tool. Since the ground truth is available for the phantom study, SNR is a reliable indication of the reconstruction accuracy, and it is calculated as

$$\text{SNR} = 10\log\left(\frac{\mathbf{x}^2}{(\mathbf{x} - \mathbf{x}_0)^2}\right) \quad (42)$$

where \mathbf{x} is the reconstructed image and \mathbf{x}_0 is the ground truth. The reconstructed images are also included for visual comparison along with SNR. For the simulation study, dynamic PET scans were simulated similar to Wang et al.'s paper [9] using a Zubal head phantom as shown in Figure 24(a). The simulated brain dataset contains dynamic 2D images of the brain, thus global kNN is used without Gaussian weighting. The scanning time consisted of 24 time frames: 4×20 s, 4×40 s, 4×60 s, 4×180 s and 8×300 s.

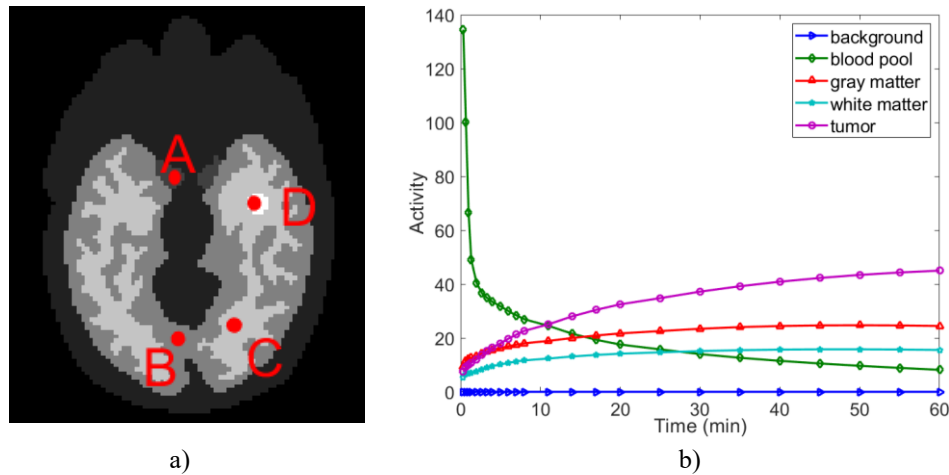


Figure 24. a) Digital phantom with A, B, C, and D being regions in the blood pool, gray matter, white matter and tumor region, respectively. b) Time activity curve for different regions.

Regional time activity curves, shown in Figure 24(b), were assigned to different brain regions. With these regional time activity curves and knowing the duration of each frame, simulated dynamic activity images are generated. For this goal, the value of the time

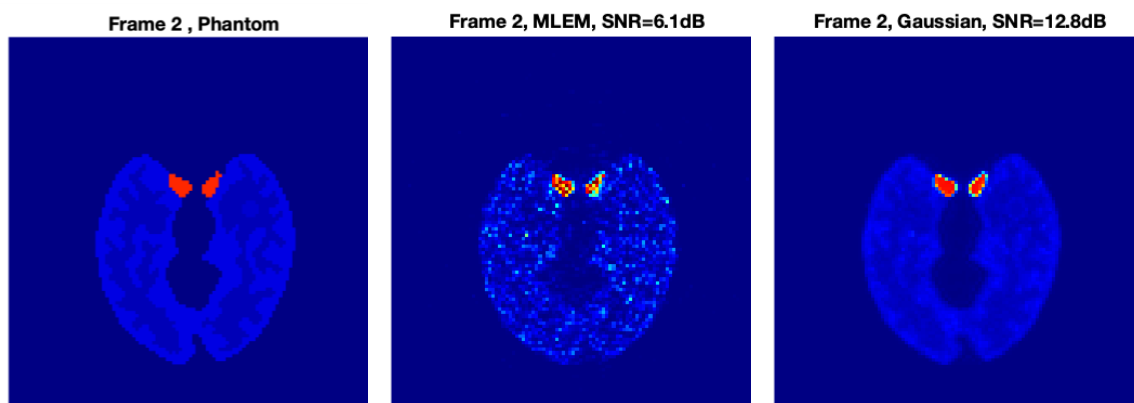
activity curve for each tissue region in each time frame is multiplied by the duration of the frame (in minutes) and that will form the value of that tissue region in the specific time frame. By doing it for all tissue regions and over all time frames, the dynamic activity images are formed. Then dynamic activity images are forward projected with a system matrix, and this will form the noise-free sinograms. By adding scatter and random event noise, realistic PET sinograms were generated. The expected total number of coincidence events over 60 min was 16 million.

As previously explained in Section 3.2, these frames are split into three 20 min length composite frames by summing the frames in 20-minute consecutive intervals: the first composite frame consists of first 16 time frames and largely corresponds to the tracer in the blood, the second composite frame consists of the next 4 time frames and largely refers to the transition of the tracer from blood to tissue, and the final composite frame consists of the last 4 time frames and largely contains the uptake in the target organs and tissues. For this simulation study, a global k NN with 48 nearest neighbors was used for all kernels. For kernel cases where σ (a for Morlet wavelet) needs to be set, a few different σ values are tested, and it is set to the value which gives the best result in terms of SNR and visual quality. For the Ricker wavelet, decreasing σ will increase SNR in early frames slightly but it decreases SNR in later frames. Then if σ is increased to values larger than 1, the SNR in early frames is reduced. The same happens with the Gaussian kernel. For the Morlet wavelet, $a < 1$ gives lower SNR and visual quality in early and late frames and higher values for a reduces SNR in early frames. Overall, for Gaussian and Ricker wavelet, $\sigma = 1$ and for Morlet wavelet $a = 1$ was chosen for this comparison. The simulated data is

reconstructed using maximum likelihood expectation maximization (MLEM) as a reference and also with other mentioned kernels for two of the frames.

The reconstructed images for frame 2 (20 – 40 s) are shown in Figure 25 and for frame 24 (3300 – 3600 s) they are shown in Figure 26. The tumor has higher uptake in frame 24 and is therefore more clearly visible in frame 24. In frame 2, SNR is higher for Ricker wavelet compared to Gaussian kernel. In frame 24, SNR is higher with Gaussian kernel compared to Ricker wavelet and the reconstructed image with the Ricker wavelet presents tumor with higher noise while the Gaussian kernel recovers the tumor more smoothly. For Meyer wavelet, the SNR is lower than Gaussian kernel for frame 2 as there is more noise in gray matter for this kernel compared to the Gaussian kernel. SNR is similar to Gaussian kernel for frame 24, but the tumor is reconstructed with a slightly lower concentration therefore it does not offer any benefit on top of Gaussian kernel.

For biorthogonal wavelets, in frame 2 the SNR values are higher than Gaussian kernel and the visual quality are very similar. For frame 24 both biorthogonal wavelets have lower SNR value and lower concentration value in tumor region and therefore they are also not good substitutes for Gaussian kernel.



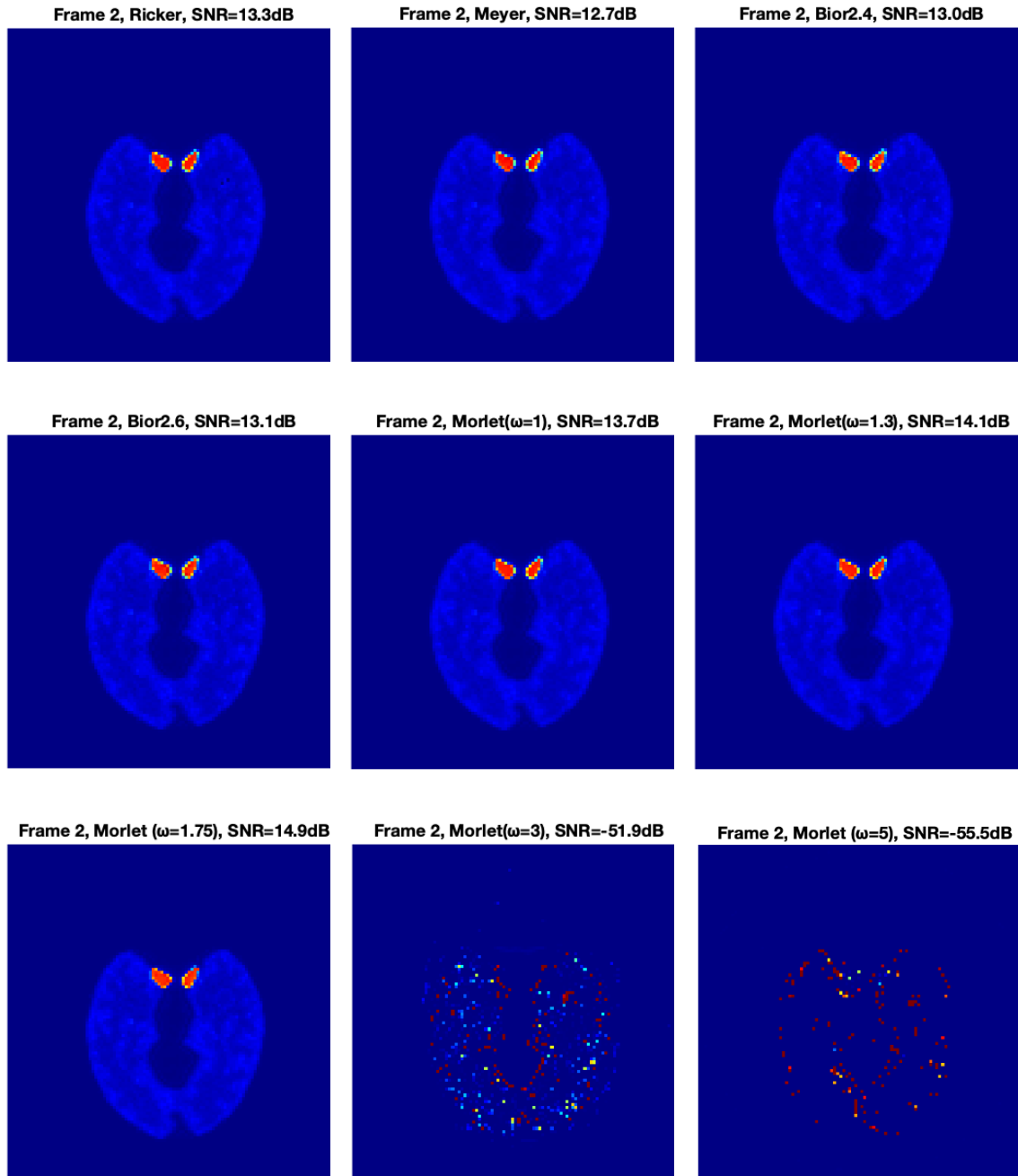
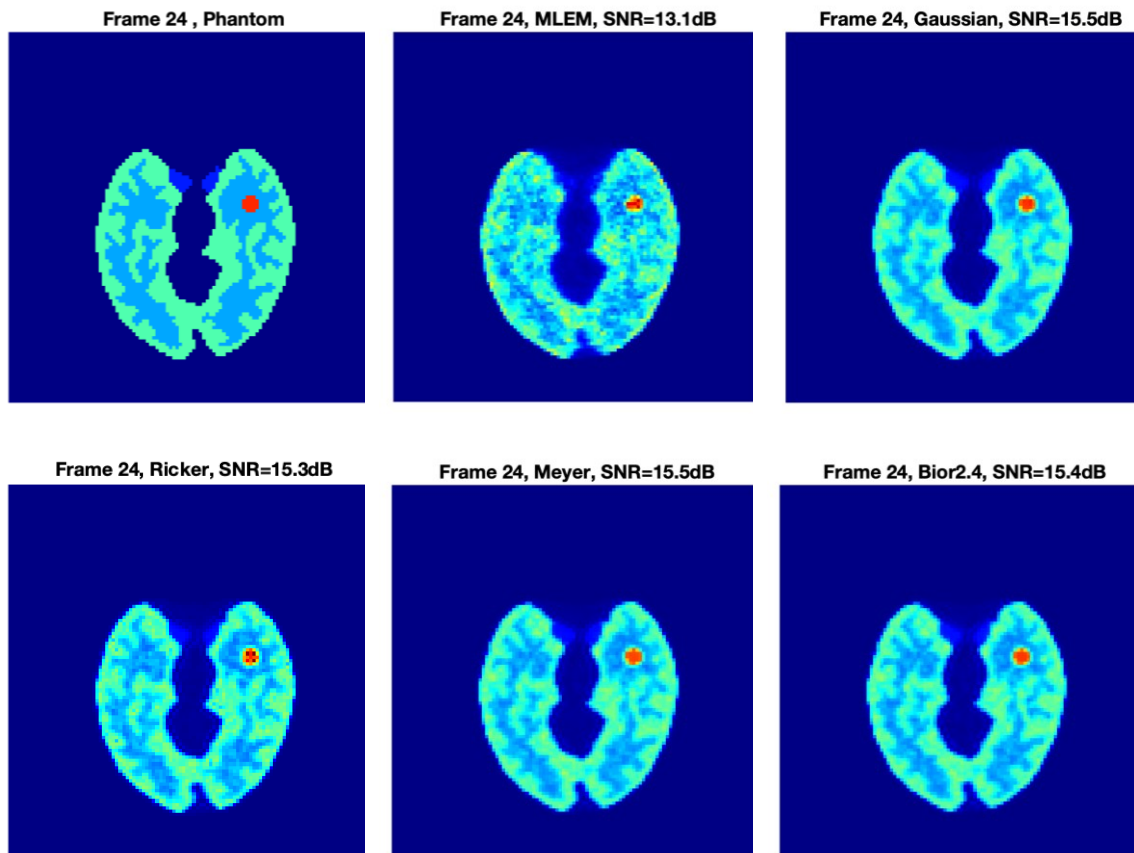


Figure 25. Reconstructed images of frame 2 from different reconstruction methods along with the original phantom.

For the Morlet wavelet kernel, the reconstruction results with the different ω values are shown for frame 2 and frame 24. For ω values larger than 2 the reconstruction quality degrades substantially for frame 24 and it fails for frame 2 (frame with low number of

counts). As explained in section 4.2, for standard ω values (larger than 2) the wavelet will not be able to detect features due to the smear of information over more oscillations [69]. But for smaller values of ω (smaller than 2) the reconstruction does not fail and in fact it improves the quality both in terms of SNR and visual quality compared to other given wavelets for both frames. It can be seen from Figure 25 and Figure 26 that among the chosen ω values, Morlet wavelet with $\omega = 1.75$ works best in the visual quality of the reconstructed image (especially in tumor and blood pool region) and SNR value.

For easier comparison, SNR values for frame 2 and frame 24 comparing different kernels in the kernel reconstruction are shown in Table 2.



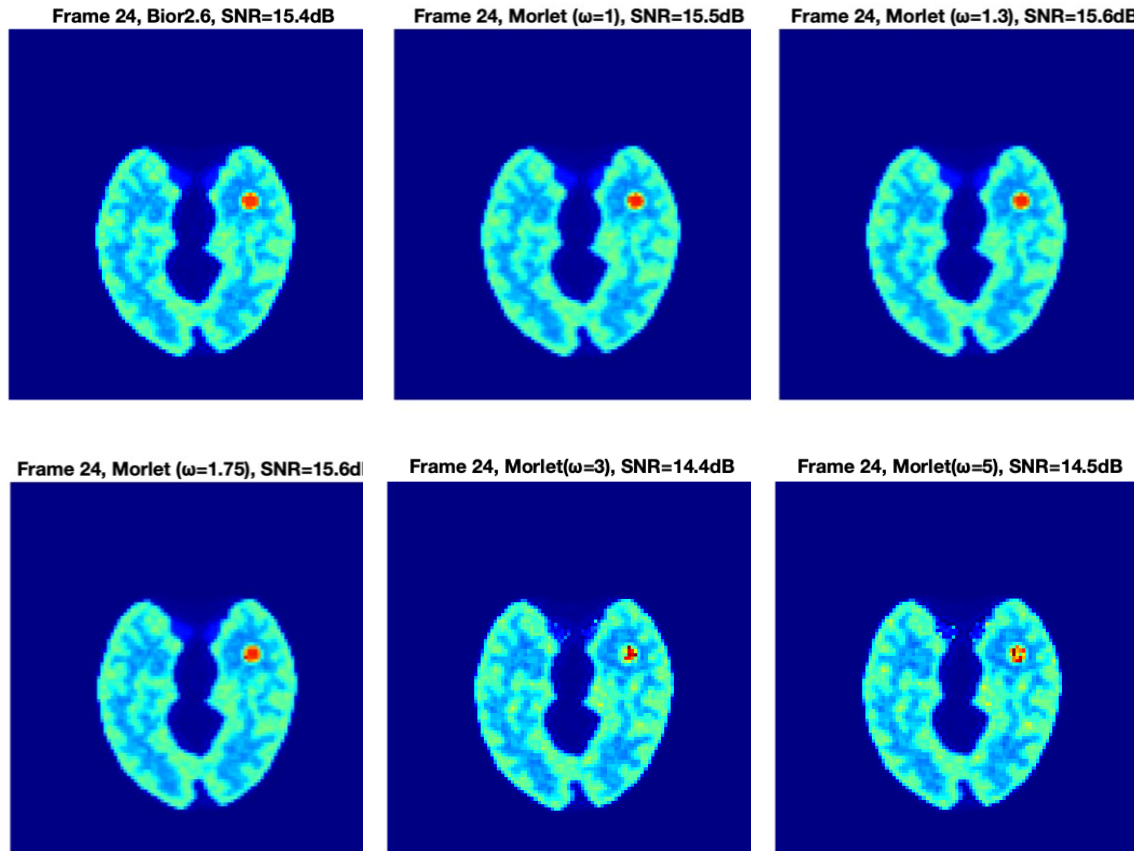


Figure 26. Reconstructed images of frame 24 from different reconstruction methods along with the original phantom.

Table 2. SNR values for frame 2 and frame 24 comparing different kernels for kernel reconstruction.

	Frame 2	Frame 24
MLEM	6.1 dB	13.1 dB
Gaussian	12.8 dB	15.5 dB
Ricker	13.3 dB	15.3 dB
Meyer	12.7 dB	15.5 dB
Bior 2.4	13.0 dB	15.4 dB
Bior 2.6	13.1 dB	15.4 dB
Morlet ($\omega = 1$)	13.7 dB	15.5 dB
Morlet ($\omega = 1.3$)	14.1 dB	15.6 dB
Morlet ($\omega = 1.75$)	14.9 dB	15.6 dB
Morlet ($\omega = 3$)	-51.9 dB	14.4 dB
Morlet ($\omega = 5$)	-55.5 dB	14.5 dB

4.4 Summary

Wavelet kernels are expected to preserve edge information and small details in the image. Therefore, in this chapter, wavelet kernels were chosen as a substitute for Gaussian kernel and some of the well-known wavelets were tested for this goal. Based on the discussions and results given in this section, for this thesis, Morlet wavelets with low oscillations ($\omega = 1.75$) is selected as the wavelet kernel for PET image reconstruction. The reconstruction results with different prior information and different data sets for this wavelet are presented and discussed in the following chapters.

Chapter 5 : Kernel Based Image Reconstruction using Morlet Wavelet Filter

This chapter has been previously published in a Journal. © 2021 IEEE. Reprinted, with permission, from Zahra Ashouri, Guobao Wang, Richard M. Dansereau, Robert A. deKemp “Evaluation of Wavelet Kernel-based PET Image Reconstruction,” 2021 IEEE Transactions on Radiation and Plasma Medical Sciences, August 2021. Some text change and reformatting modifications have been made.

Since the Gaussian kernel tends to over smooth the details in the reconstructed images [9], in the previous chapter, some wavelet kernels were tested to check their effectiveness in terms of reducing the noise while keeping the details in the reconstructed images. A Morlet wavelet with $\omega = 1.75$ was shown to be useful in this regard. In this chapter, I extensively evaluate the Morlet wavelet kernel with three different data sets. The data sets are a simulated brain data, physical NEMA phantom data and patient data. Reconstruction results are presented, and different quality assessment metrics are used to compare the wavelet kernel method with the Gaussian kernel method.

5.1 Details of the Proposed Morlet Wavelet Kernel

As explained in Chapter 4, although the Gaussian kernel increases SNR in reconstructed images [9], it tends to over smooth small targets and tissue boundaries. To address this problem, Morlet wavelet kernel is proposed that does not have the same smoothing effect of the Gaussian kernel.

Principal component analysis (PCA) can be used to map the data into a new feature space that contains more linearly separable features than those in the original input space. The transformation from an original input space into a transform feature space in which the data is projected onto linear components can be done using kernels. This mapping is referred to as kernel PCA (KPCA) [62].

Wavelet kernel PCA can be used to better capture data similarity measures in the kernel matrix [62]. Wavelet kernels are constructed from a given mother wavelet function to improve the performance of kernel PCA as the feature extraction method. As discussed in Chapter 4, many options exist for the mother wavelet which satisfies the admissibility condition. Because of their flexibility, wavelet kernels have been successfully used in support vector machine (SVM) learning for classifying data [62]. Besides classification, wavelet kernels can be used in the process of feature extraction [62]. The wavelet kernel comes from wavelet theory [63] and can approximate arbitrary functions. A translation-invariant version of this kernel is given as

$$g(v, w) = \prod_{i=1}^Q h\left(\frac{v_i - w_i}{a}\right) \quad (43)$$

where $v, w \in \mathbb{R}^Q$, a is the dilation coefficient, and $h(\cdot)$ is the mother wavelet. Equation (43) is general case of equation (41). The single-scale translation invariant (STI) wavelet kernel based on the Morlet mother wavelet function given in [63] as

$$h(z) = \cos(1.75z) \exp\left(-\frac{z^2}{2}\right). \quad (44)$$

is used here. This is a specific form of the Morlet wavelet given in equation (40) with $\omega = 1.75$. In the rest of the chapter, this Morlet wavelet is referred to as WKEM.

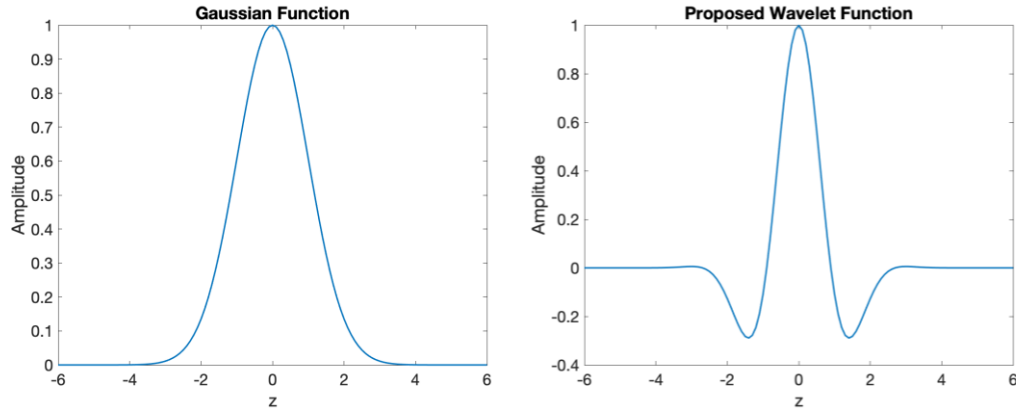


Figure 27. 1-D Gaussian function vs proposed Morlet wavelet.

The one-dimensional form of the Gaussian function and the proposed wavelet function are shown in Figure 27. Due to the sharpness of the transitions in the wavelet function around the peak, the proposed wavelet kernel should be better able to preserve edge information and show higher contrast between the edges and their surrounding compared to the Gaussian function. In this work, v_i and w_i are substituted by features \mathbf{f}_j^i and \mathbf{f}_l^i where i refers to i -th composite frame. The (j, l) th element of the wavelet kernel matrix \mathbf{K} is given in equation (41) with $\omega = 1.75$ and Q is the total number of composite frames. Each composite frame is a dimension of the wavelet feature space. \mathbf{f}_j^i and \mathbf{f}_l^i are the feature vectors or pixel values in the i -th reconstructed composite frames. This wavelet kernel-based image reconstruction is referred to as WKEM in this chapter.

5.2 Simulation Study

5.2.1 Simulation Setup

For the simulation study, the same data set as in Section 4.3 was used. The Zubal head phantom and the time activity curves are shown in Figure 24. As explained in Section 4.3, the scanning time consisted of 24 time frames: 4×20 s, 4×40 s, 4×60 s, 4×180 s and 8×300 s. The sinograms for the simulated brain dataset is derived the

same as the method defined in Section 4.3. The expected total number of coincidence events over 60 min was 16 million. For this study to have robust results, ten realizations were generated with the same scatter and noise level.

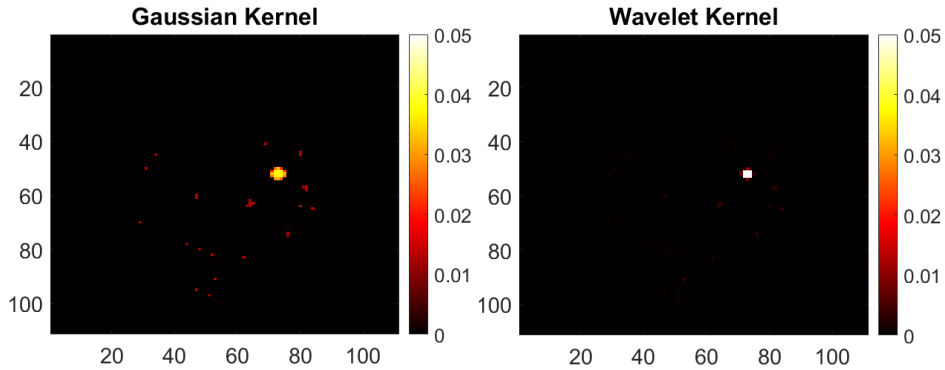


Figure 28. Basis image of the two kernel matrices that corresponds to a pixel in the tumor region of the simulated brain.

Figure 28 shows the basis image of the Gaussian and wavelet kernel matrices for a pixel in the tumor region of the simulated brain data. In this figure, the chosen pixels in the wavelet kernel are more localized, meaning that the wavelet kernel identifies pixels corresponding to the same tissue and uses them for kernel construction of that specific pixel while the Gaussian kernel also includes pixels from outside the tissue region in the kernel construction. Therefore, the wavelet kernel should be better able to identify similar pixels, and as a result it can preserve edge properties better.

5.2.2 Implementation Parameters

As explained in Section 4.3, the number of composite frames is three, each corresponding to 20 minutes of the scan time. For the simulation study, a k NN with 48 nearest neighbors was used for both Gaussian kernel and wavelet kernel. As explained in Section 4.3, for a values smaller than 1 the wavelet was too thin, and the reconstruction quality degrades. For values larger than 1, the mean squared error (MSE) increased for

most of the frames with the increase in a value, especially in early frames in which the WKEM showed greater improvement. Therefore a was chosen to be equal to 1 for the wavelet kernel. For the Gaussian kernel, MSE is lower with σ smaller than 1 in early frames but it has higher MSE in later frames and for σ values larger than 1 it is opposite, therefore $\sigma = 1$ was chosen for Gaussian kernel to have acceptable result in both early and later frames. MSE versus σ (or a for wavelet) are shown in Figure 29 for an early frame and a late frame (Frames 2 and 24).

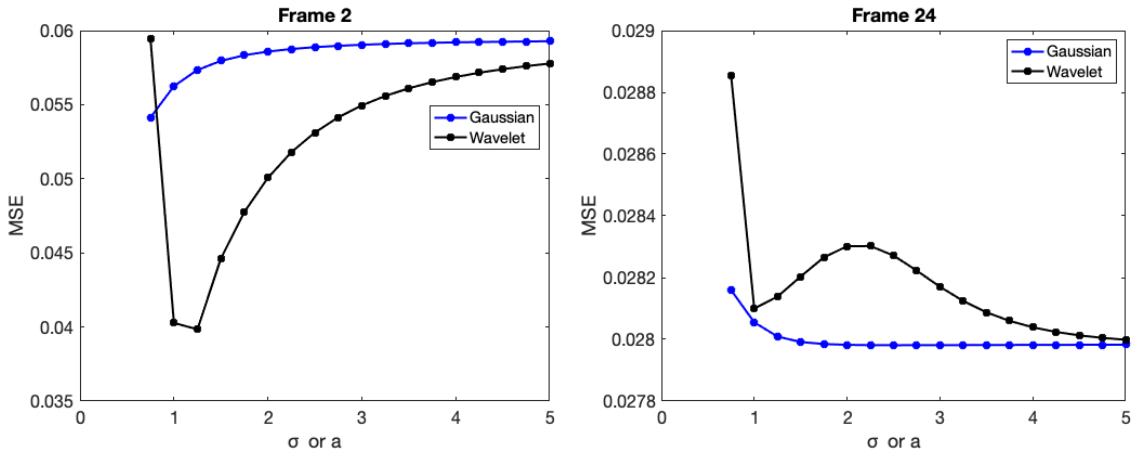


Figure 29. MSE for different " σ " (" a " for wavelet) value shown for frame 2 and frame 24.

5.2.3 Evaluation Method

For each data set, the evaluation method is defined based on the information available. For the simulation study, the ground truth is available and, therefore, SNR and contrast recovery coefficient are defined accordingly and based on using different realizations. For quantitative comparison between different reconstruction methods, contrast recovery coefficient (CRC) of the blood pool and tumor are also calculated by simulating ten noisy realizations and reconstructing them independently. The CRC is calculated by

$$\text{CRC} = \frac{\frac{1}{10} \sum_{i=1}^{10} \left(\frac{\mathbf{R}_i - \mathbf{B}_i}{\mathbf{B}_i} \right)}{\left(\frac{\mathbf{R}_{\text{true}} - \mathbf{B}_{\text{true}}}{\mathbf{B}_{\text{true}}} \right)} \quad (45)$$

where \mathbf{R} refers to region of interest, \mathbf{B} is the background region and i is the i -th realization of the simulated data. The subscript "true" refers to the value of the region in the ground truth. The white matter was the background region. Background standard deviation was derived pixel-wise over 10 realizations and was then averaged over all the pixels in the background region and normalized by the true background value.

5.2.4 Results

Figure 30 shows images of the reconstructed brain phantom for two sample time frames using 40 iterations. The WKEM method achieved a higher SNR than KEM for the early Frame 2 in which the blood pool has a high activity. For the late frame, Frame 24, the two approaches had the same SNR. Nonetheless, the shape of the tumor using WKEM is more consistent with the ground truth. In Figure 31, CRC versus background standard deviation (SD) percentage is shown for the blood pool and the tumor region by varying the iteration number from 20 to 60 with 20 iterations having the smallest CRC value and 60 iterations having the largest CRC value in each method. WKEM had a higher CRC than KEM while with a similar background SD. The improvement for the blood pool is higher than for the tumor. This result is also seen in Figure 30 where SNR and the visual quality of the reconstructed images are higher with WKEM for the low count frames (shorter time frames with low activity), and for the higher count frames (later frames which are longer time frames with higher activity), WKEM is acting similar to KEM.

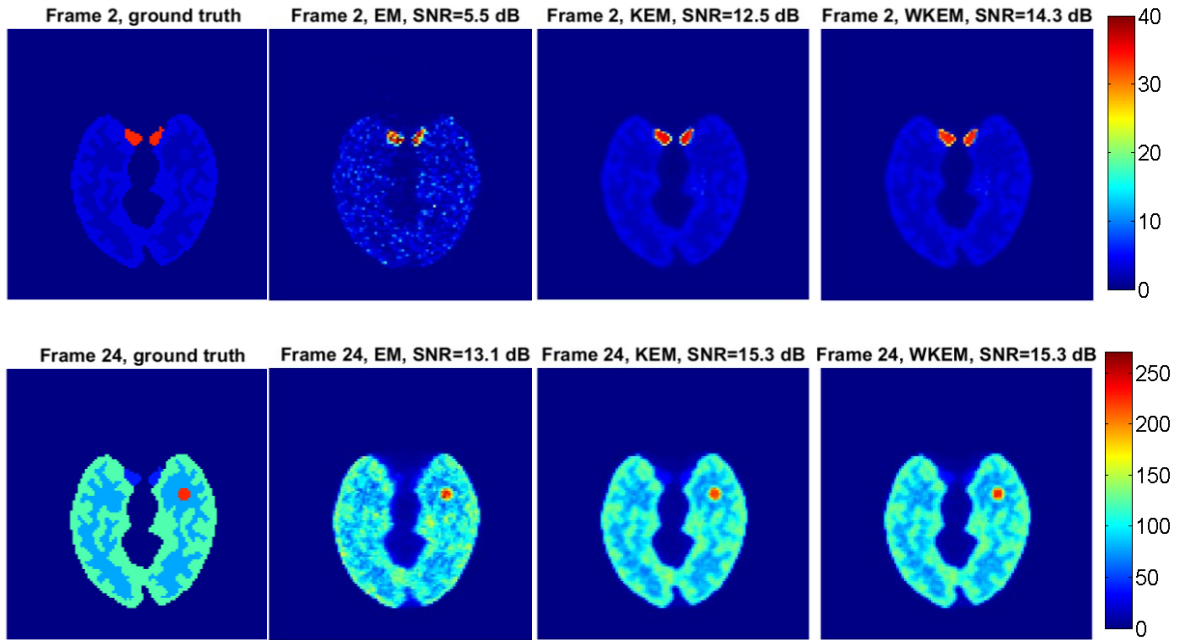


Figure 30. Ground truth and reconstructed images of three different reconstruction methods for two different time frames of the brain phantom.

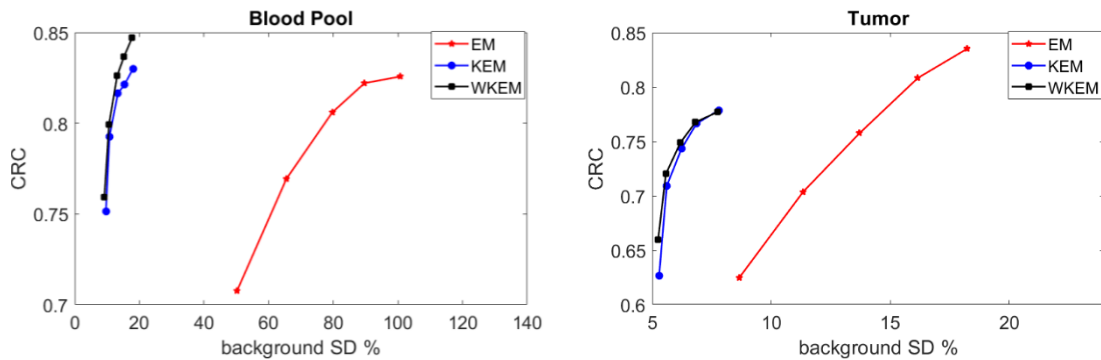


Figure 31. Contrast recovery versus background standard deviation for Zubal head phantom. Blood pool is calculated in frame 2 and the tumor is calculated in frame 24

MSE with error bar for all three reconstruction methods are shown in Figure 32. In this figure, the iteration number is set to 40 and the error bars show the variability between the ten realizations. The variability is the standard deviation of the MSE over ten realizations. This figure shows that WKEM has a smaller MSE than KEM for earlier

frames, which is consistent with the SNR trends from Figure 30. For later frames, KEM and WKEM have similar performance in terms of MSE.

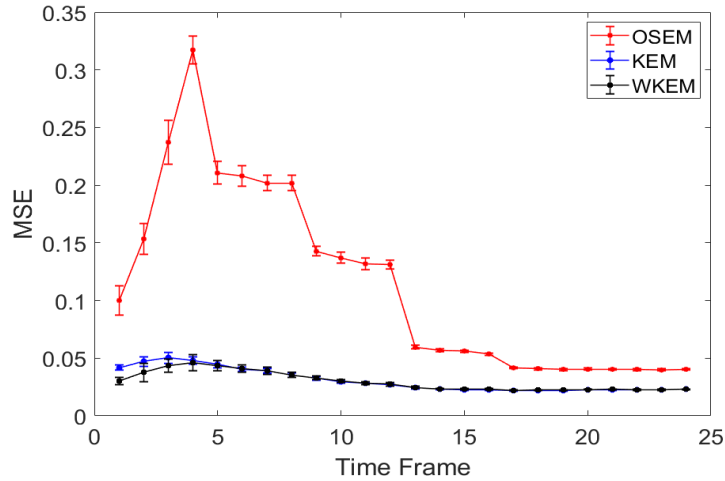


Figure 32. Mean square error (MSE) for different reconstruction methods shown for each frame with the standard deviation error bars for ten realizations.

5.3 Real Data

A physical phantom study and real patient study were conducted to further evaluate the WKEM reconstruction method. As explained in Section 3.3, for the implementation of the kernel method in each study, a cubic window was chosen as the neighborhood and different sizes of the neighborhood window were tested for each study. A window of $7 \times 7 \times 7$ was used for applying regional k NN. Note that using this local neighborhood instead of global k NN decreases the computational complexity such that the method is more practical for 3D reconstruction [9]. To include the spatial distance between the pixel of interest and neighboring pixels in the cubic neighborhood, Gaussian weights are calculated in a similar way as explained in Section 3.3. The weights are then multiplied by the kernel coefficients from equations (18) and (41). To apply a regional k NN, in the neighbourhood of each voxel, k nearest neighbours are selected. For both the wavelet kernel and Gaussian kernel, the parameters σ and a were set to 1. As explained in Section

3.3, this spatial weighting was not applied in the simulated 2D brain data since using a global k NN was feasible. For real data, OSEM reconstruction was performed with different iteration numbers and numbers of subsets as explained in the following subsections.

5.3.1 NEMA Phantom

To evaluate the performance of reconstruction, National Electrical Manufacturers Association (NEMA) standard phantom was used [70]. A dynamic study was performed using this phantom and the resulting sinograms are reconstructed with OSEM, KEM and WKEM reconstruction methods. The NEMA phantom consists of six spheres with varying diameters which are filled with radiotracer. For the measurements, each sphere is filled with 1.5 MBq of F-18 diluted in about 55 mL of water. The background is injected with 80 MBq of F-18 diluted in about 10 L of water. The dynamic frames follow an exponential determined by F-18 decay. The scan time is 15 min and consists of 26 time frames as follows: 15×10 s, 5×30 s, 5×60 s and 1×300 s.

Composite frames were chosen so that each corresponds to 5 min of the scan time: the first composite frame is from the first 20-time frames, the second composite frame contains the next 5 time frames, and the final composite frame corresponds to the last time frame. For the NEMA phantom, ground truth is known. Therefore, for comparison I looked into the contrast and noise calculations in each of the spheres [71]. For this goal, a region of interest (ROI) the same size of the sphere is drawn manually for each sphere with the help of the corresponding CT image and the mean value in these spheres is the average

number of counts. For comparison, contrast recovery is calculated for each reconstruction method using

$$CR_j = \frac{\frac{C_{S,j} - C_{B,j}}{C_{B,j}}}{\frac{a_S - a_B}{a_B}} \times 100 [\%]. \quad (46)$$

where $C_{S,j}$ is the average counts in the ROI for sphere j and $C_{B,j}$ is the average counts in the background ROI for sphere j . The background ROIs are drawn inside the phantom away from the spheres and are concentric to each other with diameter equal to the referring

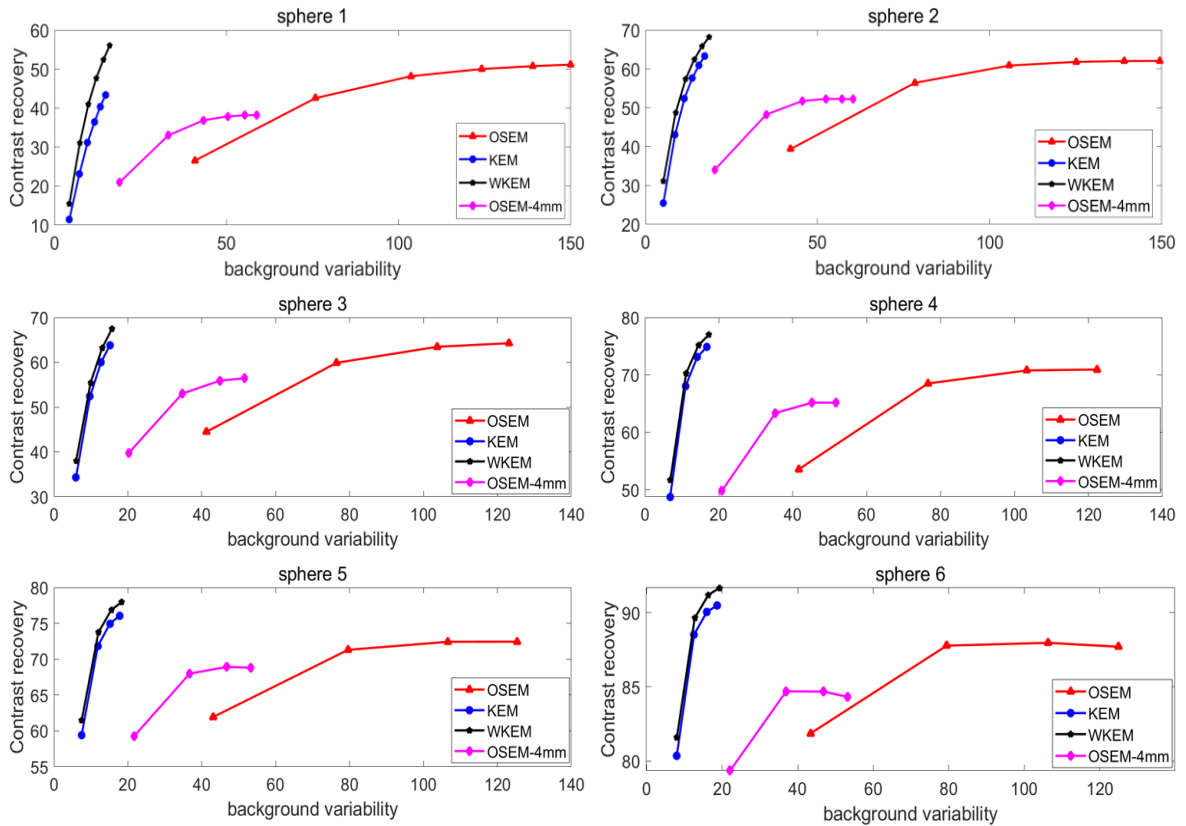


Figure 33. Contrast recovery versus background variability for all sphere sizes, with sphere 1 being the smallest sphere and sphere 6 being the largest sphere.

sphere. a_S and a_B are the activity concentration in the hot spheres and background, respectively. The percentage of background variability N_j is a measurement of image noise for sphere j with standard deviation SD_j (in an ideal case = 0 %) and is calculated using

$$N_j = \frac{SD_j}{C_{B,j}} \times 100 [\%]. \quad (47)$$

SD_j is the standard deviation in the background ROI for sphere j .

Figure 33 shows contrast recovery versus background variability for different sphere sizes by increasing the iteration number. Contrast recovery and background variability are averaged over the time frames. In this study, there are 24 subsets in the reconstruction and number of iterations vary from 1 to 4 (for smaller spheres the iteration number is increased to 6 to have convergence for CRC) with 1 iteration having the smallest background variability value and 4 (6 for sphere 1 and 2) iterations having the largest background variability value in each method. As can be seen from Figure 33, both KEM and WKEM have significantly smaller background variability in comparison to OSEM. However, WKEM has the best performance in terms of contrast recovery and background variability trade off, especially for smaller spheres. In the smallest sphere (sphere 1), OSEM achieves a much higher contrast recovery value in comparison to WKEM, which is expected as KEM and WKEM have smoothing included in the reconstruction process. But, since the background variability is larger for OSEM, overall, it is not as effective as WKEM. Also, OSEM is clinically always followed by post filtering to reduce noise and as the figure suggests, OSEM with 4 mm post filtering reduced contrast recovery to a level lower than WKEM.

Figure 33 also demonstrates that for the smallest sphere with the highest iteration number, there is an increase of around 20% in the contrast recovery value between KEM and WKEM, which is significant. There is also an increase of around 10% for sphere 2 between KEM and WKEM. For other larger spheres (spheres 3 to 6), the increase in the contrast recovery value is around 1–3%. These results affirm the statement about this

wavelet kernel being better than the Gaussian kernel at retrieving small objects. This result can also be seen in Figure 34, in which a reconstructed frame of the NEMA phantom is shown and the contrast, especially in the smallest sphere, is best preserved in WKEM. We can also see that larger spheres look smoother in KEM compared to WKEM. This is because the Gaussian kernel has a smoothing effect, however results from Figure 33 show that the variability in the background is almost unchanged between KEM and WKEM for larger spheres.

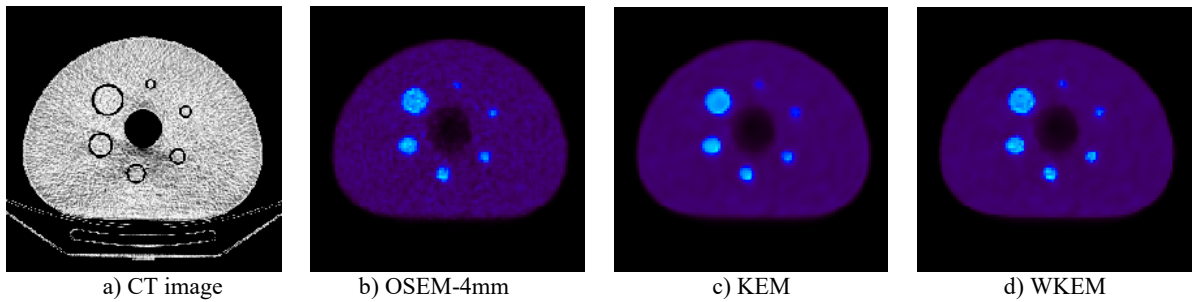


Figure 34. Reconstructed image of a frame from NEMA phantom.

5.3.2 Patient Data

The patient data are from the Ottawa Heart Institute and were acquired as part of a research ethics board approved study presented in Appendix D. All images were anonymized before analysis. For patient data, there is no ground truth available and, therefore, SNR and contrast are defined based on tissue regions in the same way as the method in Section 3.4 from equations (26) and (27).

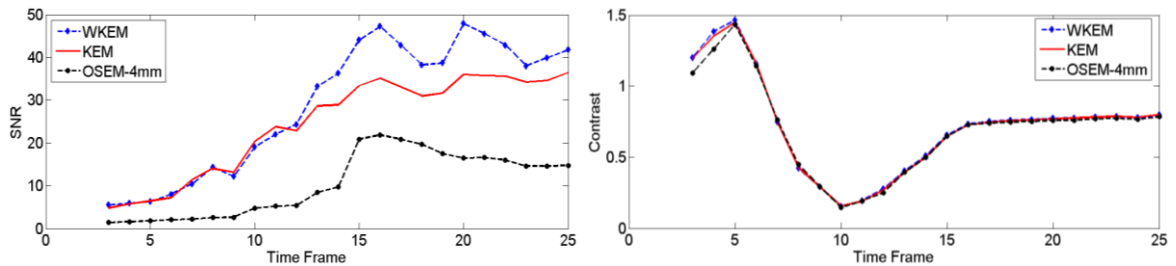


Figure 35. Average SNR and contrast over all frames for OSEM (with 4 mm post filtering), KEM, and WKEM.

The study includes dynamic PET scans acquired from 10 patients with HED tracer on a GE D600 PET/CT scanner. The scan time was 60 minutes split into 25 time frames defined as follows: 9×10 s, 3×30 s, 2×60 s, and 11×300 s. Three composite frames were created, each corresponding to 20 minutes of scan time, therefore the first composite frame was from the first 17 frames, the second composite frame was derived from the next 4

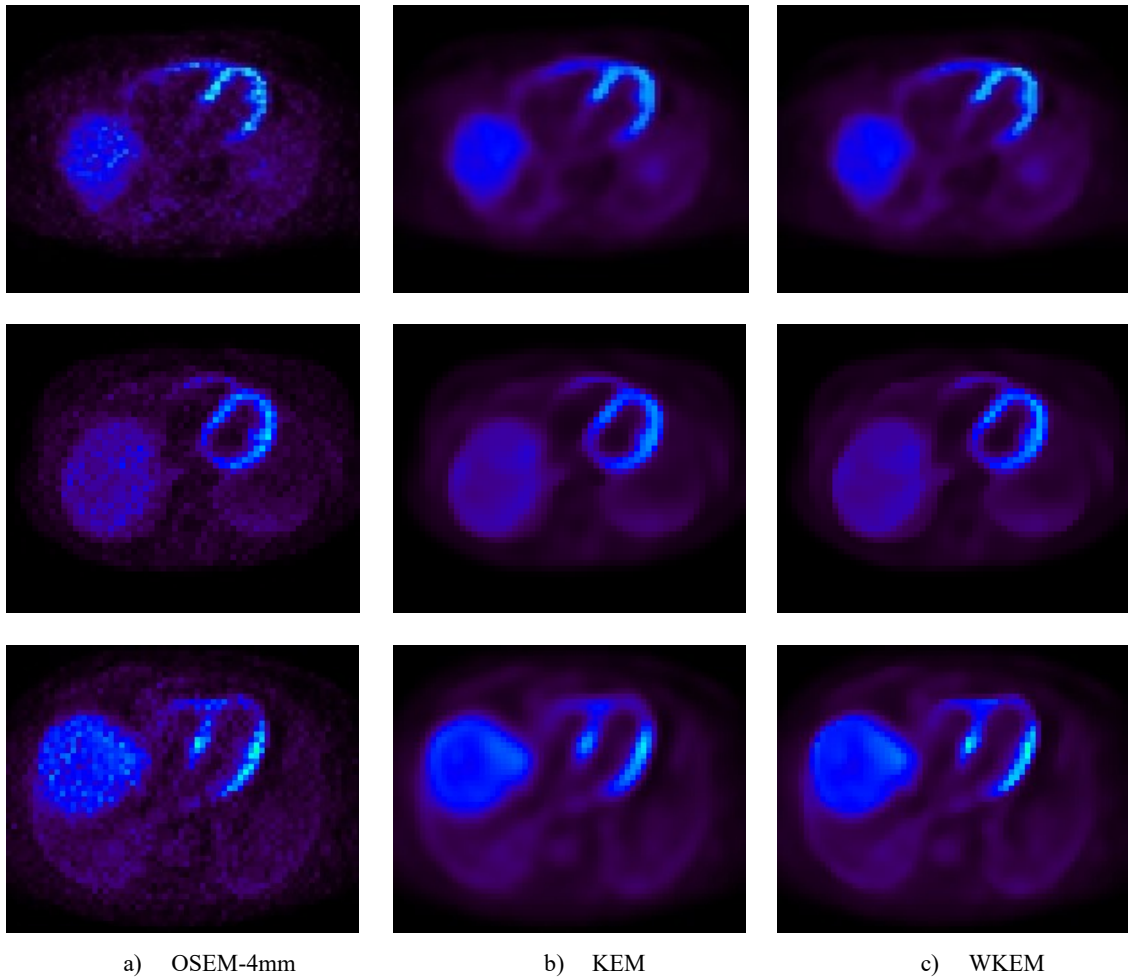


Figure 36. A transaxial slice of the heart for OSEM, KEM, and WKEM. Each row corresponds to one of the patients and shows the last frame

frames and the last one is from the last 4 frames of the dynamic series. For patient data, OSEM reconstruction was performed with 32 subsets and 3 iterations. The Gaussian kernel parameter σ is set to 1 and for WKEM, a is 1 as discussed.

Figure 35 shows the average SNR and contrast over all 10 patients for different time frames and different reconstruction methods. In the first couple of frames of the dynamic series, the amount of tracer uptake is very small and there is a very low number of photons. This will cause the mean value and standard deviation to be very close to zero in these time frames therefore, the resulting SNR and contrast value would be inconsistent with the rest of the frames. Because of this reason they have been removed from this study and are not shown in the SNR and contrast calculations. The contrast is the normalized difference of the regions in the LV and blood cavity. In early frames, the tracer is mainly in the blood, so the difference is large. Then at some point in time, the tracer is in both the blood and LV and, therefore, their difference is small. Then later, the tracer is taken up in the LV and again the difference between these two regions is large.

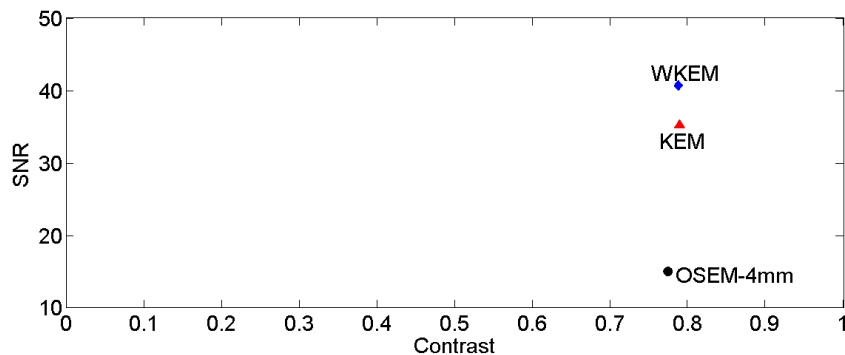


Figure 37. SNR vs contrast of uptake frames (last four frames) averaged over all patients for OSEM (with 4 mm post filtering), KEM, and WKEM.

Figure 36 shows a transaxial slice of the heart for three patients. As explained in Section 5.1, a wavelet kernel should be better able to preserve edge information. Figure 36 affirms this statement by showing that WKEM preserves high intensity values better than KEM, especially in the left ventricle wall. In Figure 37, SNR versus contrast is shown for WKEM and is compared to KEM and OSEM (with 4 mm post filtering). For this figure,

the uptake frames, which are the last four frames, are included and the mean value of contrast and SNR over the last four frames of all patients are calculated. From Figure 37, WKEM presents a higher SNR value compared to KEM and OSEM with post filtering and it also preserves contrast.

5.4 Summary

A wavelet kernel with Morlet wavelets with $\omega = 1.75$ has been evaluated for dynamic PET series. The method has been tested on simulated data, physical phantom data (NEMA Phantom) and real patient data and compared to KEM. Results for simulated data show that WKEM method achieved a higher SNR and contrast recovery than KEM for the low count frames. The NEMA phantom study suggests WKEM can reconstruct the phantom with higher contrast recovery, especially for smaller spheres. Also, the study using cardiac patient data shows improvement of the SNR in WKEM method over KEM and the visual quality of images for patient data indicate WKEM is better in preserving edge information in left ventricle wall than KEM method.

Chapter 6 : Gaussian Kernel Based Image

Reconstruction using MR Information

Part of this chapter has been previously published in a conference proceeding. © 2020 IEEE. Reprinted, with permission, from Zahra Ashouri, Chad R. Hunter, Benjamin A. Spencer, Guobao Wang, Richard M. Dansereau, Robert A. deKemp “Kernel-based Reconstruction of Cardiac PET Images Using MR Information,” 2020 IEEE Nuclear Science Symposium and Medical Imaging Conference (NSS/MIC), November 2020. Some reformatting modifications have been made.

Anatomical image modalities have high spatial resolution and therefore most of the PET imaging systems have either CT (computed tomography) or MRI (magnetic resonance imaging) technologies incorporated in their system. PET/CT has been widely used in clinics, especially for attenuation correction in PET, but PET/MR systems have also been used due to their ability to acquire simultaneous images in PET and MRI. MR imaging is a non-invasive imaging method while CT exposes the patient to radiation [72]. Therefore, incorporating MR information in PET image reconstruction reduces the health risks related to radiation exposure. But mismatches between MR imaging and the PET image can degrade the quality of the PET reconstruction and should be considered. Some methods include the anatomical information with some penalty function [5], [38]–[45]. But incorporating anatomical prior information with the kernel method is simpler than incorporating this information as a penalty term. This is because with the kernel method there is no need to do segmentation and prior information can easily be incorporated in ordered subsets reconstruction [30].

Some previous works with the kernel derived from MR image have been explained in Section 2.9. In [8], Hutchcroft et al. derived the Gaussian kernel directly from the co-registered MR image and embedded it in the iterative update of the image. In this chapter, a kernel is defined in a similar way as described by Hutchcroft et al. [8]. However, in their work, they present the results based on tumor detection in the brain and compared it to reconstruction methods using MR in the form of a regularizer. Here the focus is on the difference between this method and the standard kernel method using dynamic series as prior information [9]. In the next chapter this will be extended by using wavelet kernels.

6.1 Method

In the original KEM method for dynamic PET [9], multiple time frames are summed to form composite frames. The pixel values in the composite frames are the feature vector [9]. In this chapter, the feature vectors are assigned as the pixel values from a co-registered MR image. The kernel matrix \mathbf{K} is formed by using the radial Gaussian function to calculate the similarity between pixel intensities of the co-registered MR image in a defined neighborhood. This kernel is then used in the EM update in equation (21). With this method of creating the feature vector, no dynamic imaging is required; therefore, it can be used for clinical cases where dynamic PET imaging is not feasible because of patient throughput. Using MR information for PET image reconstruction has also an undesired effect of including features particular to MR in PET image reconstruction due to mismatch and therefore introducing bias in PET image reconstruction [58]. This study was produced without the use of a commercial PET-MR scanner, therefore PET and MRI are not acquired simultaneously and as a consequence registration is required. Registration was performed

using the Elastix software [2]. The registration alignment was confirmed visually as well to make sure there are no gross errors in the registration.

6.2 Patient Study

The study population for this work includes dynamic PET scans acquired from three patients with the HED tracer from the same study with the research ethics board approval in Appendix D. The data were anonymized before analysis. The experimental setup for PET imaging is same as the setup explained in Section 3.5. MR images are acquired at a different time with a Siemens Aera, which has magnetic field strength of 1.5 T. This system has magnet length of 137 cm and system length of 145 cm with 70 cm bore size. The acquisition protocol chosen was the steady-state free precession (SSFP) and the image was acquired at end-expiration and end-diastole using respiratory-navigators and ECG-gating. SSFP was chosen since it gives a good contrast between left ventricle wall and blood cavity. MR images were registered to the PET images and then used for PET image reconstruction. The MRI-based kernel reconstruction method (MKEM) is compared with the original KEM reconstruction method [7] and ordered subset expectation maximization (OSEM) reconstruction [30]. The purpose of this study is to evaluate the quality of these reconstruction methods in the left ventricle (LV) wall, which is the target region of interest (ROI). To compare these three reconstruction methods, contrast is calculated using equation (27). For ROI quantification of the left ventricle, SNR is defined locally [8] to reflect changes in the LV and therefore is calculated for this ROI as

$$\text{SNR} = \frac{\text{mean(LV)}}{\text{std(LV)}}. \quad (48)$$

For this SNR calculation, noise is defined as the standard deviation in the LV. This is because the kernel derived from MR information might introduce some artifacts due to

mismatch between the two modalities, therefore the focus here is on a small area in the LV to see if there is improvements.

Table 3. SNR and contrast values for the late uptake frames for all three patients.

		KEM	MKEM	OSEM
Patient #1	SNR	7.33	7.28	5.28
	Contrast	74.81%	75.11%	75.27%
Patient #2	SNR	5.39	5.39	4.49
	Contrast	79.72%	79.81%	79.37%
Patient #3	SNR	6.16	6.09	4.79
	Contrast	82.89%	83.00%	81.24%

A one-tissue compartment model from equation (16) is achieved in FlowQuant for kinetic modeling of the left ventricle (tissue of interest). The SNR and contrast values for all three patients over the last four uptake frames are presented in Table 3. These values are obtained from equations (27) and (48). As presented in the table, these values are very close for MKEM and KEM. Dynamic PET KEM has slightly higher SNR compared to MKEM but on the other hand it has slightly lower contrast.

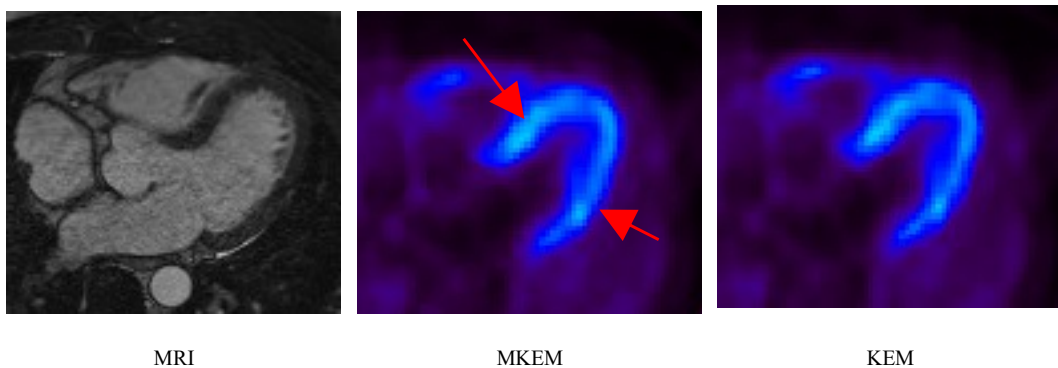


Figure 38. A transaxial slice of the heart from patient #1 for a late frame showing reconstructed image for MKEM and KEM and the corresponding SSFP MR image.

The reconstructed images show some subtle differences between the two methods. Figure 38 shows some improvements for MKEM on the left ventricle wall shown by arrows, which might be because MKEM extracts the kernel from a high-resolution MR image and might be better at preserving high intensity values. This is in agreement with the results from [8] which claims KEM with MR prior information can improve ROI quantification. Dynamic scans need the patients to stay still and inside the PET system for an hour which is not possible for all cases while static PET and MR are very fast and can be done in a few minutes or seconds. Therefore, MKEM can be used to reconstruct uptake images of perfusion when dynamic scans are not available.

The kinetic parameter, K_1 , as explained in Section 2.8, is the uptake constant in a one-tissue compartment model and is determined from kinetic modeling. Polar map images of K_1 for left ventricle in KEM and MKEM along with OSEM reconstruction are given in Figure 39. As explained in Section 3.6 polar maps are derived by projecting the left ventricle wall into a 2D plane using FlowQuant™. These polar maps are then segmented into smaller segments and for each segment, using the input blood function and the time activity curves estimated from the dynamic PET images, the kinetic parameter K_1 is estimated. The mean and standard deviation of the K_1 value in these segments is shown in Figure 39 for all three patients and each reconstruction method. As it can be seen K_1 rate is almost unchanged for all three reconstruction methods, meaning that the rate quantification in this study is not affected by the image reconstruction methods. This is not surprising because the injected dose already provides good image quality, and the kinetic quantification was performed for regions in which a number of voxels are involved.

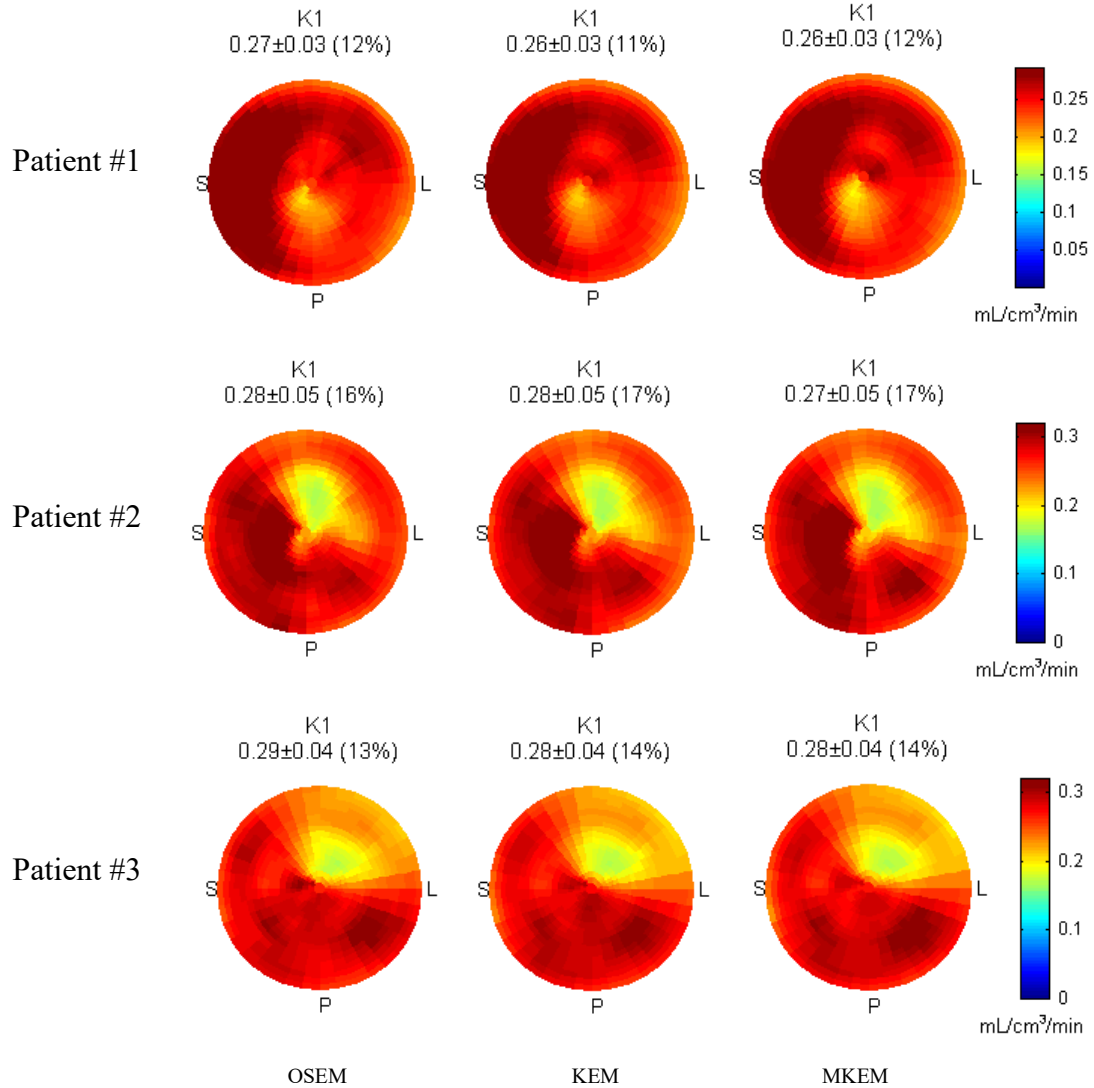


Figure 39. K_1 values for three reconstruction methods and all three patients. Each patient is shown in one row. The mean and standard deviation of K_1 is shown.

6.3 Summary

In this chapter, MKEM is compared to the KEM method that uses composite frames to reconstruct dynamic PET images. Results show that the two kernel-based reconstruction methods work almost equally in these cardiac images. The use of MR images as a feature vector eliminates the need for dynamic image reconstruction of the composite series and could therefore be an option for cases where no dynamic imaging is obtainable and still produce comparable results.

Chapter 7 : Multi-scale Morlet Wavelet Kernel-based PET Reconstruction Using MR Prior Information

Part of this chapter been previously presented in a conference abstract. © 2021 IEEE. Reprinted, with permission, from Zahra Ashouri, Guobao Wang, Richard M. Dansereau, Robert A. deKemp “Multi-scale Wavelet Kernel-based PET Reconstruction Using MR Side Information”, 2021 IEEE Nuclear Science Symposium and Medical Imaging Conference (NSS/MIC), October 2021.

As explained in Chapter 6, Hutchcroft et al. [8] extracted the features from pixel intensities from the co-registered MR image and used the Gaussian kernel to calculate the kernel coefficients. In this chapter, the kernel used is a multi-scale wavelet [62] to help preserve edges that may be over-smoothed by a Gaussian kernel. The multi-scale wavelet kernel is built based on the single-scale wavelet kernel previously introduced Chapter 5. The performance of single-scale wavelet kernel, multi-scale wavelet kernel, Gaussian kernel with MR information [8], and MLEM are compared on a simulated brain image and real patient data.

7.1 Anatomical Prior Kernel Extraction

The feature vectors are built like the method explained in Section 6.1. Here, the feature vector for each pixel is formed by defining a patch around a corresponding pixel (x_j) in the co-registered MR image as illustrated in Figure 40. First each pixel in the PET image is matched to a corresponding pixel in the co-registered MR image (PET and MR

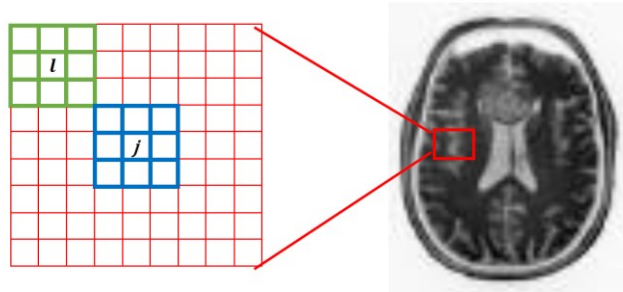


Figure 40. MR image showing feature extraction with patch-wise similarity between voxels. f_j is the feature vector for pixel j and it contains all the pixels in the blue window and f_l is the feature vector for pixel l and consists of all the pixels in the green window.

image are same size in this dataset) and the patch around the corresponding pixel in the MR image forms the feature vector for the pixel of interest in the PET image as

$$\mathbf{f}_j = [x_{j,1}, x_{j,2}, \dots, x_{j,t}, \dots, x_{j,T}]. \quad (49)$$

where $x_{j,t}$ is pixel t in the MR patch and T is the total number of pixels in the MR patch. Basically, T is the size of the feature vector for each pixel when using anatomical prior information, while when using the dynamic PET as prior information, the number of composite frames is the size of the feature vector for each pixel. A kernel matrix \mathbf{K} can be formed using different kernel functions, such as a Gaussian, single-scale or multi-scale wavelet functions which are evaluated in this chapter.

7.2 Single-scale and Multi-scale Wavelet Kernels

As discussed in Section 5.1, KPCA is used to convert the feature space into a transform space. In Chapter 5, a single-scale translation invariant wavelet kernel is introduced for PET image reconstruction. A multi-scale translation invariant (MTI) wavelet kernel with Z scales is given as [62]

$$g_{MS}(v, w) = \sum_{z=1}^Z \frac{1}{a_z} \prod_{i=1}^Q h\left(\frac{v_i - w_i}{a_z}\right) \quad (50)$$

where a_z is the dilation coefficient and $h(\cdot)$ is the mother wavelet. v_i and w_i are substituted by the i -th feature vectors \mathbf{f}_j^i and \mathbf{f}_l^i for pixel j and neighboring pixel l . The STI wavelet kernel is a special case of the MTI wavelet kernel in equation (50) with a fixed a instead of a_z and is given in (43) in Chapter 5.

The STI and MTI wavelets defined with Morlet mother wavelet are both Mercer kernels [62]. Similar to Chapter 5, for the MTI kernel, Morlet wavelet given in (44) is chosen as the mother wavelet. The (j, l) th element of the wavelet kernel matrix \mathbf{K} for MTI would be

$$\mathbf{K}_{j,l} = \sum_{z=1}^Z \frac{1}{a_z} \prod_{i=1}^Q \left[\cos \left(1.75 \left(\frac{(\mathbf{f}_j^i - \mathbf{f}_l^i)}{a_z} \right) \right) e^{\left(-\frac{(\mathbf{f}_j^i - \mathbf{f}_l^i)^2}{2a_z^2} \right)} \right] \quad (51)$$

where Q is the feature vector size. The STI wavelet kernel is given in equation (41).

For both single-scale and multi-scale wavelet kernels, a window centered on a pixel of interest defines where the neighboring pixels are located. The neighborhood window determines which pixels in the image are used to compare the feature vectors in (41) and (50). This neighbourhood window should not be confused with the patch explained in Section 7.1, as the patch was used to build the feature vector (\mathbf{f}_j and \mathbf{f}_l) for each pixel. The parameters of neighbourhood size and a are based on testing different values. In multi-scale wavelet kernels, multiple single-scale wavelet kernels with different scales both large and small are combined. Therefore, they are expected to be more flexible than single-scale wavelet kernels. Also, they are not dependent on the choice of a .

7.3 Gabor Spatial Weighting

In previous chapters, spatial weighting is included in the kernel construction to account for spatial distance between the pixel of interest and neighboring pixels in the

neighborhood when global k NN was not used. In this chapter, simulated data is a 2D MR image and the PET data is static, therefore, a two-dimensional Gaussian weight was given to the pixels in the neighborhood in a similar way explained in previous chapters. This weighting kernel is then multiplied pointwise by the kernel extracted based on feature vectors. Similar to methods used in [9] and Chapter 5, a regional k NN is used to identify the neighbouring pixels which can be used for weight calculation of each pixel in the image.

In this section Gabor filter [73] is introduced for spatial weight calculation instead of Gaussian weighting in equation (23). Gabor filters are modulation products of Gaussian and sinusoidal signals and can be used for different image processing applications such as texture analysis and edge detection [74], [75]. The Gabor filter analyzes the image to check if there is directionality in a certain scale in a region of the image. Unlike the Gaussian function which creates spatial weighting in terms of distance from the centre pixel, with Gabor filtering the spatial weighting is largely in terms of directionality and wavelength. Gabor filters have a real and imaginary component. The complex formula is

$$Ga = \exp\left(-\frac{x'^2 + \gamma^2 y'^2}{2\sigma^2}\right) \exp\left(i\left(2\pi\frac{x'}{\lambda} + \chi\right)\right) \quad (52)$$

and the real and imaginary parts are as follows, respectively

$$R_Ga = \exp\left(-\frac{x'^2 + \gamma^2 y'^2}{2\sigma^2}\right) \cos\left(2\pi\frac{x'}{\lambda} + \chi\right) \quad (53)$$

$$I_Ga = \exp\left(-\frac{x'^2 + \gamma^2 y'^2}{2\sigma^2}\right) \sin\left(2\pi\frac{x'}{\lambda} + \chi\right) \quad (54)$$

where $x' = x\cos\theta + y\sin\theta$ and $y' = -x\sin\theta + y\cos\theta$ and θ represents the direction or orientation and x' and y' are rotated by it, $\theta = 0$ degrees correspond to the vertical position for the Gabor filter and $\theta = 90$ degrees correspond to the horizontal position. χ is the phase

offset of the sinusoidal. λ is the wavelength of the sinusoidal component and it controls the width between two peaks in sinusoidal (seen as stripes in a 2D Gabor filter) of the Gabor function. Increasing the wavelength is seen as thicker stripes in a Gabor filter and decreasing the wavelength produces thinner stripes.

γ is the spatial aspect ratio which specifies the ellipticity of the support of the Gabor function. In 2D Gabor filter it is seen as the amount the kernel is stretched along the kernel wave pattern. σ is the width of the Gaussian envelope. It controls the overall size of the Gabor envelope. For larger bandwidth the envelope increase allowing more stripes in it and with small bandwidth the envelope tightens.

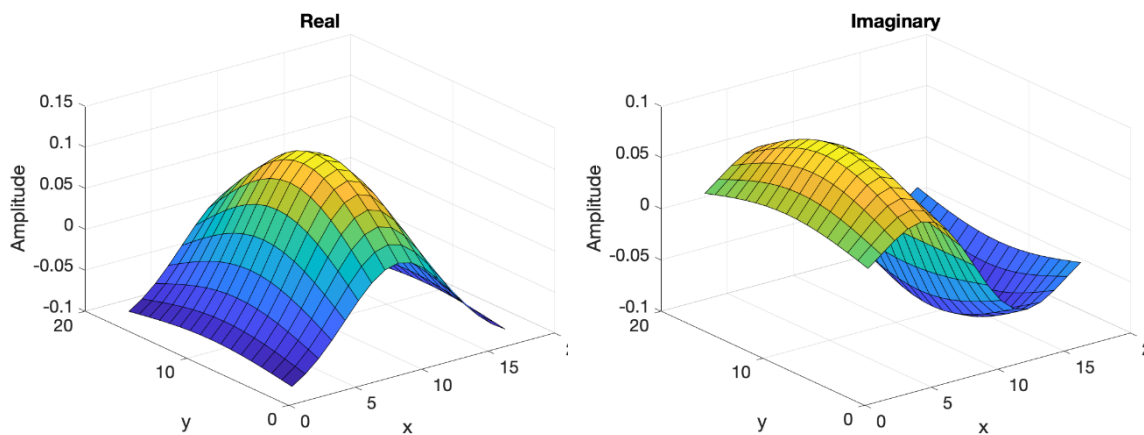


Figure 41. Real and imaginary part of the Gabor filter for given parameters.

The real and imaginary part of the Gabor filter are shown for a set of parameters in Figure 41 as an example. For this figure $\theta = 90$, $\lambda = 1$, $\psi = 0$, $\gamma = 0.5$ and $\sigma = 4$. Gabor filters for a set of combinations of parameters are shown in Figure 42 from the MATLAB

function for Gabor filter. In this function σ is set to be equal to $\frac{\lambda}{3\pi\sqrt{\frac{\log(2)}{2}}}$ and $\lambda = \{2,4,6\}$

and $\theta = \{0,30,60,90,120,150\}$ degrees.

In signal processing, Gabor filters are used for edge detection or feature extraction [74], [75]. In this work, using Gabor weighting will help in identifying the direction of edges in each neighborhood and define the weights based on that directionality to avoid smoothing out edges. The method used to include Gabor filters in the weight's calculation was through a Gabor filter bank. The Gabor filter bank was defined as a combination of orientation and the wavelength of the sinusoids. The orientation is defined as the normal direction to the sinusoidal plane wave. Then the image is filtered with the Gabor filter bank by convolution as

$$\mathbf{I}_{g(\lambda,\theta)} = \mathbf{I} * \text{Ga}_{\lambda,\theta} \quad (55)$$

where $\text{Ga}_{\lambda,\theta}$ is the filter bank with different λ and θ values, \mathbf{I} is the MRI image and $\mathbf{I}_{g(\lambda,\theta)}$ is the filtered MRI image. At each pixel location there is a magnitude for each of the entries of the filter bank. The magnitude for all the cases of the filter bank are thresholded to avoid any small value without a significant directional component signal

$$\mathbf{I}_{g(\lambda,\theta)} = \begin{cases} \mathbf{I}_{g(\lambda,\theta)} & \mathbf{I}_{g(\lambda,\theta)} > T \\ 0 & \mathbf{I}_{g(\lambda,\theta)} < T \end{cases} \quad (56)$$

where $\mathbf{I}_{g(\lambda,\theta)}$ is the magnitude of filtered image with the Gabor filter related to λ, θ from the filter bank. Then the maximum magnitude between all the filtered results from the filter bank is considered to correspond to the correct combination of direction and wavelength for that pixel.

$$(\lambda, \theta)_{\{x,y\}} = \text{argmax} (\mathbf{I}_{g(\lambda,\theta)}(x, y)) \quad (57)$$

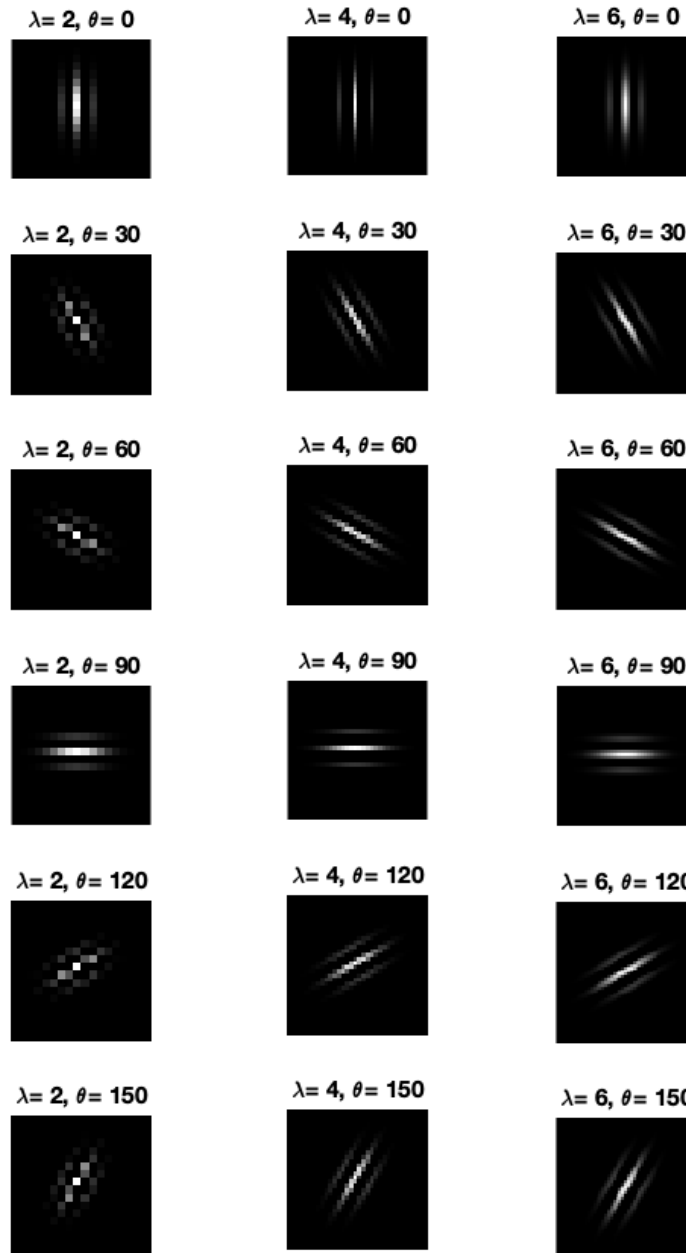


Figure 42. Gabor filters of three wavelengths and six directions.

With the calculated direction and wavelength for each pixel, the real component of the Gabor filter is formed based on the selected neighbourhood size. If the magnitude is set to zero in thresholding, then no direction and wavelength is selected, and a Gaussian filter is used instead. When the combination of (λ, θ) which results in the maximum magnitude for each pixel location is known, it is used in the Gabor filter equation (55) resulting in the

Gabor filter coefficient at that specific pixel. With all the coefficients for all the pixel locations, the Gabor weight matrix is constructed. This weighting is then multiplied with the multi-scale wavelet kernel explained in Section 7.2 to include both multi-scale wavelet and multi-directionality of the Gabor filter in the kernel calculation.

It should be noted that the multi-scale Morlet wavelet can also be used with the Gaussian spatial weighting and the comparison with the multi-scale Morlet wavelet with Gabor spatial weighting will show the effectiveness of Gabor filter.

7.4 Simulation Study

For the simulation study, PET scans were simulated using a head phantom. As shown in Figure 40, the MR image is from the brainWeb project [76] with 256×256 pixels in the axial plane with 1 mm isotropic pixel size. To generate a simulated PET image, the interior tissue was segmented into grey matter and white matter with intensity values of 40 and 10, respectively. A circular lesion with diameter of 11 pixels and intensity of 80 was then added to the white matter in the PET image. The activity image is forward projected and multiplied by attenuation map to form a noise-free sinogram. To simulate scatter and random coincidences, 20% of the mean of the noise-free sinogram is then added to the noise-free sinogram. Then, Poisson noise is introduced to the sinogram with 200k total coincidence events.

To apply regional k NN in a 7×7 window, $k = 16$ nearest neighbours are found for each pixel (within this window). Similar to Hutchcroft et al. [8], the patch size here is a 3×3 patch, therefore $T = 9$ in equation (49). The weight matrix derived from the Gabor filters by the procedure explained in Section 7.3, is used for spatial weighting in multi-scale wavelet kernel. For equation (51), a_z is chosen as powers of 2: $a_z \in$

$\{1, \dots, 2^{0.25z}, \dots, 2^{0.25(Z-1)}\}$ with $Z = 6$, similar to [62]. In STI wavelet, values smaller than 1 for a results in very noisy reconstructions which will be shown in Figure 46 further in the chapter, therefore the chosen a_z do not include values smaller than 1. Other values for a_z which are not powers of 2 have been tested and no significant difference was seen, therefore for simplicity of the choice a_z is selected as powers of 2 and $a = 1$ for (43).

For identifying the correct Gabor filter for the chosen neighborhood, a Gabor filter bank is applied to the whole MR image using different wavelengths and directions. The wavelengths of the sinusoids are selected as $\{2,4,6\}$ pixels/cycle and the orientation vector for the Gabor filter bank is set to $\{0,15,30,45,60,75,90,105,120,135,150,165\}$ degrees with respect to the horizontal. Then for each pixel the wavelength and direction which gives the maximum magnitude for the Gabor filter is selected. To be consistent with how the k NN of f_j is defined, for the chosen wavelength and direction the real part of the Gabor filter is calculated based on a 7×7 window size and this weighting kernel is used in the reconstruction process combined with the multi-scale wavelet kernel.

The proposed MR-based multi-scale wavelet kernel with Gabor directionality was compared to single-scale wavelet kernel and Gaussian kernel. These results are also compared with standard MLEM reconstruction. Figure 43 shows the reconstruction results with 40 iterations along with the phantom. KEM reconstruction refers to the kernel-based reconstruction using MR information [8]. The MR image in Figure 40 does not show the tumor present in the PET image but the reconstruction using kernel from this MR image is able to reconstruct the tumor. Figure 43(a) middle row shows the reconstruction results with the MR image in Figure 40. As can be seen from this row the tumor is best represented

in the case where the multi-scale wavelet combined with directionality property of Gabor filter is used for kernel-based reconstruction.

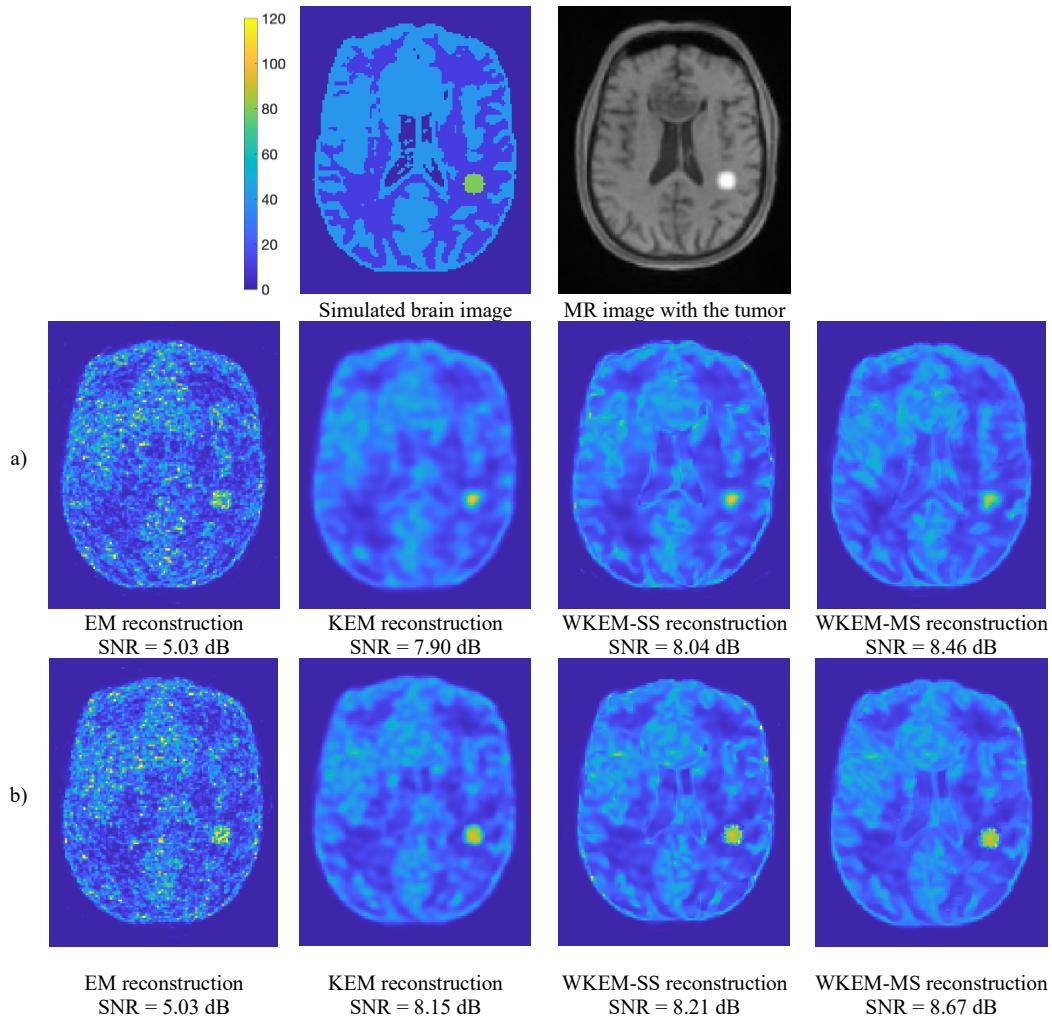


Figure 43. Simulated brain image with different PET reconstruction methods. (a) Middle row is from MRI without tumor and (b) the bottom row is with tumor present in MR image

Figure 43(a) also shows that with the MR image without tumor as prior information, KEM has already removed noise that is present in MLEM reconstruction, but it also smooths the image. In the figure, WKEM-SS refers to wavelet-based KEM with single-scale wavelet. The single-scale wavelet sharpens the image but there are some artifacts, especially at the border of the phantom. WKEM-MS, which refers to multi-scale wavelet-based KEM with Gabor directionality, removes the noise from the border while

preserving the sharpness of the edges, which improves the visual quality of the reconstructed image.

The bottom row of the Figure 43 (Figure 43(b)) is the reconstruction results with tumor present in MR image as well and the overall SNR of the image is shown for each method. It also shows that the tumor is reconstructed closer to true size when it is present in MR image as well. The SNR values indicate that WKEM-MS outperforms WKEM-SS and the original KEM with MR in both cases (with and without tumor present in MR image).

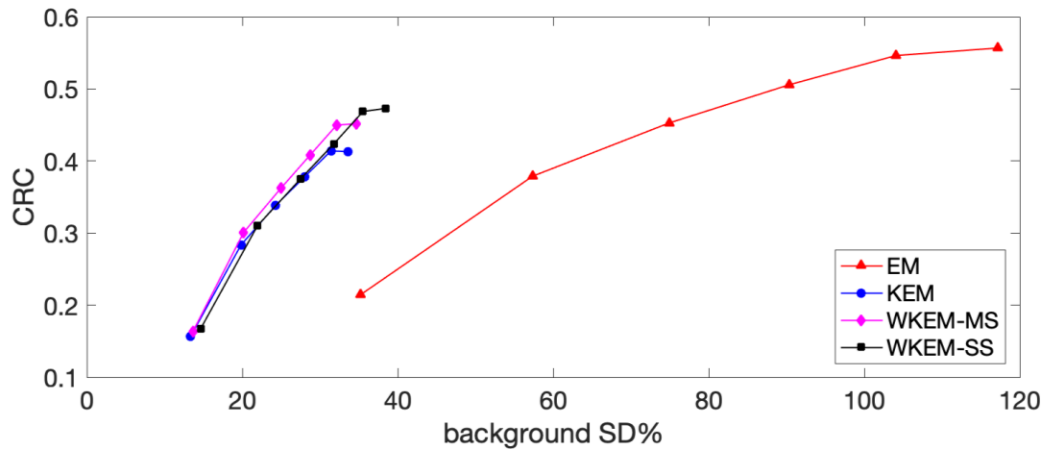


Figure 44. Contrast recovery versus background standard deviation for simulated brain phantom calculated for tumor region.

To see the effect of mismatch between PET and MR, for the following figures, the MR image without the tumor is used as the source of prior information. In Figure 44, CRC versus background SD percentage is shown for the tumor region (shown in green in simulated brain image in Figure 43(a)) by varying the iteration number from 10 to 60 with 10 iterations having the smallest CRC value and 60 iterations having the largest CRC value in each method. WKEM-SS has a slightly higher CRC than WKEM-MS but the background standard deviation is also higher in WKEM-SS. This is the reason distortion is present in WKEM-SS which is not visible in WKEM-MS.

From this figure, it can be concluded that there is a trade-off between WKEM-SS and WKEM-MS in terms of CRC and background standard deviation. But since the visual quality and SNR in WKEM-MS is higher, it is desired over the WKEM-SS. Figure 44 suggests that both WKEM methods have higher CRC than KEM. All kernel-based methods are also superior to MLEM.

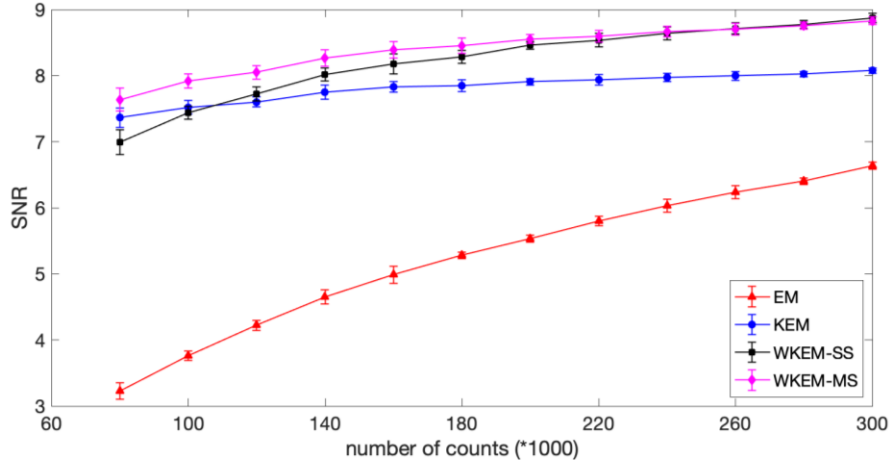


Figure 45. SNR value for different number of coincidence events with 40 iterations and 10 realizations

In Figure 45, different number of counts (coincidence events) are tested with 10 realizations and the iteration number fixed to 40. SNR is calculated using different methods. The error bars are also shown in the figure and are calculated as standard deviation from the mean value of SNR. From this figure, it can be seen that for low number of counts, WKEM-MS is superior to all the other methods. As the number of counts increases, SNR for WKEM-SS and WKEM-MS are getting closer together and when the number of counts is very large WKEM-SS is having slightly higher SNR. This might be because when there is high enough number of points, setting the wavelet parameter to a fixed value (a) which gives the best result is better than combining different values of a_z . However, for the real case where usually the number of counts is minimum to minimize

patient exposure, WKEM-MS is still able to recover the image with higher SNR than WKEM-SS and the original KEM with Gaussian kernel.

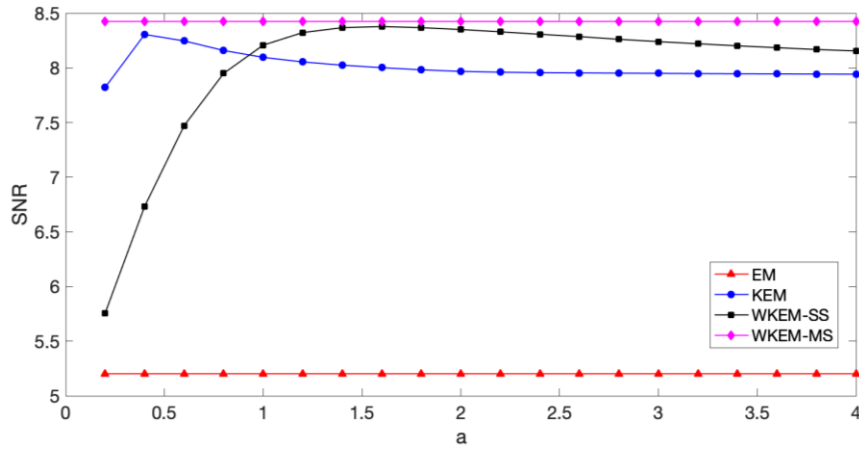


Figure 46. SNR for different "a" values with 40 iterations and 200K coincidence events.

To see the effect of different parameters in the quality of reconstructed image, SNR is calculated by varying the value of a for KEM and WKEM-SS. The SNR values are then compared with WKEM-MS kernel as well. This is shown in Figure 46 with fixed iteration number and number of counts. In this figure, it is shown that WKEM-MS is superior than KEM and WKEM-SS, no matter what value of a is selected. It should be noted that the

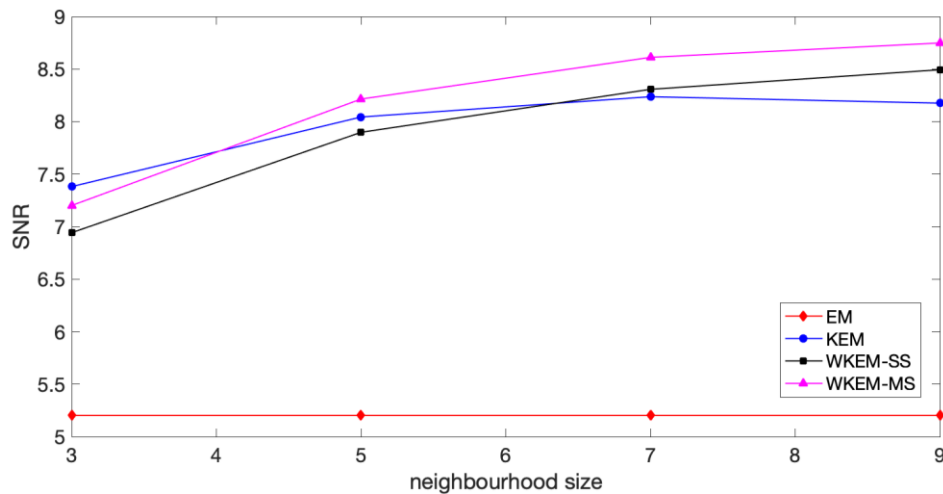


Figure 47. SNR for different neighbourhood sizes with 40 iterations and 200K coincidence events. For a 3×3 neighbourhood, 5 pixels are chosen in k NN, for 5×5 neighbourhood 10 pixels are chosen, and for 7×7 and 9×9 neighbourhoods 16 and 20 pixels are chosen respectively

SNR value in MLEM and WKEM-MS do not depend on " a " and therefore they are fixed in this figure.

Different neighbourhood sizes have also been tested and the SNR for different reconstruction methods are shown in Figure 47. We can see in this figure that for a 3×3 neighbourhood, SNR values are very small in all cases and for 7×7 and 9×9 neighbourhoods the SNR is in an acceptable range. The 7×7 neighbourhood is selected to not lose too much information from the tumor region and still get high SNR value.

To compare the visual quality of reconstructed images, structural similarity index (SSIM) is calculated [77]. SSIM has been widely used on image processing literature as a method of comparing visual quality. SSIM represents the visual aspects of the image better than SNR and therefore is a useful method for comparing reconstruction methods. The values of SSIM for different reconstruction methods are shown in Table 4. SSIM is defined in a way that it would have a value between zero and one. The larger the value, the more similar is the image to the original image. The SSIM value is an average of the similarity over the pixels of the image, in this case the brain region pixels (excluding the background).

Table 4. SSIM values for different reconstruction methods. The values are averaged over 10 realizations.

	MLEM	KEM	WKEM-SS	WKEM-MS
SSIM	0.1356	0.1855	0.2112	0.2177

To check structural similarity locally, the SSIM map can be formed. It is an image with the same size as the original image and shows local differences all over the image. The larger the value in SSIM map the higher fidelity the image has with the original image (the simulated brain image in this case). Figure 48 shows the SSIM map for the reconstructed images of all four reconstruction methods. The second column is zoomed

over the rectangular in the image to show the result on the border more clearly. As can be seen from this figure, the borders have higher SSIM values in WKEM-MS method, especially in comparison to KEM. This confirms the statement about multi-scale kernel method with Gabor directionality being able to better preserve edges.

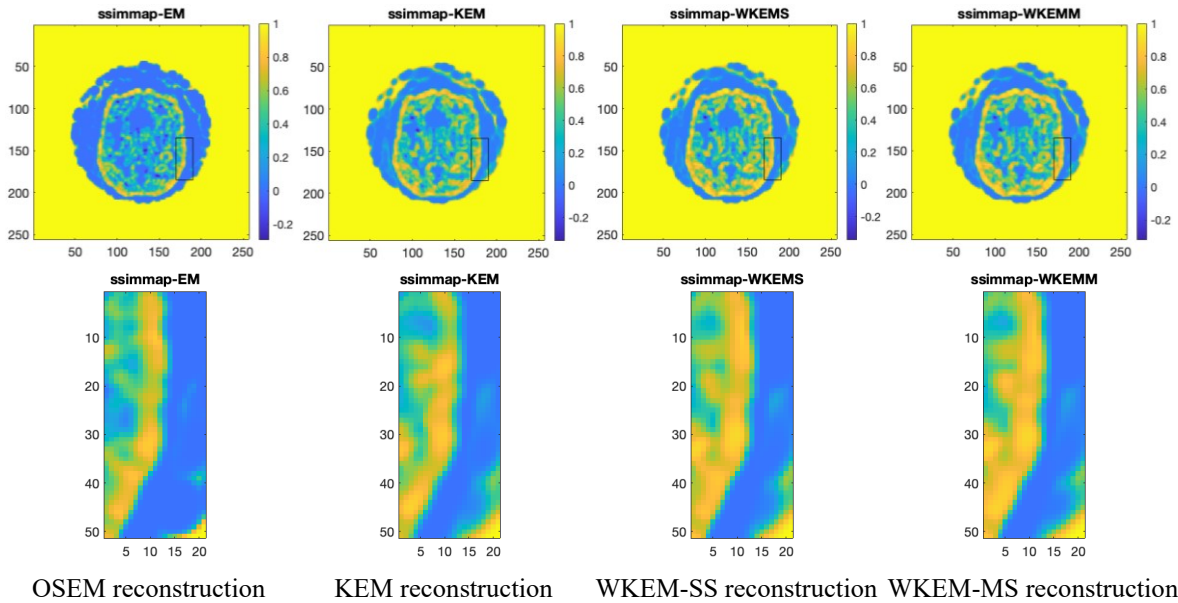


Figure 48. SSIM map for reconstructed images of different methods. The high value of SSIM map shows higher structural similarity between the reconstructed image and the reference image. The second column is the part shown in rectangular of the first column.

To see the effect of Gabor weighting, the multi-scale wavelet kernel was also applied with Gaussian spatial weighting and the results are compared to the multi-scale wavelet method with Gabor weighting in Figure 49. The results are shown for two cases with the tumor present in MR image and without the tumor in the MR image. For both cases the reconstruction of the tumor area is pretty much similar but the difference is in the edges of the brain region, which has less noise with Gabor weighting than the Gaussian weighting. SNR values are also higher for the multi-scale wavelet with Gabor weighting.

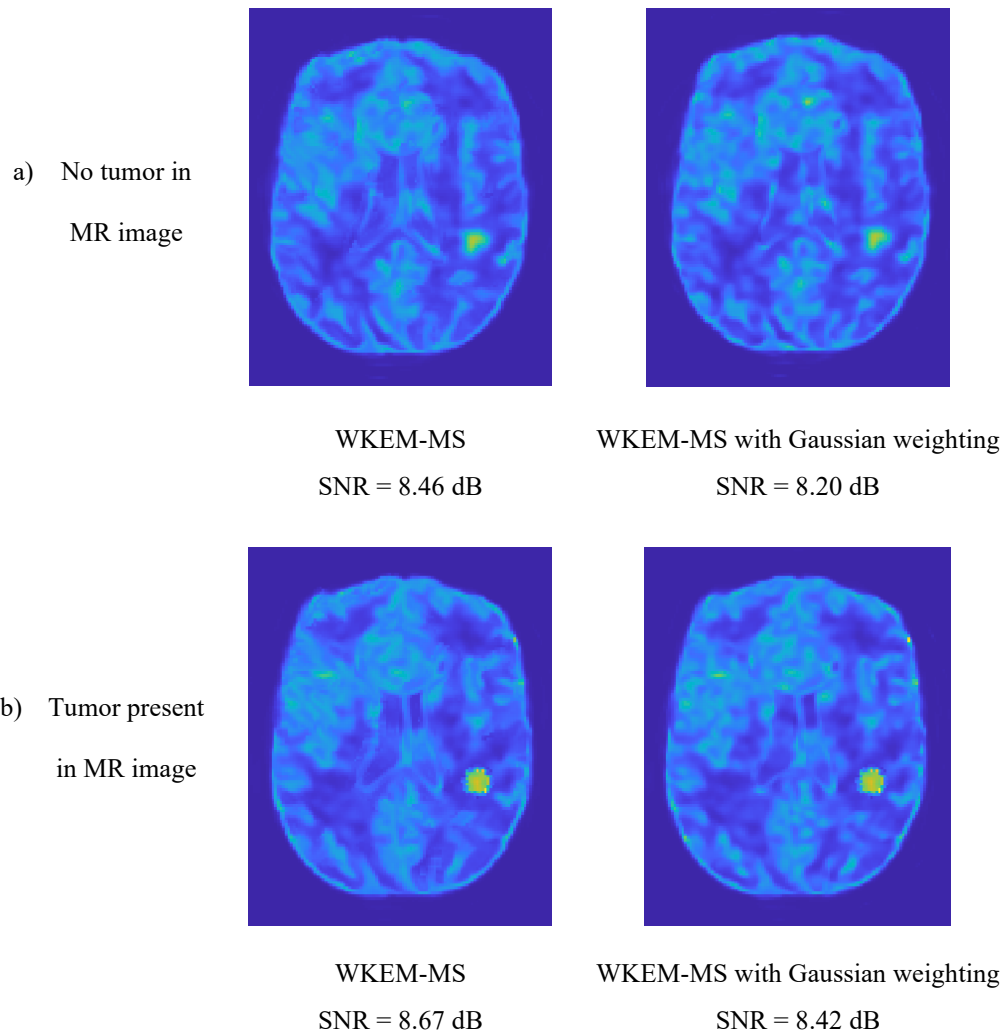


Figure 49. Reconstructed images of the simulated brain comparing multi-scale wavelet with Gaussian weighting and multi-scale wavelet with Gabor weighting.

7.5 Patient Data

The patient data are from the Ottawa Heart Institute and the use of this data is approved by research ethics board presented in appendix D. The data were also anonymized before analysis. Since for patient data there is no ground truth available, SNR and contrast are defined based on equations (26) and (27) defined in Chapter 3.

As in Chapter 6, static PET scans of three patients with HED tracer on a GE D600 PET/CT scanner is used. Since no data from a commercial PET-MR scanner was available,

static PET and MRI are acquired separately from different machines and at different times. Consequently, registration is required between the two image modalities. Registration was performed using the Elastix software [2]. Similar to Section 6.2, MR images are acquired from a Siemens Aera magnetic resonance scanner with magnetic field strength of 1.5 T and SSFP acquisition protocol was chosen. The images were acquired at end-expiration and end-diastole using respiratory-navigators and ECG-gating.

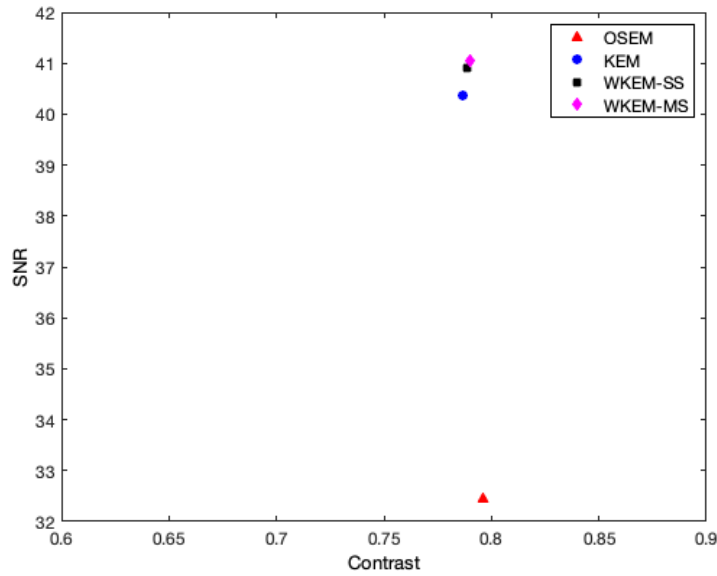


Figure 50. SNR versus contrast averaged over three patients showing OSEM, KEM, WKEM-SS and WKEM-MS

The Gaussian kernel parameter σ is set to 1 and for single-scale WKEM, a is 1. For WKEM-MS, a_z is selected similar to the simulation study. Figure 50 shows average SNR versus contrast for three patients using all four methods. KEM, WKEM-SS and WKEM-MS have preserved contrast value and SNR is higher for WKEM-MS. The exact values are also given in Table 5. There is a slight increase in SNR and contrast values for WKEM-MS in comparison to WKEM-SS.

The reconstruction result from one of the patients is shown in Figure 51. The visual

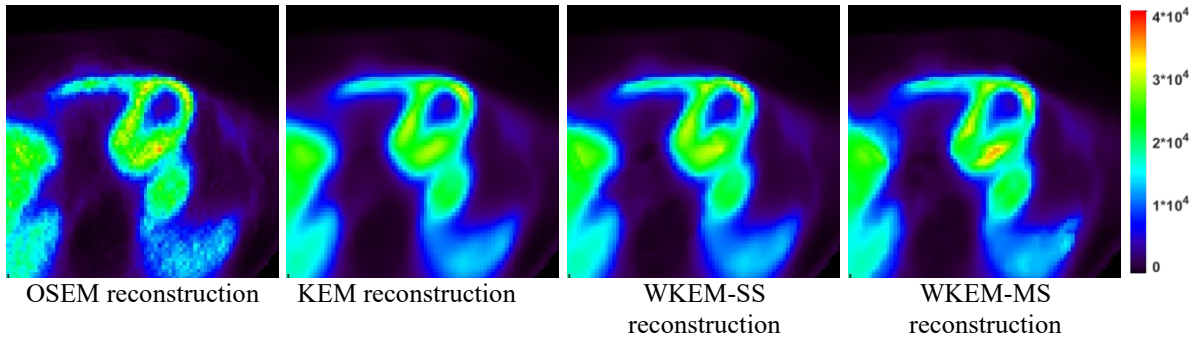


Figure 51. Patient data showing reconstruction result of left and right ventricle.

quality of the reconstructed images is very much similar between the single-scale WKEM and multi-scale WKEM, except for some parts in the left ventricle wall in which WKEM-MS is better able to recover the high intensity values that are present in OSEM reconstruction. It should be noted that the quality of reconstruction for patient data is limited by co-registration accuracy, which is not perfect. Using data from a simultaneous PET-MR machine may help in eliminating registration mismatch in reconstruction.

Table 5. Average SNR and contrast values for three patients

	OSEM	KEM	WKEM-SS	WKEM-MS
Avg SNR (dB)	32.45	40.37	40.90	41.03
Contrast	0.7962	0.7866	0.7888	0.7902

Another difference between simulation data and patient data is motion in patient data. Although the images are static, patient motion is still present in the time span the PET image is acquired while motion is not included in the simulation data. Because of these sources of artifacts in real patient data, the comparison between different reconstruction methods is limited for patient data while the simulated brain data does not contain these mismatches.

7.6 Summary

In this chapter, a multi-scale wavelet kernel method is proposed to improve PET image reconstruction with MR anatomical prior information. The directionality information of the MR image is also included with the use of the Gabor filter. The results from the simulation study show that the multi-scale wavelet kernel with Gabor directionality, can achieve slightly higher SNR than conventional KEM with Gaussian kernel and single-scale wavelet. It has also higher SNR than multi-scale wavelet with Gaussian weighting. The multi-scale wavelet kernel with Gabor directionality, can preserve high intensity values and it also removes the artifacts present at the edges if single-scale wavelet is used and therefore results in better spatial resolution. Real data from patient study also confirms higher SNR value and preservation of visual detail in WKEM-MS than other methods.

Chapter 8 : Conclusions and Future Work

8.1 Conclusions

This thesis is based on kernel PET image reconstruction. In this work alternative kernels were developed based on wavelet functions which had not been applied to PET image reconstruction before. Introducing wavelets in kernel PET image reconstruction is a novel application of the wavelet kernels. It has been shown that the kernels defined based on the wavelets result in better preservation of the contrast and quality of edges. The developed techniques are tested in different datasets such as simulated brain data, physical NEMA phantom and real patient data and for prior information from two distinct sources, dynamic PET series and from MR images.

Introducing the wavelet method for dynamic PET image reconstruction and its assessment using computer simulated data, physical phantoms, and patient scans enables us to carefully study the method in different settings and organ structures in the tissue being imaged. Results from simulated brain data in Chapter 5 show that the WKEM method achieved a higher SNR compared to KEM for the low-count frames (early frames) in which the blood pool in brain has a high activity. However, for later frames, the two approaches had similar SNR, the shape of the tumor using WKEM is more consistent with the ground truth. The analysis for simulated brain data also showed that WKEM can achieve higher contrast recovery than conventional KEM for low-count frames. The results also show that for high count frames Gaussian kernel will result in reconstruction images with similar SNR value. So, with even more counts it might be possible that the Gaussian kernel would result in better reconstructed images than wavelet kernel but it needs more experiments. The NEMA phantom study suggests WKEM can reconstruct images with higher contrast

recovery, especially for smaller spheres. This method results in an increase of around 20% in contrast recovery for the smallest sphere which is significant. This confirms the statement about the WKEM method being better than KEM in the reconstruction of small objects. Consistent with these results, the study using cardiac patient data in same chapter (Chapter 5) demonstrated improvement of the left ventricle SNR using WKEM kernel reconstruction over KEM and OSEM methods. The visual comparison of reconstructed images of the cardiac patient data also show WKEM was better in preserving edges in left ventricle wall than KEM method.

In Chapter 7, the wavelet kernel for PET image reconstruction has been used to develop a kernel method which extracts the kernel from MR information. For this goal, multi-scale wavelet kernel was proposed and evaluated using brain simulation study and patient data. In multi-scale wavelet kernels, multiple single-scale wavelet kernels with different scales both large and small are combined. Therefore, they are more flexible than single-scale wavelet kernels and better able to capture local behaviors of data, and there is no need to tune the dilation coefficient (a parameter) in single-scale wavelet. Directionality information was also extracted from the MR image by Gabor filtering and used in the kernel construction. Simulation study shows that the multi-scale wavelet kernel with Gabor directionality can achieve higher SNR than conventional KEM and single-scale wavelet. The results were also compared with the multi-scale wavelet kernel with Gaussian spatial weighting (No Gabor weighting) and it showed that including the directionality information along with the multi-scale wavelet, increases the SNR value. The multi-scale wavelet kernel with Gabor directionality, can preserve high intensity values and it also removes some artifacts which are present at the edges if single-scale wavelet is used, and

therefore results in better accuracy. The multi-scale directional wavelet was also tested using cardiac patient data and these evaluations demonstrated an increase in SNR value in the left ventricle of the heart. However, since the number of patients is small, a larger patient data set might be needed to confirm the results. There might be cases with some patient data where single-scale wavelet works as good or better than the multi-scale wavelet (with or without directionality) and that needs more investigation.

8.2 Future work

My work presented here was to investigate new kernel methods with different kernels on different feature vectors (dynamic PET or MR) to reconstruct PET images. There are several ways this work can be extended.

- The patient data is limited to a small number; for a more comprehensive comparison it would be useful to have more patient data and including other PET tracers as well.
- Another approach which may help the work to improve is to include motion compensation to further improve image resolution, especially for real data which will further benefit from a reconstruction method which included motion compensation.
- The emphasis in this thesis is on image quality enhancement and did not focus on the effect of the method in diagnostic accuracy. It might be useful to evaluate diagnostic accuracy and the effect of kernel reconstruction methods, especially the wavelet kernel method.
- To increase the quality of the reconstructed images with dynamic series as prior information, an alternative method would be to reconstruct all the frames (instead

of only three composite frames) with OSEM and then use the reconstructed images to extract the multi-scale wavelet kernel directly and use that kernel to reconstruct the whole series again. This is not as efficient in terms of time and resources but for cases where quality of reconstruction is much more important, and if the time and CPU resources are available, then might be able to provide even higher quality in the reconstructed image.

Some aspects of the kernel image reconstruction that were not fully explored in this thesis might be interesting to continue:

- Including regularizers with kernel image reconstruction. Regularizers are included in the image reconstruction to reduce noise but in the kernel method since the noise is handled during the reconstruction, there is no need for a regularizer which reduces the noise. But a regularizer could be added to preserve edge information since kernel methods tend to smooth edges for noise reduction. Therefore, it will be beneficial to include edge-preserving regularizer and there is a potential increase in the quality of edges in the reconstructed images.
- Another future direction can be on the method for calculating the kernel. The kernel can be extracted by deep learning methods. A neural network can be used to extract the features using prior information, which could be either composite images from dynamic PET series and/or from MR images. These features can then be used with the methods described in this thesis to calculate the kernel by wavelet or Gaussian kernel. The features extracted from deep learning would need to contain all the necessary information for a good quality image reconstruction. One option may be to use autoencoders [78]. An autoencoder consists of two parts: an encoder part that

maps the input into a set of features, and a decoder that maps the features to a reconstruction of the input. The features are expected to contain structure information in the data and therefore can be used for kernel construction with any of the described kernels in this thesis.

Appendix

Appendix A - Projection-slice theorem

Based on this theory, a 1D Fourier transform of a projection is a slice of the 2D Fourier transform of the object [24].

The 1D Fourier transform of a projection is

$$G(\rho, \theta) = F_{1D}\{g(l, \theta)\} = \int_{-\infty}^{\infty} g(l, \theta) \exp(-j2\pi\rho l) dl. \quad A.1$$

where $g(l, \theta) = \int_{-\infty}^{\infty} \int_{-\infty}^{\infty} f(x, y) \delta(x \cos \theta + y \sin \theta - l) dx dy$, is the line integral of the image function [24].

Therefore equation A.1 would be:

$$G(\rho, \theta) = \int_{-\infty}^{\infty} \int_{-\infty}^{\infty} \int_{-\infty}^{\infty} f(x, y) \delta(x \cos \theta + y \sin \theta - l) \exp(-j2\pi\rho l) dx dy dl \quad A.2$$

Due to the impulse function the result would be simplified to [24]

$$\begin{aligned} G(\rho, \theta) &= \int_{-\infty}^{\infty} \int_{-\infty}^{\infty} f(x, y) \int_{-\infty}^{\infty} \delta(x \cos \theta + y \sin \theta - l) \exp(-j2\pi\rho l) dl dx dy \\ &= \int_{-\infty}^{\infty} \int_{-\infty}^{\infty} f(x, y) \exp(-j2\pi\rho(x \cos \theta + y \sin \theta)) dx dy. \end{aligned} \quad A.3$$

On the other hand based on the definition of the 2D Fourier transform, the Fourier transform of the object can be written as [24]

$$\begin{cases} F(u, v) = \int_{-\infty}^{\infty} \int_{-\infty}^{\infty} f(x, y) \exp(-j2\pi(xu + yv)) dx dy \\ u = \rho \cos \theta, \quad v = \rho \sin \theta \end{cases} \quad A.4$$

With a change of parameter for u, v , equations A.3 and A.4 are identical, therefore

$$G(\rho, \theta) = F(\rho \cos \theta, \rho \sin \theta). \quad A.5$$

To be able to identify the object, the inverse 2D Fourier transform $F(u, v)$ is calculate as

$$f(x, y) = F_{2D}^{-1}\{F(u, v)\} = \int_{-\infty}^{\infty} \int_{-\infty}^{\infty} F(u, v) \exp(j2\pi(xu + yv)) dudv. \quad A.6$$

Setting $u = \rho \cos \theta$ and $v = \rho \sin \theta$ and $dudv = \rho d\rho d\theta$, equation A.6 would become

$$\begin{aligned} F_{2D}^{-1}\{F(u, v)\} &= \int_0^{2\pi} \int_0^{\infty} F(\rho \cos \theta, \rho \sin \theta) \exp(j2\pi\rho(x \cos \theta + y \sin \theta)) \rho d\rho d\theta = \\ &= \int_0^{2\pi} \int_0^{\infty} G(\rho, \theta) \exp(j2\pi\rho(x \cos \theta + y \sin \theta)) \rho d\rho d\theta = \\ &= \int_0^{\pi} \int_{-\infty}^{\infty} |\rho| G(\rho, \theta) \exp(j2\pi\rho(x \cos \theta + y \sin \theta)) d\rho d\theta \end{aligned} \quad A.7$$

Since $x \cos \theta + y \sin \theta = l$ is a constant value

$$F_{2D}^{-1}\{F(u, v)\} = \int_0^{\pi} \left[\int_{-\infty}^{\infty} |\rho| G(\rho, \theta) \exp(j2\pi\rho l) d\rho \right] d\theta \quad A.8$$

which is a slice of the 2D Fourier transform of the object.

Appendix B - Proof that Morlet wavelet satisfies Mercer's condition

As stated in the thesis, for a kernel to satisfy Mercer's condition the Fourier transform in (29) can be used which is

$$\hat{k}(\omega) = (2\pi)^{-N/2} \int \exp(-j(\omega x)) k(x) dx \geq 0 \quad B.1$$

for all ω , where

$$k(x) = \prod_{i=1}^N \cos\left(\frac{1.75x_i}{a}\right) \exp\left(-\frac{x_i^2}{2a^2}\right). \quad B.2$$

Substituting B.2 in B.1 would result in

$$\hat{k}(\omega) = (2\pi)^{-N/2} \prod_{i=1}^N \int \exp\left(-j\omega_i x_i - \frac{x_i^2}{2a^2}\right) \cos\left(\frac{1.75x_i}{a}\right) dx_i. \quad B.3$$

To provide the proof, I would first state the general complex Morlet wavelet transform for a given signal $s(t)$ [79]

$$\tilde{s}(a, \tau) = \int_{-\infty}^{\infty} s(t) \frac{1}{\sqrt{a}} \exp \left(-jk_0 \frac{t - \tau}{a} - \frac{(t - \tau)^2}{2a^2} \right) dt \quad \text{B.4}$$

where $\frac{1}{\sqrt{a}} \exp \left(-jk_0 \frac{t - \tau}{a} - \frac{(t - \tau)^2}{2a^2} \right)$ is the dilated and translated version of the complex Morlet mother wavelet function $\exp(-jk_0 t) \exp \left(-\frac{t^2}{2} \right)$ and $\tau, a \in R^+$ are the translation and dilation factors respectively. By setting $s(t) = \cos(\omega_n t)$ and $a = \frac{k_0}{\omega}$, equation B.4

becomes

$$\begin{aligned} \tilde{s}(a, \tau) &= \int_{-\infty}^{\infty} \cos(\omega_n t) \exp \left(-j\omega(t - \tau) - \frac{(t - \tau)^2}{2a^2} \right) \frac{\sqrt{\omega}}{\sqrt{k_0}} dt \\ &= \sqrt{\frac{\pi k_0}{2\omega}} \left[\cos(\omega_n \tau) \left(\exp \left(\frac{-(\omega_n - \omega)^2 k_0^2}{2\omega^2} \right) + \exp \left(\frac{(\omega_n - \omega)^2 k_0^2}{2\omega^2} \right) \right) \right. \\ &\quad \left. + j \sin(\omega_n \tau) \left(\exp \left(\frac{-(\omega_n - \omega)^2 k_0^2}{2\omega^2} \right) - \exp \left(\frac{(\omega_n - \omega)^2 k_0^2}{2\omega^2} \right) \right) \right] \quad \text{B.5} \end{aligned}$$

If τ is set to 0, $\omega_n = \frac{1.75}{a}$ and $t = x_i$ in B.5, then equation B.5 would become

$$\begin{aligned} \tilde{s}(a, 0) &= \frac{1}{a} \int_{-\infty}^{\infty} \cos \left(\frac{1.75 x_i}{a} \right) \exp(-j\omega x_i) \exp \left(-\frac{x_i^2}{2a^2} \right) dx_i \\ &= \sqrt{\frac{\pi a}{2}} \left(\exp \left(\frac{-\left(\frac{1.75}{a} - \omega \right)^2 a^2}{2} \right) + \exp \left(\frac{\left(\frac{1.75}{a} - \omega \right)^2 a^2}{2} \right) \right) \quad \text{B.6} \end{aligned}$$

looking at equation B.6, it can be seen that it is equal to the equation B.3 and since equation B.6 is always positive, it has been proved that $\hat{k}(\omega) \geq 0$ for the translation invariant kernel constructed using the Morlet mother wavelet. In this proof $k(x)$ is defined based on central frequency of 1.75 for Morlet. Changing the central frequency to other frequencies mentioned in the text would not change the proof and it is still valid.

Appendix C - Permission to reproduce published material

This appendix contains letters of permissions to include previously published articles in this thesis.

10/6/21, 8:35 PM

Rightslink® by Copyright Clearance Center



Home Help Email Support Sign in Create Account

Kernel-Based Reconstruction of C-11-Hydroxyephedrine Cardiac PET Images of the Sympathetic Nervous System



Conference Proceedings:

2019 41st Annual International Conference of the IEEE Engineering in Medicine and Biology Society (EMBC)

Author:

[Zahra:] [Ashouri:]; Chad R. Hunter; Benjamin A. Spencer; Guobao Wang; Richard M. Dansereau; Robert A. deKemp

Publisher: IEEE

Date: 23-27 July 2019

Copyright © 2019, IEEE

Thesis / Dissertation Reuse

The IEEE does not require individuals working on a thesis to obtain a formal reuse license, however, you may print out this statement to be used as a permission grant:

Requirements to be followed when using any portion (e.g., figure, graph, table, or textual material) of an IEEE copyrighted paper in a thesis:

- 1) In the case of textual material (e.g., using short quotes or referring to the work within these papers) users must give full credit to the original source (author, paper, publication) followed by the IEEE copyright line © 2011 IEEE.
- 2) In the case of illustrations or tabular material, we require that the copyright line © [Year of original publication] IEEE appear prominently with each reprinted figure and/or table.
- 3) If a substantial portion of the original paper is to be used, and if you are not the senior author, also obtain the senior author's approval.

Requirements to be followed when using an entire IEEE copyrighted paper in a thesis:

- 1) The following IEEE copyright/ credit notice should be placed prominently in the references: © [year of original publication] IEEE. Reprinted, with permission, from [author names, paper title, IEEE publication title, and month/year of publication]
- 2) Only the accepted version of an IEEE copyrighted paper can be used when posting the paper or your thesis on-line.
- 3) In placing the thesis on the author's university website, please display the following message in a prominent place on the website: In reference to IEEE copyrighted material which is used with permission in this thesis, the IEEE does not endorse any of [university/educational entity's name goes here]'s products or services. Internal or personal use of this material is permitted. If interested in reprinting/republishing IEEE copyrighted material for advertising or promotional purposes or for creating new collective works for resale or redistribution, please go to http://www.ieee.org/publications_standards/publications/rights/rights_link.html to learn how to obtain a License from RightsLink.

If applicable, University Microfilms and/or ProQuest Library, or the Archives of Canada may supply single copies of the dissertation.

BACK

CLOSE WINDOW

© 2021 Copyright - All Rights Reserved | Copyright Clearance Center, Inc. | Privacy statement | Terms and Conditions
Comments? We would like to hear from you. E-mail us at customer-care@copyright.com



Dynamic PET Image Reconstruction Using the Wavelet Kernel Method



Conference Proceedings:
2019 IEEE Nuclear Science Symposium and Medical Imaging Conference (NSS/MIC)

Author:
[;Zahra;] [;Ashouri;]; Chad R. Hunter; Benjamin A. Spencer; Guobao Wang; Richard M. Dansereau; Robert A. DeKemp

Publisher: IEEE

Date: 26 Oct.-2 Nov. 2019

Copyright © 2019, IEEE

Thesis / Dissertation Reuse

The IEEE does not require individuals working on a thesis to obtain a formal reuse license, however, you may print out this statement to be used as a permission grant:

Requirements to be followed when using any portion (e.g., figure, graph, table, or textual material) of an IEEE copyrighted paper in a thesis:

- 1) In the case of textual material (e.g., using short quotes or referring to the work within these papers) users must give full credit to the original source (author, paper, publication) followed by the IEEE copyright line © 2011 IEEE.
- 2) In the case of illustrations or tabular material, we require that the copyright line © [Year of original publication] IEEE appear prominently with each reprinted figure and/or table.
- 3) If a substantial portion of the original paper is to be used, and if you are not the senior author, also obtain the senior author's approval.

Requirements to be followed when using an entire IEEE copyrighted paper in a thesis:

- 1) The following IEEE copyright/ credit notice should be placed prominently in the references: © [year of original publication] IEEE. Reprinted, with permission, from [author names, paper title, IEEE publication title, and month/year of publication]
- 2) Only the accepted version of an IEEE copyrighted paper can be used when posting the paper or your thesis online.
- 3) In placing the thesis on the author's university website, please display the following message in a prominent place on the website: In reference to IEEE copyrighted material which is used with permission in this thesis, the IEEE does not endorse any of [university/educational entity's name goes here]'s products or services. Internal or personal use of this material is permitted. If interested in reprinting/republishing IEEE copyrighted material for advertising or promotional purposes or for creating new collective works for resale or redistribution, please go to http://www.ieee.org/publications_standards/publications/rights/rights_link.html to learn how to obtain a License from RightsLink.

If applicable, University Microfilms and/or ProQuest Library, or the Archives of Canada may supply single copies of the dissertation.

[BACK](#)

[CLOSE WINDOW](#)



Kernel-based Reconstruction of Cardiac PET Images Using MR Information



Conference Proceedings:

2020 IEEE Nuclear Science Symposium and Medical Imaging Conference (NSS/MIC)

Author:

[[:Zahra:]] [[:Ashouri:]] Chad R. Hunter; Benjamin A. Spencer; Guobao Wang; Richard M. Dansereau; Robert A. deKemp

Publisher: IEEE

Date: 31 Oct.-7 Nov. 2020

Copyright © 2020, IEEE

Thesis / Dissertation Reuse

The IEEE does not require individuals working on a thesis to obtain a formal reuse license, however, you may print out this statement to be used as a permission grant:

Requirements to be followed when using any portion (e.g., figure, graph, table, or textual material) of an IEEE copyrighted paper in a thesis:

- 1) In the case of textual material (e.g., using short quotes or referring to the work within these papers) users must give full credit to the original source (author, paper, publication) followed by the IEEE copyright line © 2011 IEEE.
- 2) In the case of illustrations or tabular material, we require that the copyright line © [Year of original publication] IEEE appear prominently with each reprinted figure and/or table.
- 3) If a substantial portion of the original paper is to be used, and if you are not the senior author, also obtain the senior author's approval.

Requirements to be followed when using an entire IEEE copyrighted paper in a thesis:

- 1) The following IEEE copyright/ credit notice should be placed prominently in the references: © [year of original publication] IEEE. Reprinted, with permission, from [author names, paper title, IEEE publication title, and month/year of publication]
- 2) Only the accepted version of an IEEE copyrighted paper can be used when posting the paper or your thesis online.
- 3) In placing the thesis on the author's university website, please display the following message in a prominent place on the website: In reference to IEEE copyrighted material which is used with permission in this thesis, the IEEE does not endorse any of [university/educational entity's name goes here]'s products or services. Internal or personal use of this material is permitted. If interested in reprinting/republishing IEEE copyrighted material for advertising or promotional purposes or for creating new collective works for resale or redistribution, please go to http://www.ieee.org/publications_standards/publications/rights/rights_link.html to learn how to obtain a License from RightsLink.

If applicable, University Microfilms and/or ProQuest Library, or the Archives of Canada may supply single copies of the dissertation.

[BACK](#)

[CLOSE WINDOW](#)



Evaluation of Wavelet Kernel-based PET Image Reconstruction

Author: [[:Zahra:]]; [[:Ashouri:]]; Guobao Wang; Richard M. Dansereau; Robert A. de Kemp

Publication: IEEE Transactions on Radiation and Plasma Medical Sciences

Publisher: IEEE

Date: Dec 31, 1969

Copyright © 1969, IEEE

Thesis / Dissertation Reuse

The IEEE does not require individuals working on a thesis to obtain a formal reuse license, however, you may print out this statement to be used as a permission grant:

Requirements to be followed when using any portion (e.g., figure, graph, table, or textual material) of an IEEE copyrighted paper in a thesis:

- 1) In the case of textual material (e.g., using short quotes or referring to the work within these papers) users must give full credit to the original source (author, paper, publication) followed by the IEEE copyright line © 2011 IEEE.
- 2) In the case of illustrations or tabular material, we require that the copyright line © [Year of original publication] IEEE appear prominently with each reprinted figure and/or table.
- 3) If a substantial portion of the original paper is to be used, and if you are not the senior author, also obtain the senior author's approval.

Requirements to be followed when using an entire IEEE copyrighted paper in a thesis:

- 1) The following IEEE copyright/ credit notice should be placed prominently in the references: © [year of original publication] IEEE. Reprinted, with permission, from [author names, paper title, IEEE publication title, and month/year of publication]
- 2) Only the accepted version of an IEEE copyrighted paper can be used when posting the paper or your thesis online.
- 3) In placing the thesis on the author's university website, please display the following message in a prominent place on the website: In reference to IEEE copyrighted material which is used with permission in this thesis, the IEEE does not endorse any of [university/educational entity's name goes here]'s products or services. Internal or personal use of this material is permitted. If interested in reprinting/republishing IEEE copyrighted material for advertising or promotional purposes or for creating new collective works for resale or redistribution, please go to http://www.ieee.org/publications_standards/publications/rights/rights_link.html to learn how to obtain a License from RightsLink.

If applicable, University Microfilms and/or ProQuest Library, or the Archives of Canada may supply single copies of the dissertation.

[BACK](#)

[CLOSE WINDOW](#)

Appendix D - Research ethics board approvals



Ottawa Health Science Network Research Ethics Board/ Conseil d'éthique de la recherche du Réseau de science de la santé d'Ottawa

Civic Box 411 725 Parkdale Avenue, Ottawa, Ontario K1Y 4E9 613-796-5555 ext. 14902 Fax : 613-761-4311
<http://www.ohri.ca/ohsn-reb>

September 23, 2014

Dr. Pablo Nery
University of Ottawa Heart Institute
Division of Cardiology
40 Ruskin Street, Room H123
Ottawa, ON K1Y 4W7

Dear Dr. Nery:

Re: Protocol # 20140417-01H Correlation of Arrhythmia Mechanism and Substrate to Ablate Persistent Atrial Fibrillation (COAST-AF): A Pilot Study

Protocol approval valid until - November 23, 2014

This protocol was reviewed by the full Board of the Ottawa Health Science Network Research Ethics Board (OHSN-REB) at the June 18, 2014 meeting. You have met the requirements of the OHSN-REB and your protocol has been granted CONDITIONAL approval.

No changes, amendments or addenda may be made to the protocol or the consent form without the OHSN-REB's review and approval.

NOTE: IF YOUR STUDY REQUIRES A CONTRACT/AGREEMENT, YOU MAY NOT START THE STUDY, OR BEGIN TO RECRUIT RESEARCH PARTICIPANTS INTO THE STUDY UNTIL THE CONTRACT/AGREEMENT HAS BEEN REVIEWED BY THE UNIVERSITY OF OTTAWA HEART INSTITUTE CONTRACTS OFFICE AND HAS BEEN SIGNED BY THE AUTHORIZED SIGNATORIES. FOR FURTHER DETAILS, PLEASE CONTACT AISHA WEAVER, CONTRACTS ASSOCIATE AT aweaver@ottawaheart.ca OR AT 613-761-4885.

Conditional REB approval has been granted for the following:

- Research Protocol version June 3, dated June 3, 2014
- English Informed Consent, Version 1, dated September 11, 2014
- Case Report forms

Recruitment of English-speaking participants is contingent on REB receipt of the the Health Canada approval letter for basic research.

Upon receipt and review of the French consent forms, the protocol approval may be extended to June 17, 2015 (one year from the initial meeting date), and the recruitment of French-speaking participants may commence. When submitting hardcopies of the French documentation to the OHSN-REB please be sure to indicate how the document was translated. Refer to SOP # 1000 for the translation options when submitting your French documents to the REB for approval. The SOP can be found in the Translation section of the OHSN-REB website (www.ohri.ca/OHSN-REB).

If the study is to continue beyond the expiry date noted above, a Renewal Form should be submitted to the REB approximately six weeks prior to the current expiry date. If the study has been completed by this date, a Termination Report should be submitted.2

The Ottawa Health Science Network Research Ethics Board (OHSN-REB) was created by the merger of both the Ottawa Hospital Research Ethics Board (OHREB) and the Human Research Ethics Board (HREB) for meetings held at the University of Ottawa Heart Institute.

OHSN-REB complies with the membership requirements and operates in compliance with the Tri-Council Policy Statement: Ethical Conduct for Research Involving Humans; the International Conference on Harmonization - Good Clinical Practice: Consolidated Guideline; the provisions of the Personal Health Information Protection Act 2004; and the Food and Drug Act of Health Canada and its applicable Regulations.

The OHSN-REB has reviewed and approved the clinical trial protocol and informed consent form for the trial which is to be conducted by the qualified investigator named above at the specified clinical trial site. This approval and the views of this Research Ethics Board have been documented in writing.

Yours sincerely,

A handwritten signature in black ink, appearing to read "J. Robblee".

Jim Robblee, M.D.
Vice-Chairperson
Ottawa Health Science Network Research Ethics Board

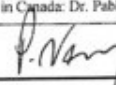
JR/dw

Appendix 1 – Application for Authorization and Attestation for Positron-emitting Radiopharmaceuticals (PERs) Basic Clinical Research Study

PART 1 – General Information			
A) Sponsor			
Name of sponsor University of Ottawa Heart Institute	E-mail lgarrard@ottawaheart.ca		
Civic address 40 Ruskin Street, Ottawa, Ontario, K1Y 4W7			
Postal address (if different)			
Telephone No. 613-761-4192	Fax No. 613-761-5406		
B) Manufacturer or in the case of an application for importation, the manufacturer's representative in Canada who is responsible for the sale of the study drug			
Name of manufacturer University of Ottawa Heart Institute	E-mail lgarrard@ottawaheart.ca		
Civic address 40 Ruskin Street, Ottawa, Ontario, K1Y 4W7			
Postal address (if different)			
Telephone No. 613-761-4192	Fax No. 613-761-5406		
C) Related Submissions*			
Type NOL	Control No. # 098578	File No. #9427-U0143-35C	Date Cleared June 10, 2005
Brand Name: [¹¹ C]-(1R,2S)-(-)- <i>meta</i> -3-hydroxy- α -[1-(methylamino)ethyl]-benzenemethanol; [¹¹ C] <i>meta</i> -Hydroxyephedrine; [¹¹ C] <i>m</i> HED		Manufacturer/Sponsor Name University of Ottawa Heart Institute	
Associated Submission(s)			
Reason for Submission			
New Protocol and application			
* Attach separate sheets if necessary (same format) if necessary. Number of pages attached: _____			
PART 2 – Application and Information Requirements			
Title of the basic clinical research study and the protocol code or identification	Correlation of Arrhythmia Mechanism and Substrate to Ablate Persistent Atrial Fibrillation (COAST-AF)		
Purposes and concise description of study - Please attach a 1-2 page summary. - Ensure that an explanation is provided as to how the criteria for basic clinical research (as outlined herein) have been met.	X Summary attached		

Number of study subjects	30
Brand name, if any, of positron-emitting radiopharmaceutical(s)	[¹¹ C]-(1R,2S)-(-)- <i>meta</i> -3-hydroxy-α-[1-(methylamino)ethyl]-benzenemethanol; [¹¹ C] <i>meta</i> -Hydroxyephedrine; [¹¹ C]mHED
Chemical or generic name of the active ingredients in the study drug	[¹¹ C]-(1R,2S)-(-)- <i>meta</i> -3-hydroxy-α-[1-(methylamino)ethyl]-benzenemethanol
Qualitative list of the non-active ingredients of the study drug	Sterile Water: 5.5 mL Sodium Chloride: 31.5 mg in 3.5 mL sterile water Sodium Bicarbonate: 8.4 mg in 1 mL sterile water Total Batch size: 10.0 mL
Maximum mass to be administered	N/A mass is not measured
Radioactive dose range of the study drug, expressed in MBq or mCi	333-370 MBq (9-10 mCi) / patient or 5 MBq /kg of patient
Effective dose or effective dose equivalent of the study drug, expressed in mSv/MBq or rem/mCi	0.0054 mSv/MBq

PART 3 – Attestation (NOTE: if any box is checked “No”, a CTA should be filed)		
	YES	NO
1. The purpose of the study is to a) obtain data on the pharmacokinetics or metabolism of the study drug; b) normal human biochemistry or physiology; or c) changes caused to human biochemistry or physiology by aging, disease or medical interventions.	x	<input type="checkbox"/>
2. The study is NOT primarily intended to a) discover, identify or verify the pharmacodynamic effects of the study drug; b) identify adverse reactions; c) fulfil an immediate therapeutic or diagnostic purpose; or d) ascertain the safety or efficacy of the study drug.	x	<input type="checkbox"/>
3. There is sufficient data from testing the study drug in animals and humans to demonstrate its safety in humans.	x	<input type="checkbox"/>
4. The amount of active ingredients or combination of active ingredients in the study drug has been shown not to cause any clinically detectable pharmacodynamic effect in humans.	x	<input type="checkbox"/>
5. The total radiation dose incurred annually by a study subject, including from multiple administrations of the study drug, from significant contaminants or from impurities and from the use of other procedures for the purposes of the study, will be not more than 50 mSv.	x	<input type="checkbox"/>
6. All concurrent medications (other than the PER) used in this study have been granted market authorization by Health Canada.	x	<input type="checkbox"/>
7. Subjects are over 18 years old and have legal capacity at the time of the study.	x	<input type="checkbox"/>
8. Confirm that female subjects are not pregnant (as confirmed by a pregnancy test or signed declaration) and/or are to suspend lactation for 24 hours after the administration of the study drug.	x	<input type="checkbox"/>

9. The total number of subjects in this study is equal to or less than 30 individuals. ***If the study includes more than 30 individuals, a scientific rationale has been provided to the Minister.	x	<input type="checkbox"/>						
10. All criteria for a basic clinical research study as set out in subsection C.03.307 (1) of the <i>Food and Drug Regulations</i> have been met.	x	<input type="checkbox"/>						
11. The starting date for each study site has been provided. Please note that if the date is not known at this time, the sponsor shall notify the Minister in writing of the day on which the sale or importation of the study drug is intended to start in respect of each study site, not later than 15 days before that day.	x	<input type="checkbox"/>						
12. A research ethics board has approved the study proposed within this submission, and the approval letter is enclosed. (Please see attached REB attestation form)	x	<input type="checkbox"/>						
13. A list of any previous applications for studies related to the current study has been provided.	x	<input type="checkbox"/>						
14. The study will be conducted in accordance with all applicable Regulations.	x	<input type="checkbox"/>						
15. All information contained or referred to in the application is complete and accurate and is not false or misleading.	x	<input type="checkbox"/>						
16. All requirements for clinical information, as outlined in this template and within section C.03.307 of the <i>Food and Drug Regulations</i> have been met.	x	<input type="checkbox"/>						
17. All requirements for quality information and data, as outlined in this template and within section C.03.311 of the <i>Food and Drug Regulations</i> have been met.	x	<input type="checkbox"/>						
18. Subjects in the study will be monitored according to pre-determined procedures, and any serious adverse reaction attributable to the use of the PER should be reported to Health Canada within the prescribed time frames.	x	<input type="checkbox"/>						
Sponsor's Senior Medical Officer or Scientific Officer in Canada: Dr. Pablo Nery		Telephone Number: 613-761-4914						
Signature: 	Date:	<table border="1"> <thead> <tr> <th>Day</th> <th>Month</th> <th>Year</th> </tr> </thead> <tbody> <tr> <td>2</td> <td>1</td> <td>05</td> </tr> </tbody> </table>	Day	Month	Year	2	1	05
Day	Month	Year						
2	1	05						
Sponsor's Senior Executive Officer (if different than above): Dr. Peter Liu		Telephone Number: 613-761-9544						
Signature: 	Date:	<table border="1"> <thead> <tr> <th>Day</th> <th>Month</th> <th>Year</th> </tr> </thead> <tbody> <tr> <td>27</td> <td>05</td> <td>17</td> </tr> </tbody> </table>	Day	Month	Year	27	05	17
Day	Month	Year						
27	05	17						

Appendix 2 – Study Site Information and Research Ethics Board Attestation

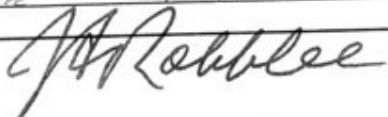
An attestation must be completed by the Research Ethics Board that reviewed and approved the basic research study protocol and informed consent form for the study at the site specified below. The completed attestation must be retained by the study sponsor for a period of 5 years after the day on which the study ends.

PART 1 – Basic Research Study Protocol Information				
Type of change (if applicable): <input type="checkbox"/> Change in Sponsor Information (complete Part 2) <input type="checkbox"/> Change/Addition of a New Site (complete Part 3) <input type="checkbox"/> Change/Addition of a Study Start Date (complete Part 3A) <input type="checkbox"/> Change in Qualified Investigator (Name of Previous Investigator: _____) (complete Part 3B) <input type="checkbox"/> Change to the Research Ethics Board (complete Part 3C) <input checked="" type="checkbox"/> Other (please specify): New protocol and application				
Basic Research Study Protocol Title Correlation of Arrhythmia Mechanism and Substrate to Ablate Persistent Atrial Fibrillation (COAST-AF)				Basic Research Study Protocol Number (if applicable)
PART 2 – Drug Product / Sponsor Information				
A) Drug Product Information				
Brand Name : [¹¹ C]-(1R,2S)-(-)- <i>meta</i> -3-hydroxy- α -[1-(methylamino)ethyl]-benzenemethanol; [¹¹ C] <i>meta</i> -Hydroxyephedrine; [¹¹ C] <i>m</i> HED				
Proper or Common Name [¹¹ C] <i>m</i> HED				
B) Sponsor of the Basic Research Study				
Company Name (Full Name - No Abbreviations) University of Ottawa Heart Institute				
Street / Suite / PO Box 40 Ruskin Street	City / Town Ottawa	Prov. / State Ontario	Country Canada	Postal/ZIP Code K1Y 4W7
C) Contact for this Basic Research Study				
Contact Name Linda Garrard			E-mail lgarrard@ottawaheart.ca	
Company Name (Full Name - No Abbreviations) University of Ottawa Heart Institute				
Street / Suite / PO Box 40 Ruskin Street	City / Town Ottawa	Prov. / State Ontario	Country Canada	
Telephone No. 613-761-4192	Fax No. 613-761-5406		Postal/ZIP Code K1Y 4W7	

PART 3 – Basic Research Study Site Information			
A) Basic Research Study Site			
Name of Site (Full Name - No Abbreviations) University of Ottawa Heart Institute			
Street / Suite / PO Box 40 Ruskin Street	City / Town Ottawa	Province Ontario	Postal Code K1Y 4W7
Start Date of the Basic Research Study (day / month / year) : TBD ____/____/____			
B) Qualified Investigator			
Name Dr. Pablo Nery	Title Associate Professor of Medicine, Staff Cardiologist		Language Preferred <input checked="" type="checkbox"/> English <input type="checkbox"/> French
Street / Suite / PO Box 40 Ruskin Street	City / Town Ottawa	Province Ontario	Postal Code K1Y 4W7
E-mail pnery@ottawaheart.ca	Tel. No. 613-761-4914	Fax No. 613-761-4407	
C) Research Ethics Board Approval*			
Name of Research Ethics Board Ottawa Health Science Network Research Ethics Board		Date of Approval <i>September 23, 2014</i>	
Street / Suite / PO Box 725 Parkdale Ave, Civic Box 411, LOEB Building,	City / Town Ottawa	Province Ontario	Postal Code K1Y 4E9
Name of Research Ethics Board Chair Dr. James Robblee	Telephone No. 613-798-5555 ext 16719.	Fax No. 613-761-4311	Language Preferred <input checked="" type="checkbox"/> English <input type="checkbox"/> French
Title MD, Vice Chairperson of OHSN-REB Board		E-mail readministration@toh.ca	
* Attach separate sheets if necessary (same format) for each Basic Research Study Site. Number of pages attached:			

In respect of the identified basic research study, as a representative of this Research Ethics Board, I certify that:

1. The membership of this Research Ethics Board complies with the membership requirements for Research Ethics Boards defined in C.03.306 of the *Food and Drug Regulations*;
2. This Research Ethics Board carries out its functions in a manner consistent with Good Clinical Practices; and
3. This Research Ethics Board has reviewed and approved the basic research study protocol and informed consent form for the study which is to be conducted by the qualified investigator named above at the specified basic research study site. This approval and the views of this Research Ethics Board have been documented in writing.

Name, Title and Signature of Research Ethics Board Representative		Date		
Name:	Title:	Day	Month	Year
<i>Dr. Robblee</i>	<i>Vice Chairman OHSN-REB</i>	<i>23</i>	<i>09</i>	<i>14</i>
Signature: 				



Office of Research Ethics
4500 ARISE Building | 1125 Colonel By Drive
Ottawa, Ontario K1S 5B6
613-520-2600 Ext: 4085
ethics@carleton.ca

CERTIFICATION OF INSTITUTIONAL ETHICS CLEARANCE

The following research has been granted clearance by the Carleton University Research Ethics Board-B (CUREB-B). CUREB-B is constituted and operates in compliance with the Tri-Council Policy Statement: Ethical Conduct for Research Involving Humans (TCPS2).

Ethics Clearance ID: Project # 116753

Project Team Members: Zahra Ashouri Talouki (Primary Investigator)

Richard Dansereau (Co-Investigator)

Robert deKemp (Research Supervisor)

Study Title: PET image reconstruction using dynamic PET series and MR information

Funding Source: (If applicable):

Effective: December 17, 2021

Expires: December 31, 2022

This certification is subject to the following conditions:

1. Clearance is granted only for the research and purposes described in the application.
2. Any modification to the approved research must be submitted to CUREB-B via a Change to Protocol Form. All changes must be cleared prior to the continuance of the research.
3. An Annual Status Report for the renewal or closure of ethics clearance must be submitted and cleared by the renewal date listed above. Failure to submit the Annual Status Report will result in the closure of the file. If funding is associated, funds will be frozen.
4. During the course of the study, if you encounter an adverse event, material incidental finding, protocol deviation or other unanticipated problem, you must complete and submit a Report of Adverse Events and Unanticipated Problems Form.
5. It is the responsibility of the student to notify their supervisor of any adverse events, changes to their application, or requests to renew/close the protocol.
6. Failure to conduct the research in accordance with the principles of the *Tri-Council Policy Statement: Ethical Conduct for Research Involving Humans 2nd edition* and the *Carleton University Policies and Procedures for the Ethical Conduct of Research* may result in the suspension or termination of the research project.

IMPORTANT: Special requirements for COVID-19:

If this study involves **in-person research interactions with human participants**, whether on- or off-campus, the following rules apply:

1. Upon receiving clearance from CUREB, please seek the approval of the relevant Dean for your research. Provide a copy of your CUREB clearance to the Dean for their records. See Principles and Procedures for On-campus Research at Carleton University and note that this document applies both to on- and off-campus research that involves human participants. Please contact your Dean's Office for more information about obtaining their approval.
2. Provide a copy of the Dean's approval to the Office of Research Ethics prior to starting any in-person research activities.
3. If the Dean's approval requires any significant change(s) to any element of the study, you must notify the Office of Research Ethics of such change(s).

Upon reasonable request, it is the policy of CUREB, for cleared protocols, to release the name of the PI, the title of the project, and the date of clearance and any renewal(s).

Please email the Research Compliance Coordinators at ethics@carleton.ca if you have any questions.

CLEARED BY:

Date: December 17, 2021



Bernadette Campbell, PhD, Chair, CUREB-B



Kathryne Dupre, PhD, Co-Chair, CUREB-B

References

- [1] R. Klein *et al.*, “Intra- and inter-operator repeatability of myocardial blood flow and myocardial flow reserve measurements using rubidium-82 pet and a highly automated analysis program,” *J. Nucl. Cardiol. Off. Publ. Am. Soc. Nucl. Cardiol.*, vol. 17, no. 4, pp. 600–616, Aug. 2010, doi: 10.1007/s12350-010-9225-3.
- [2] S. Klein, M. Staring, K. Murphy, M. A. Viergever, and J. P. W. Pluim, “Elastix: A toolbox for intensity-based medical image registration,” *IEEE Trans. Med. Imaging*, vol. 29, no. 1, pp. 196–205, Jan. 2010, doi: 10.1109/TMI.2009.2035616.
- [3] J. Qi and R. M. Leahy, “Iterative reconstruction techniques in emission computed tomography,” *Phys. Med. Biol.*, vol. 51, no. 15, pp. R541–578, Aug. 2006, doi: 10.1088/0031-9155/51/15/R01.
- [4] G. Gindi, M. Lee, A. Rangarajan, and I. G. Zubal, “Bayesian reconstruction of functional images using anatomical information as priors,” *IEEE Trans. Med. Imaging*, vol. 12, no. 4, pp. 670–680, Dec. 1993, doi: 10.1109/42.251117.
- [5] B. A. Ardekani, M. Braun, B. F. Hutton, I. Kanno, and H. Iida, “Minimum cross-entropy reconstruction of PET images using prior anatomical information,” *Phys. Med. Biol.*, vol. 41, no. 11, pp. 2497–2517, Nov. 1996, doi: 10.1088/0031-9155/41/11/018.
- [6] C. Comtat, P. E. Kinahan, M. Defrise, C. Michel, C. Lartzien, and D. W. Townsend, “Simulating whole-body PET scanning with rapid analytical methods,” in *IEEE Nuclear Science Symposium and Medical Imaging Conference*, Oct. 1999, vol. 3, pp. 1260–1264. doi: 10.1109/NSSMIC.1999.842786.
- [7] J. Nuyts, “The use of mutual information and joint entropy for anatomical priors in emission tomography,” in *2007 IEEE Nuclear Science Symposium Conference Record*, Oct. 2007, vol. 6, pp. 4149–4154. doi: 10.1109/NSSMIC.2007.4437034.
- [8] W. Hutchcroft, G. Wang, K. T. Chen, C. Catana, and J. Qi, “Anatomically-aided PET reconstruction using the kernel method,” *Phys. Med. Biol.*, vol. 61, no. 18, pp. 6668–6683, 21 2016, doi: 10.1088/0031-9155/61/18/6668.
- [9] G. Wang and J. Qi, “PET image reconstruction using kernel method,” *IEEE Trans. Med. Imaging*, vol. 34, no. 1, pp. 61–71, Jan. 2015, doi: 10.1109/TMI.2014.2343916.
- [10] D. L. Bailey, D. W. Townsend, P. E. Valk, and M. N. Maisey, *Positron Emission Tomography: Basic Sciences*. Springer Science & Business Media, 2005.
- [11] M. Politis and P. Piccini, “Positron emission tomography imaging in neurological disorders,” *J. Neurol.*, vol. 259, no. 9, pp. 1769–1780, Sep. 2012, doi: 10.1007/s00415-012-6428-3.
- [12] T.-P. Mm, M. Na, F. Dc, M. J, and S. Dl, “Photon time-of-flight-assisted positron emission tomography.,” *J. Comput. Assist. Tomogr.*, vol. 5, no. 2, pp. 227–239, Apr. 1981, doi: 10.1097/00004728-198104000-00014.
- [13] E. D. Ponti *et al.*, “Performance measurements for the PET/CT Discovery-600 using NEMA NU 2-2007 standards,” *Med. Phys.*, vol. 38, no. 2, pp. 968–974, 2011, doi: 10.1118/1.3544655.
- [14] J. S. Suri, *Handbook of Biomedical Image Analysis - Volume 1: Segmentation Models Part A* | David Wilson | Springer.

- [15] F. H. Fahey, "Data acquisition in PET imaging," *J. Nucl. Med. Technol.*, vol. 30, no. 2, pp. 39–49, Jun. 2002.
- [16] C. S. Levin, M. Dahlbom, and E. J. Hoffman, "A Monte Carlo correction for the effect of Compton scattering in 3-D PET brain imaging," *IEEE Trans. Nucl. Sci.*, vol. 42, no. 4, pp. 1181–1185, Aug. 1995, doi: 10.1109/23.467880.
- [17] D. W. Townsend *et al.*, "Fully three-dimensional reconstruction for a PET camera with retractable septa," *IEEE Trans. Med. Imaging*, vol. 10, no. 4, pp. 505–512, 1991, doi: 10.1109/42.108584.
- [18] S. Grootoank, T. J. Spinks, T. Jones, C. Michel, and A. Bol, "Correction for scatter using a dual energy window technique with a tomograph operated without septa," in *IEEE Nuclear Science Symposium and Medical Imaging Conference Record*, Nov. 1991, vol. 3, pp. 1569–1573. doi: 10.1109/NSSMIC.1991.259177.
- [19] D. L. Bailey, "3D acquisition and reconstruction in positron emission tomography," *Ann. Nucl. Med.*, vol. 6, no. 3, pp. 123–130, Sep. 1992, doi: 10.1007/BF03178303.
- [20] S. R. Cherry, S. R. Meikle, and E. J. Hoffman, "Correction and characterization of scattered events in three-dimensional PET using scanners with retractable septa," *J. Nucl. Med. Off. Publ. Soc. Nucl. Med.*, vol. 34, no. 4, pp. 671–678, Apr. 1993.
- [21] P. E. Kinahan, D. W. Townsend, T. Beyer, and D. Sashin, "Attenuation correction for a combined 3D PET/CT scanner," *Med. Phys.*, vol. 25, no. 10, pp. 2046–2053, Oct. 1998, doi: 10.1118/1.598392.
- [22] R. N. Bracewell, "Strip integration in radio astronomy," *Aust. J. Phys.*, vol. 9, no. 2, pp. 198–217, 1956, doi: 10.1071/ph560198.
- [23] J. Radon, "On the determination of functions from their integral values along certain manifolds," *IEEE Trans. Med. Imaging*, vol. 5, no. 4, pp. 170–176, Dec. 1986, doi: 10.1109/TMI.1986.4307775.
- [24] J. L. Prince and J. Links, *Medical Imaging Signals and Systems | 2nd edition* | Pearson. Upper Saddle River, N.J. : Pearson Prentice Hall, 2006.
- [25] L. A. Shepp and Y. Vardi, "Maximum likelihood reconstruction for emission tomography," *IEEE Trans. Med. Imaging*, vol. 1, no. 2, pp. 113–122, 1982, doi: 10.1109/TMI.1982.4307558.
- [26] R. A. Horn and C. R. Johnson, *Matrix Analysis*. Cambridge: Cambridge University Press, 1985. doi: 10.1017/CBO9780511810817.
- [27] J. A. Fessler and W. L. Rogers, "Spatial resolution properties of penalized-likelihood image reconstruction: space-invariant tomographs," *IEEE Trans. Image Process.*, vol. 5, no. 9, pp. 1346–1358, Sep. 1996, doi: 10.1109/83.535846.
- [28] E. Levitan and G. T. Herman, "A Maximum a Posteriori probability expectation maximization algorithm for image reconstruction in emission tomography," *IEEE Trans. Med. Imaging*, vol. 6, no. 3, pp. 185–192, Sep. 1987, doi: 10.1109/TMI.1987.4307826.
- [29] T. J. Hebert and R. Leahy, "Statistic-based MAP image-reconstruction from Poisson data using Gibbs priors," *IEEE Trans. Signal Process.*, vol. 40, no. 9, pp. 2290–2303, Sep. 1992, doi: 10.1109/78.157228.
- [30] H. M. Hudson and R. S. Larkin, "Accelerated image reconstruction using ordered subsets of projection data," *IEEE Trans. Med. Imaging*, vol. 13, no. 4, pp. 601–609, 1994, doi: 10.1109/42.363108.

- [31] M. Muzi *et al.*, “Quantitative assessment of dynamic PET imaging data in cancer imaging,” *Magn. Reson. Imaging*, vol. 30, no. 9, pp. 1203–1215, Nov. 2012, doi: 10.1016/j.mri.2012.05.008.
- [32] C. Hunter, “A study of the prevalence of patient body motion and its subsequent correction by projection consistency conditions,” PhD thesis, Carleton University, Ottawa, 2017.
- [33] E. D. Morris, C. J. Endres, K. C. Schmidt, B. T. Christian, R. F. Muzic, and R. E. Fisher, “Chapter 23 - kinetic modeling in positron emission tomography,” in *Emission Tomography*, M. N. Wernick and J. N. Aarsvold, Eds. San Diego: Academic Press, 2004, pp. 499–540. doi: 10.1016/B978-012744482-6.50026-0.
- [34] J. Llacer, E. Veklerov, K. J. Coakley, E. J. Hoffman, and J. Nunez, “Statistical analysis of maximum likelihood estimator images of human brain FDG PET studies,” *IEEE Trans. Med. Imaging*, vol. 12, no. 2, pp. 215–231, Jun. 1993, doi: 10.1109/42.232250.
- [35] B. W. Silverman, M. C. Jones, J. D. Wilson, and D. W. Nychka, “A smoothed EM approach to indirect estimation problems, with particular, reference to stereology and emission tomography,” *J. R. Stat. Soc. Ser. B Methodol.*, vol. 52, no. 2, pp. 271–324, 1990.
- [36] J. A. Fessler, “Mean and variance of implicitly defined biased estimators (such as penalized maximum likelihood): applications to tomography,” *IEEE Trans. Image Process.*, vol. 5, no. 3, pp. 493–506, Mar. 1996, doi: 10.1109/83.491322.
- [37] J. A. Fessler, N. H. Clinthorne, and W. L. Rogers, “Regularized emission image reconstruction using imperfect side information,” *IEEE Trans. Nucl. Sci.*, vol. 39, no. 5, pp. 1464–1471, Oct. 1992, doi: 10.1109/23.173225.
- [38] A. M. Alessio and P. E. Kinahan, “Improved quantitation for PET/CT image reconstruction with system modeling and anatomical priors,” *Med. Phys.*, vol. 33, no. 11, pp. 4095–4103, 2006, doi: 10.1118/1.2358198.
- [39] V.-G. Nguyen and S.-J. Lee, “Incorporating anatomical side information into PET reconstruction using nonlocal regularization,” *IEEE Trans. Image Process.*, vol. 22, no. 10, pp. 3961–3973, Oct. 2013, doi: 10.1109/TIP.2013.2265881.
- [40] A. O. Hero, R. Piramuthu, J. A. Fessler, and S. R. Titus, “Minimax emission computed tomography using high-resolution anatomical side information and B-spline models,” *IEEE Trans. Inf. Theory*, vol. 45, no. 3, pp. 920–938, Apr. 1999, doi: 10.1109/18.761333.
- [41] F. Bataille, C. Comtat, S. Jan, F. C. Sureau, and R. Trebossen, “Brain PET partial-volume compensation using blurred anatomical labels,” in *IEEE Nuclear Science Symposium Conference Record*, Oct. 2006, vol. 3, pp. 1817–1824. doi: 10.1109/NSSMIC.2006.354247.
- [42] A. Rangarajan and I.-T. Hsiao, “A bayesian joint mixture framework for the integration of anatomical information in functional image reconstruction,” p. 19.
- [43] R. Loeb, N. Navab, and S. I. Ziegler, “Direct parametric reconstruction using anatomical regularization for simultaneous PET/MRI data,” *IEEE Trans. Med. Imaging*, vol. 34, no. 11, pp. 2233–2247, Nov. 2015, doi: 10.1109/TMI.2015.2427777.
- [44] J. Tang and A. Rahmim, “Anatomy assisted MAP-EM PET image reconstruction incorporating joint entropies of wavelet subband image pairs,” in *IEEE Nuclear*

- Science Symposium Conference Record*, Oct. 2009, pp. 3741–3745. doi: 10.1109/NSSMIC.2009.5401877.
- [45] R. Leahy and X. Yan, “Incorporation of anatomical MR data for improved functional imaging with PET,” in *Information Processing in Medical Imaging*, Berlin, Heidelberg, 1991, pp. 105–120. doi: 10.1007/BFb0033746.
- [46] J. E. Bowsher *et al.*, “Utilizing MRI information to estimate F18-FDG distributions in rat flank tumors,” in *IEEE Symposium Conference Record Nuclear Science 2004.*, Oct. 2004, vol. 4, pp. 2488–2492. doi: 10.1109/NSSMIC.2004.1462760.
- [47] G.-H. Chen, J. Tang, and S. Leng, “Prior image constrained compressed sensing (PICCS): a method to accurately reconstruct dynamic CT images from highly undersampled projection data sets,” *Med. Phys.*, vol. 35, no. 2, pp. 660–663, Feb. 2008, doi: 10.1118/1.2836423.
- [48] G. Wang, C. Catana, and J. Qi, “Joint reconstruction of attenuation and emission from PET data using MR-derived attenuation prior,” presented at the IEEE Nuclear Science Symposium and Medical Imaging Conference, Anaheim, CA, USA., Nov. 2012.
- [49] C. Chan, S. Meikle, R. Fulton, G.-J. Tian, W. Cai, and D. D. Feng, “A non-local post-filtering algorithm for PET incorporating anatomical knowledge,” in *IEEE Nuclear Science Symposium Conference Record*, Oct. 2009, pp. 2728–2732. doi: 10.1109/NSSMIC.2009.5401971.
- [50] K. Gong, C. Catana, J. Qi, and Q. Li, “PET image reconstruction using deep image prior,” *IEEE Trans. Med. Imaging*, vol. 38, no. 7, pp. 1655–1665, Jul. 2019, doi: 10.1109/TMI.2018.2888491.
- [51] P. Novosad and A. J. Reader, “MR-guided dynamic PET reconstruction with the kernel method and spectral temporal basis functions,” *Phys. Med. Biol.*, vol. 61, no. 12, pp. 4624–4644, 21 2016, doi: 10.1088/0031-9155/61/12/4624.
- [52] B. Spencer, J. Qi, R. D. Badawi, and G. Wang, “Dynamic PET image reconstruction for parametric imaging using the HYPR kernel method,” in *Medical Imaging 2017: Physics of Medical Imaging*, Mar. 2017, vol. 10132, p. 101324W. doi: 10.1117/12.2254497.
- [53] H.-M. Huang, “Dynamic PET reconstruction using the kernel method with non-local means denoising,” *Biomed. Signal Process. Control*, vol. 68, p. 102673, Jul. 2021, doi: 10.1016/j.bspc.2021.102673.
- [54] G. Wang, “High temporal-resolution dynamic PET image reconstruction using a new spatiotemporal kernel method,” *IEEE Trans. Med. Imaging*, vol. 38, no. 3, pp. 664–674, Mar. 2019, doi: 10.1109/TMI.2018.2869868.
- [55] K. Gong, G. Wang, K. T. Chen, C. Catana, and J. Qi, “Nonlinear PET parametric image reconstruction with MRI information using kernel method,” in *Medical Imaging 2017: Physics of Medical Imaging*, Mar. 2017, vol. 10132, p. 101321G. doi: 10.1117/12.2254273.
- [56] J. Bland *et al.*, “MR-guided kernel EM reconstruction for reduced dose PET imaging,” *IEEE Trans. Radiat. Plasma Med. Sci.*, vol. 2, no. 3, pp. 235–243, May 2018, doi: 10.1109/TRPMS.2017.2771490.
- [57] J. Bland, M. A. Belzunce, S. Ellis, C. J. McGinnity, A. Hammers, and A. J. Reader, “Spatially compact MR-guided kernel EM for PET image reconstruction,” *IEEE*

- Trans. Radiat. Plasma Med. Sci.*, vol. 2, no. 5, pp. 470–482, Sep. 2018, doi: 10.1109/TRPMS.2018.2844559.
- [58] K. Gong, J. Cheng-Liao, G. Wang, K. T. Chen, C. Catana, and J. Qi, “Direct patlak reconstruction from dynamic PET data using the kernel method with MRI information based on structural similarity,” *IEEE Trans. Med. Imaging*, vol. 37, no. 4, pp. 955–965, Apr. 2018, doi: 10.1109/TMI.2017.2776324.
- [59] J. H. Friedman, J. L. Bentley, and R. A. Finkel, “An algorithm for finding best matches in logarithmic expected time,” *ACM Trans. Math. Softw.*, vol. 3, no. 3, pp. 209–226, Sep. 1977, doi: 10.1145/355744.355745.
- [60] Z. Ashouri, C. R. Hunter, B. A. Spencer, G. Wang, R. M. Dansereau, and R. A. deKemp, “Kernel-based reconstruction of C-11-Hydroxyephedrine cardiac PET images of the sympathetic nervous system,” in *41st Annual International Conference of the IEEE Engineering in Medicine and Biology Society (EMBC)*, Jul. 2019, pp. 832–835. doi: 10.1109/EMBC.2019.8856752.
- [61] J. Mercer, “Functions of Positive and Negative Type, and their Connection with the Theory of Integral Equations,” *Philos. Trans. R. Soc. Lond. Ser. Contain. Pap. Math. Phys. Character*, vol. 209, pp. 415–446, 1909.
- [62] S. Xie, A. T. Lawniczak, S. Krishnan, and P. Lio, “Wavelet kernel principal component analysis in noisy multiscale data classification,” *ISRN Comput. Math.*, vol. 2012, Jul. 2012, doi: 10.5402/2012/197352.
- [63] L. Zhang, W. Zhou, L. Jiao, and S. Member, “Wavelet support vector machine,” *IEEE Trans. Syst. Man Cybern. B*, pp. 34–39, 2004.
- [64] H. Ryan, “Ricker, Ormsby; Klander, Butterworth - a choice of wavelets:,” *CSEG Rec.*, vol. 8–9, 1994.
- [65] A. Bernardino and J. Santos-Victor, “A real-time gabor primal sketch for visual attention,” in *Pattern Recognition and Image Analysis*, vol. 3522, J. S. Marques, N. Pérez de la Blanca, and P. Pina, Eds. Berlin, Heidelberg: Springer Berlin Heidelberg, 2005, pp. 335–342. doi: 10.1007/11492429_41.
- [66] Y. Meyer, *Ondelettes et opérateurs*. Paris: Hermann, 1990.
- [67] V. V. Vermehren and H. M. de Oliveira, “Close expressions for Meyer wavelet and scale function,” *An. XXXIII Simpósio Bras. Telecomunicações*, 2015, doi: 10.14209/SBRT.2015.2.
- [68] S. G. Mallat, *A wavelet tour of signal processing: the sparse way*, 3rd ed. Amsterdam ; Boston: Elsevier/Academic Press, 2009.
- [69] P. S. Addison, J. N. Watson, and T. Feng, “Low oscillation complex wavelets,” *J. Sound Vib.*, vol. 254, no. 4, pp. 733–762, Jul. 2002, doi: 10.1006/jsvi.2001.4119.
- [70] National Electrical Manufacturers Association., “NEMA standards publication NU 2–2007, performance measurements of positron emission tomographs.” Rosslyn, VA. 26-33., 2007.
- [71] S. Ziegler, B. W. Jakoby, H. Braun, D. H. Paulus, and H. H. Quick, “NEMA image quality phantom measurements and attenuation correction in integrated PET/MR hybrid imaging,” *EJNMMI Phys.*, vol. 2, no. 1, p. 18, Dec. 2015, doi: 10.1186/s40658-015-0122-3.
- [72] C. Catana *et al.*, “Simultaneous in vivo positron emission tomography and magnetic resonance imaging,” *Proc. Natl. Acad. Sci. U. S. A.*, vol. 105, no. 10, pp. 3705–3710, Mar. 2008, doi: 10.1073/pnas.0711622105.

- [73] D. Gabor, "Theory of Communication," *J. Inst. Electr. Eng.*, vol. Vol. 93, no. No. 3, pp. 429-457., 1946.
- [74] A. G. Ramakrishnan, S. Kumar Raja, and H. V. Raghu Ram, "Neural network-based segmentation of textures using Gabor features," in *Proceedings of the 12th IEEE Workshop on Neural Networks for Signal Processing*, Sep. 2002, pp. 365–374. doi: 10.1109/NNSP.2002.1030048.
- [75] R. Mehrotra, K. R. Namuduri, and N. Ranganathan, "Gabor filter-based edge detection," *Pattern Recognit.*, vol. 25, no. 12, pp. 1479–1494, Dec. 1992, doi: 10.1016/0031-3203(92)90121-X.
- [76] C. Cocosco, V. Kollokian, R. Kwan, and A. C. Evans, "BrainWeb: Online Interface to a 3D MRI Simulated Brain Database," *undefined*, 1997.
- [77] Z. Wang, A. C. Bovik, H. R. Sheikh, and E. P. Simoncelli, "Image quality assessment: From error visibility to structural similarity," *IEEE Trans. Image Process.*, vol. 13, no. 4, pp. 600–612, Apr. 2004, doi: 10.1109/TIP.2003.819861.
- [78] M. A. Kramer, "Nonlinear principal component analysis using auto associative neural networks," *AIChE J.*, vol. 37, no. 2, pp. 233–243, 1991, doi: 10.1002/aic.690370209.
- [79] H. C. Shyu and Y. S. Sun, "Underwater acoustic signal analysis by multiscaling and multitranslation wavelets," in *Wavelet Applications V*, Mar. 1998, vol. 3391, pp. 628–636. doi: 10.1117/12.304914.